VHF Magnetic and Electric Sensors for Partial Discharge Measurements in GIS

Mier Escurra, C.

DOI
10.4233/uuid:93980e67-9c6c-4ec5-8b4d-3b83412cf6fb

Publication date
2024

Document Version
Final published version

Citation (APA)
Mier Escurra, C. (2024). *VHF Magnetic and Electric Sensors for Partial Discharge Measurements in GIS*. [Dissertation (TU Delft), Delft University of Technology]. https://doi.org/10.4233/uuid:93980e67-9c6c-4ec5-8b4d-3b83412cf6fb

VHF Magnetic and Electric Sensors for Partial Discharge Measurements in GIS

Dissertation

for the purpose of obtaining the degree of doctor
at Delft University of Technology
by the authority of the Rector Magnificus, prof. dr. ir. T.H.J.J. van der Hagen,
chair of the Board for Doctorates
to be defended publicly on
Monday 08 July 2024 at 10:00 o'clock

By

Christian MIER ESCURRA

Master of Science in Electrical Engineering, Delft University of Technology, The Netherlands
Born in Aguascalientes, México

This dissertation has been approved by the promotors.

Composition of the doctoral committee:

Rector Magnificus,	Chairperson
Prof. ir. P.T.M. Vaessen	Delft University of Technology, promotor
Dr. A. Rodrigo Mor	TU Delft / Universitat Politècnica de València, Spain, promotor

Independent members:

Prof. Dr. R. Ross	Delft University of Technology
Prof. Dr. G. Robles Muñoz	Universidad Carlos III de Madrid, Spain
Prof. Dr. S. Tenbohlen	University of Stuttgart, Germany
Prof. Dr. R. Plath	Universität Berlin, Germany
Prof. Dr. M. Popov	Delft University of Technology, reserve member

This project 19ENG02 FutureEnergy has received funding from the EMPIR programme co-financed by the Participating States and from the European Union's Horizon 2020 research and innovation programme. Funder ID: 10.13039/100014132.
Project available at https://www.ptb.de/empir2020/futureenergy/home/

The love of family cannot be measured, but its existence is beyond doubt.

Table of Contents

Summary

The energy transition towards decarbonization and modernization of the electric network requires the development of new technologies. Offshore windfarms, essential to this transition, rely on Gas-Insulated Systems (GIS) due to their compactness and extended lifespan. Despite the reliability of GIS, the high maintenance costs and severe consequences of power outages leave no room for failure risks. The primary source of failures in GIS is attributed to defects in electric insulation, producing Partial Discharges (PDs) that serve as a tool for defect detection.

The current approach for standardized PD measurements proves impractical for implementation in GIS under operation. Consequently, unconventional methods have been employed with Ultra-High Frequency (UHF) sensors standing out. Despite the notable signal-to-noise ratio of the UHF system, it is still susceptible to interference and does not yield calibrated measurements suitable for comparison with other methods and for assessing insulation degradation. In response to these challenges, this study introduces a Very-High Frequency (VHF) system capable of providing calibrated and reliable measurements.

Very-High Frequency Sensors

The PD charge is the parameter used for PD instrument calibration, and it is impossible to estimate the charge in the UHF range. Therefore, this thesis delves into designing and characterising very-high frequency electric and magnetic sensors. The magnetic coupler is enhanced from a previous TU Delft design, improving its bandwidth and common-mode rejection. Furthermore, an electric sensor is also characterized in the VHF range and designed to interact with the magnetic sensor. The derivative response of these sensors enables PD charge estimation, which is crucial for sensor calibration. Mathematical models, validated through experimental setups, helped in the charge estimation accuracy and interference identification.

Electric and Magnetic Sensors Combination

PD pulse overlapping is one of the biggest challenges in GIS to estimate the charge accurately. Thus, building on the design and characterization of the electric and magnetic sensors, the thesis proposes their combination for overlapping elimination. This combination is achieved using two methods: adjusting their transfer functions (software method) and physically connecting them, similar to a directional coupler (hardware method). Results show that the sensors' combination distinguishes forward and backward components of PD propagation, improving charge estimation and waveshape reconstruction. Additionally, the software method allows the calculation of the PD power flow, aiding the defect localization.

A Calibration Process

Nowadays, there is no calibration process for unconventional PD measurements in online GIS. Hence, a calibration process for the VHF measuring system is shown in the thesis. This process is based on estimating the PD charge using the Voltage-Double-Integration (V2I) method, consisting of finding a scale constant by injecting low-frequency sinusoidal signals. The calibration's linearity, bandwidth and sensitivity were tested in three laboratories across Europe, giving estimation errors of below 30%, with the noise and the V2I approximation as the main uncertainties. The process demonstrates the potential for estimating PD charge in online GIS measurements, though with lower accuracy than the standard PD measurement (IEC 60270), suggesting room for improvement in the system uncertainty.

Interference Discrimination Method

Substations are subjected to multiple interferences that can be mistaken for PDs, making PD measurements unreliable. This work proposes an interference discrimination method by measuring the PD current and voltage and comparing their ratio with the GIS characteristic impedance. The method is based on the fact that signals propagating inside the coaxial GIS structure, such as PDs, have a similar magnitude between the measured electric and magnetic ratio and the GIS impedance, and any interference outside this propagation mode gives a different value. Under this hypothesis, four electric and magnetic ratio techniques were tested, identifying 98% of the PDs and 100% of the interferences. The application of this method is explored in a theoretical and a practical approach.

In conclusion, this thesis offers a novel approach to partial discharge measurements in online gas-insulated systems. Despite an uncertainty level above that indicated in the IEC60270 standard, this method stands as the only one providing a calibrated PD measuring system in online GIS, paving the way for a more reliable power system of the future.

Samenvatting

De energietransitie naar decarbonisatie en de modernisering van het elektriciteitsnet vereisen de ontwikkeling van nieuwe technologieën. Offshore windparken, essentieel voor de energietransitie, gebruiken Gas-Geïsoleerde Systemen (GIS) vanwege hun compactheid en verlengde levensduur. Ondanks de betrouwbaarheid van GIS laten de hoge onderhoudskosten en ernstige gevolgen van stroomstoringen geen ruimte voor risico op falen. De belangrijkste oorzaak van storingen in GIS wordt toegeschreven aan defecten in de elektrische isolatie. Deze produceren gedeeltelijke ontladingen (PD's) die kunnen dienen als een hulpmiddel voor de detectie van defecten.

De huidige aanpak voor gestandaardiseerde PD-metingen blijkt onpraktisch voor implementatie in GIS tijdens bedrijf. Daarom worden er onconventionele methoden onderzocht, waarbij Ultra-Hoge Frequentie (UHF) sensoren opvallen. Ondanks de lage signaal-ruisverhouding van een UHF-systeem is het gevoelig voor interferentie en levert het geen gekalibreerde metingen op die geschikt zijn voor vergelijking met andere methoden of voor het beoordelen van isolatiedegradatie. Als alternatief introduceert deze studie een Very-High Frequency (VHF) systeem dat gekalibreerde en betrouwbare metingen kan leveren.

Sensoren met Zeer Hoge Frequentie

De PD-lading is de parameter die wordt gebruikt voor de kalibratie van PD-instrumenten. Het is onmogelijk om de lading in te schatten in het UHF-bereik. Daarom gaat dit proefschrift in op het ontwerpen en karakteriseren van VHF elektrische en magnetische sensoren. De magnetische koppeling is verbeterd ten opzichte van een eerder ontwerp van de TU Delft. Daardoor zijn de bandbreedte en de common-mode-rejectie toegenomen. Bovendien wordt er ook een elektrische sensor gekarakteriseerd in het VHF-bereik. Deze is ontworpen om te interageren met de magnetische sensor. De afgeleide respons van deze sensoren maakt een inschatting van de PD-lading mogelijk, wat cruciaal is voor sensor kalibratie. Wiskundige modellen, gevalideerd door experimentele opstellingen, hebben geholpen bij de nauwkeurigheid van de ladingsschatting en de identificatie van de interferentie.

Combinatie van Elektrische en Magnetische Sensoren

De overlap van de PD-pulsen is een van de grootste uitdagingen in GIS om de lading nauwkeurig te kunnen schatten. Daarom, voortbouwend op het ontwerp en de karakterisering van de elektrische en magnetische sensoren, stelt dit proefschrift hun combinatie voor om overlapping te elimineren. Deze combinatie wordt bereikt met behulp van twee methoden: aanpassen van overdrachtsfuncties (softwaremethode) en een fysieke verbinding, vergelijkbaar met een richtingskoppelaar (hardwaremethode). De resultaten tonen aan dat de combinatie van

de sensoren de voorwaartse en achterwaartse componenten van de PD-propagatie onderscheidt, waardoor de ladingsschatting en golfvormreconstructie verbeteren. Bovendien maakt de softwaremethode de berekening van de PD-vermogensstroom mogelijk, wat bijdraagt aan de defectlokalisatie.

Een Kalibratieproces

Op dit moment is er geen kalibratieproces voor onconventionele PD-metingen in een online GIS. Daarom wordt in dit proefschrift een kalibratieproces voor het VHF-meetsysteem gepresenteerd. Dit proces is gebaseerd op het schatten van de PD-lading met behulp van de Voltage-Double-Integration (V2I) methode, bestaande uit het vinden van een schaalconstante door injectie van laagfrequente sinusvormige signalen. De lineariteit, bandbreedte en gevoeligheid van de kalibratie zijn getest in drie verschillende laboratoria in Europa met inschattingsfouten van minder dan 30% waarbij ruis en de V2I-benadering de belangrijkste onzekerheden zijn. Het proces toont het potentieel voor het inschatten van PD-ladingen in online GIS-metingen. de nauwkeurigheid is echter lager dan de standaard voor PD-metingen (IEC 60270), wat wijst op ruimte voor verbetering in de systeemonzekerheid.

Interferentie Discriminatiemethode

Onderstations worden blootgesteld aan verschillende interferenties die verward kunnen worden met PD's, waardoor PD-metingen onbetrouwbaar worden. Dit proefschrift stelt een interferentie discriminatiemethode voor door de PD-stroom en -spanning te meten en hun verhouding te vergelijken met de karakteristieke impedantie van de GIS. De methode is gebaseerd op het feit dat signalen die zich voortplanten binnen een coaxiale GIS-structuur, zoals PD's, een vergelijkbare grootte hebben tussen de gemeten elektrische en magnetische verhouding en de GIS-impedantie en dat elke interferentie buiten deze voortplantingsmodus een andere waarde geeft. Onder deze hypothese zijn vier technieken voor elektrische en magnetische verhouding getest, waarbij 98% van de PD's en 100% van de interferenties werden geïdentificeerd. De toepassing van deze methode is onderzocht met een theoretische en praktische benadering.

Concluderend biedt dit proefschrift een nieuwe benadering voor gedeeltelijke ontladingsmetingen in online gas-geïsoleerde systemen. Ondanks een onzekerheidsniveau dat boven die in de IEC60270 standaard ligt, is deze methode de enige die een gekalibreerd PD-meetsysteem biedt in een online GIS en maakt zo de weg vrij voor een betrouwbaarder energie-systeem van de toekomst.

List of Tables and Figures

List of Tables

List of Figures

Acronyms

AC	Alternating Current
BSL	Balanced Shielded Loop
BW	Bandwidth
Ca	Cavity discharge
CB	Carbon Black and epoxy resin mixture
CMC	Common-mode current
Co	Corona
DC	Direct Current
DGISC	Directional Gas-Insulated System Coupler
EM	Electromagnetic
EMF	Electro-Motive Force
FE	Floating Electrode
FEM	Finite Element Method
FFT	Fast Fourier Transform
FP	Fast Pulse
HV	High Voltage
JP	Jumping Particle
LCOE	Laboratorio Central Oficial de Electrotecnia
LPF	Low-Pass Filter
LV	Low Voltage
NPR	RMS-Noise-to-signal-Peak Ratio
SF_6	Sulphur Hexafluoride
TE	Transverse Electric
TEM	Transverse Electromagnetic
TF	Transfer Function
TL	Transmission Line
TM	Transverse Magnetic
TRF	Transformation Filter
TUDelft	Delft University of Technology
UBSL	Unbalanced Shielded Loop
V2I	Voltage double Integration
VNA	Vector Network Analyzer

1

"Persistence is the measurement of your belief in yourself".

- Brian Tracy

1. Introduction

Imagine driving on a desolate highway when suddenly, a sensor alerts you of an oil problem in the motor. Faced with this situation, you have two choices: you can either continue to the nearest mechanic, risking further damage to the car, or you can turn off the motor and wait for a tow truck, incurring financial and time losses. The optimal decision becomes clearer with more information about the failure. For instance, a detailed analysis of the oil amount and composition could provide valuable insights into the underlying problem. In this analogy, the car symbolises the gas-insulated system, the motor represents the electric insulation, the oil problem corresponds to partial discharge, and the oil measurement mirrors the proposed measuring system in this thesis.

1.1. Background

Electric substations serve as pivotal nodes in the electricity grid, facilitating energy transmission, distribution, voltage level adjustments, and system protection. The most prevalent type are Air-Insulated Substations (AIS), utilising surrounding air as the electric insulation medium due to its ubiquitous presence and cost-effectiveness. However, atmospheric pressure air is a relatively weak insulation medium. Additionally, AIS are exposed to environmental elements such as snow, rain, dust, wind, lightning, and wildlife.

For certain scenarios, encapsulating and filling the substation with controlled gas at a specified pressure becomes more advantageous. These enclosed substations, known as Gas-Insulated Systems (GIS), include gas-insulated substations, switchgears and lines. Over recent years, the popularity of GIS has grown, driven by advantages including

reduced physical space, improved reliability, and longer lifespan. These attributes make GIS attractive for specific contexts like densely urbanised areas, regions with harsh weather conditions, and offshore wind farms (Figure 1.1). As a result, the GIS market is forecasted to experience a 5.8% increase from 2023 to 2028, reaching a total value of 31.6 billion USD [1].

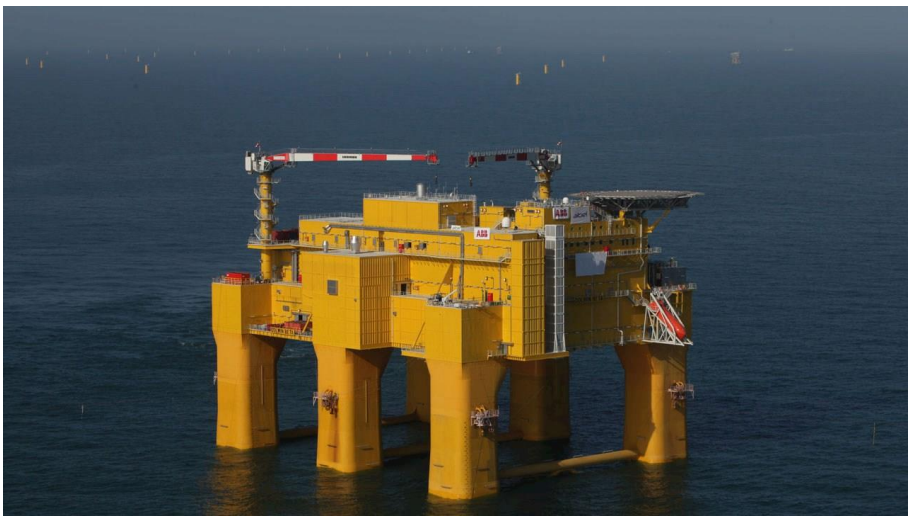

Figure 1.1 Offshore platform with GIS in the North Sea. Picture taken from [2].

The GIS high installation and maintenance cost and pivotal role in the power system demands a zero-margin approach to failures. Despite GIS demonstrate high reliability, they remain susceptible to insulation failures [3] and [4]. Maintenance for offshore substations is notably expensive compared to land-based counterparts, making it imperative to conduct interventions only when absolutely necessary. One strategy to prevent premature failures involves undertaking factory acceptance tests and site acceptance tests as part of the protocols outlined in the standard IEC 62271 [5]. A mandatory component of this standard is the measurement of Partial Discharges (PDs), conforming to the guidelines in IEC 60270 [6]. PD measurement serves not only as a requirement for routine and commissioning tests but also as a powerful tool for monitoring and diagnosing electric insulation [7] and [8].

IEC 60270 provides the standardised method for measuring partial discharges and calibrating PD measuring systems. The apparent charge magnitude, measured in pC, is the reference parameter for calibrated measurements. This charge value offers insights into the severity of insulation degradation, validates proper installation, and standardises readings across diverse sensors [9]. However, implementing IEC 60270 in online GIS proves impractical due to coupled interferences and restricted access to live conductors.

Recent trends in asset maintenance have shifted from time-based towards condition-based maintenance, necessitating diagnostic monitoring methods for online and onsite substations [10]. Recognising this shift, IEC 62478 [11] and CIGRE [12] recommend unconventional partial discharge measurement methods for GIS, including

acoustic techniques and Ultrahigh-Frequency (UHF) and Very-High Frequency (VHF) electromagnetic methods. The acoustic method detects the mechanical vibration of the energy released when the partial discharge occurs, making it impossible to extract electric parameters such as the charge. Another disadvantage is the interaction with environmental interference, driving the use of electric methods.

The UHF method employs electric antennas to measure the UHF (300 MHz – 3 GHz) electromagnetic fields produced by partial discharges. Although proven effective, this method sacrifices PD waveshape and charge information due to its frequency operation, which offers high noise rejection, [13] and [14]. While efforts have been made to verify the sensitivity of this method [15], a standardised calibration procedure is yet to be approved, and according to [11] and [12], this issue persists even at very-high frequency. However, [9] indicates that unconventional detectors, dealing with conducted signals within a specific frequency range, can be calibrated, providing charge magnitudes.

Very-high-frequency sensors operate below the UHF range (30 MHz – 300 MHz), capturing electromagnetic transients through inductive and capacitive sensors. The High-Frequency Current Transformer (HFCT) serves as a common VHF sensor for online PD measurements, [16] and [17], offering a high Signal-to-Noise Ratio (SNR) and practical installation in most cases. However, in GIS, the absence of a discontinuity in the enclosure where PD current is forced to flow, hinders the installation of HFCTs. A novel approach proposed in [18] involves coupling the HFCT in the bolts of GIS spacers. While effective for low-interference environments, this attempt is designed for older GIS installations where spacers are externally bolted to the flange. As a result, [19] proposed a novel VHF magnetic sensor installed in the GIS mounting holes, where presently UHF sensors are placed.

The magnetic sensor in [19] comprises a shielded magnetic loop measuring the magnetic field produced by PD current propagating in the GIS enclosure. The authors demonstrated in [20] that the sensor's measurement is proportional to the PD charge. Moreover, in [21], the authors presented a method to discriminate interference by comparing the sensor's mirrored lobes. While this research opens the possibility of calibrated measurements in GIS, several areas require improvement: the sensor's thin wire design makes it unsuitable for High Voltage (HV) applications, the unbalanced loop induces Common-Mode Currents (CMC) that affect the discrimination method, the accuracy of charge estimation and model characterisation at higher frequencies. Additionally, the presented measuring system lacks a calibration procedure. Therefore, this thesis attempts to provide the basis for a calibrated unconventional VHF PD measuring system.

This research is part of the EMPIR FutureEnergy European project, which focuses on developing metrology solutions for testing electric power components and monitoring

their condition. These solutions are required for the successful implementation of future electrification [22].

1.2. Objective and Research Questions

The goal of this thesis is to develop a very-high frequency PD measuring system for GIS that provides calibrated and reliable measurements.

The objective entails designing a measuring method for partial discharge integrated with a sensor exhibiting the necessary sensitivity, resolution and accuracy for PD charge estimation with a minimum value of 5 pC (Q1). The sensors must also be adapted to high-voltage applications (Q2) and reduce the uncertainty originated from overlapped pulses (Q3). A calibration process based on the PD charge should be provided for the proposed sensors (Q4). And finally, the measuring system should be reliable by effectively distinguishing between partial discharges and interferences (Q5). To address the objective, the following research questions are formulated:

Q1. How to model the electric and magnetic sensors, and how to improve their sensitivity, resolution, and accuracy?

The unbalanced magnetic sensor proposed in [23] successfully measured partial discharge and established a relation with the PD charge. However, this sensor was affected by common-mode currents, distorting the accuracy of the sensor. Additionally, its lumped element model constrained the sensor's characterization to lower frequencies.

Q2. How can the proposed magnetic sensor be adapted for HV GIS applications?

The magnetic sensors in [23] and the proposed one in Chapter 3 consist of a conductive wire inside the GIS enclosure, enhancing the power-frequency electric field. Shielding these sensors is crucial for their application in HV GIS.

Q3. How can the charge estimation uncertainty be reduced?

One of the main uncertainty sources in PD measurements in GIS is the pulse reflections [9], overlapping with the incident pulse and distorting the estimated charge and the PD pulse waveshape.

Q4. How can the proposed measuring system be calibrated?

The purpose of calibration is to compare the same quantity with another one, which is homogeneous with the measured one and is considered the measurement unit [24]. So far, there is no calibrated PD measurement for online GIS.

Q5. How can partial discharges be distinguished from interferences?

Onsite substations are susceptible to multiple interferences, leading to false identification of partial discharges [25]. Therefore, discrimination of interference in online PD measurements is of interest and is critical for maintenance programs in remote places, such as offshore GIS.

1.3. Contributions

The main contribution of this thesis to the field of partial discharge measurements in gas-insulated systems is summarised as follows:

- A mathematical model in the very-high frequency range for magnetic loop sensors and capacitive couplers (Chapter 3).
- A signal processing method for forward and backward components segregation and power flow propagation computation (Chapter 4).
- A high-voltage directional coupler for gas-insulated systems (Chapter 4).
- A calibration process for very-high frequency sensors in GIS (Chapter 5).
- An interference discrimination method based on the characteristic impedance of the GIS (Chapter 6).

These contributions forge the path to a more reliable PD monitoring system for HVDC/AC GIS, allowing better maintenance planning and reducing unnecessary costs, especially for offshore substations.

1.4. Thesis Layout

The thesis adopts a systematic approach by structuring the proposed measuring system in a linear progression. The sequence of chapters unfolds as follows: The initial chapter delves into comprehending the intricacies of partial discharge phenomena, laying the groundwork for subsequent research and development and then explaining the gas-insulated system as a propagation medium. Once the physical phenomena and its propagation media are understood, suitable magnetic and electric sensors are designed and characterised in Chapter 3. Chapter 4 integrates magnetic and electric sensors to create a method that enhances the measured signal, contributing to the core functionality of the measuring system. With the sensors' final design in place, Chapter 5 introduces a calibration process to ensure accurate and reliable measurements. This step is crucial to validate the measuring system's performance. Furthermore, Chapter 6 extends the applicability of the measuring system to onsite substations by proposing an interference discrimination method. The last chapter concludes the thesis by answering the research question and providing recommendations for future work.

Figure 1.2 provides a schematic representation of the thesis structure, visually capturing the logical flow of the presented chapters. Detailed descriptions of each chapter's focus are provided in the subsequent paragraphs.

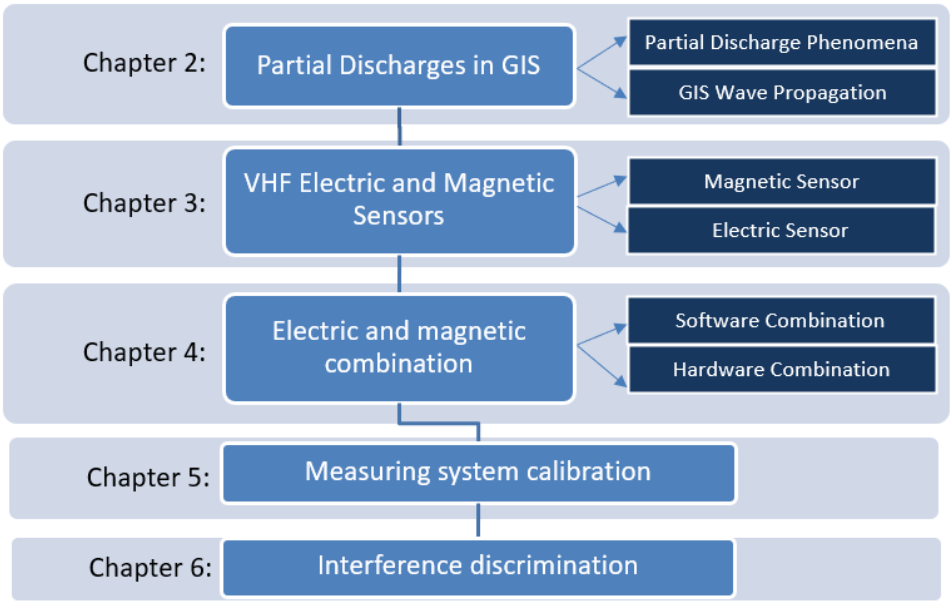

Figure 1.2 Schematic of thesis structure.

Chapter 2 is subdivided into two sections, providing an overview of partial discharges and their propagation within a GIS. The initial part explores GIS defects, the PDs waveshape in various gases and different charge estimation methodologies. The subsequent section shifts the focus to the propagation of very-fast transients within the GIS structure and the unconventional methods used for this type of substation.

Chapter 3 focuses on the design and modelling of very-high frequency sensors. Different versions of the magnetic sensor are designed, encompassing the unshielded loops, shielded loops, and balanced shielded loops. The second part introduces the electric coupler, using a commercial design but accompanied by its mathematical model tailored for the very-high frequency range. This chapter is based on the published articles [26]–[29].

Chapter 4 builds upon the outcomes of Chapter 3 by combining electric and magnetic sensors. The initial segment describes the software-based combination of sensors, facilitating the separation of forward and backward propagation components and the delineation of power flow. The subsequent portion describes the physical combination of sensors, resembling a directional coupler but customised for high-voltage applications. This chapter is based on the published articles [29] and [30].

Chapter 5 proceeds with the calibration methodology for the sensors introduced in preceding chapters. The calibration process is scrutinised through testing on a Low Voltage (LV) testbench and a full-scale GIS. Furthermore, the calibration method

undergoes evaluation in three laboratories equipped with distinct GIS setups. This chapter is based on the published articles [28] and [31].

Chapter 6 introduces a methodology for discriminating interferences in partial discharge measurements. The approach distinguishes partial discharges from interferences based on the GIS characteristic impedance. The characteristic impedance is calculated using the very-high-frequency electric and magnetic sensors presented in earlier chapters and through the calibration process outlined in Chapter 5 and other approaches. This chapter is based on the published articles [33] and [34].

2

"If you can not measure it, you can not improve it."

- Lord Kelvin

2. Partial Discharges in GIS

Before developing a measuring system, it is essential to understand the physical phenomena to be measured and the environment in which the sensor operates. Therefore, this chapter provides an overview of partial discharge mechanisms, covering the types of defects that give rise to partial discharges and the electrical waveform of PDs that the sensor captures. Subsequently, the methods for estimating PD charge are examined, constituting the calibration process's cornerstone. Once the nature of PD is described, its propagation in the gas-insulated system is explained. Finally, conventional and unconventional methods for PD measurements are presented.

2.1. Partial Discharge Phenomena

A partial discharge is a breakdown that partially bridges the insulation. In the presence of a defect within the insulation, when the local electric field exceeds the insulation strength and a starting electron appears, ionization occurs, creating an electronic avalanche, the partial discharge. Over time, the repetitive occurrence of partial discharges degrades the material, causing erosion and eventually leading to a full/complete breakdown of the insulation. Partial discharges are a primary cause of failures in HV equipment [35] and serve as valuable indicators for detecting premature insulation failures. Hence, timely detection of partial discharges is of utmost importance.

Two mechanisms explain the gas breakdown: the Townsend mechanism and the Streamer mechanism [36].

- Townsend mechanism: Gaseous dielectrics always contain free electrons induced by photons, radioactive radiation, and sometimes cosmic radiation. In the presence of an

electric field, electrons accelerate and gain kinetic energy, potentially colliding with gas molecules and ionising them. This process repeats, leading to the multiplication of free electrons, resulting in an avalanche. Positive ions in the avalanche accelerate towards the cathode, emitting new electrons. A feedback process begins if the avalanche produces enough new electrons, ultimately causing a breakdown. This mechanism's speed is influenced by the time required for avalanches and the feedback process to form.

- Streamer mechanism: Some discharges occur too rapidly to be caused by the Townsend mechanism, as there isn't enough time for feedback. The streamer mechanism occurs at a higher pressure and is explained differently. When an avalanche is formed, the space charge enhances the local electric field. With this higher electric field and a higher probability of photons hitting the dense gas, new ionisation occurs, forming a new avalanche that merges with the previous one, resulting in discharges.

The inception voltage for these discharge mechanisms is increased in electronegative gases, making them the most suitable for HV applications. In these gases, electrons attach to gas molecules rather than collide, and the formed heavy negative ions are too slow to initiate an avalanche. Hence, the field strength required to activate electrons and form avalanches must be considerably increased, resulting in very fast discharges. The most used electronegative gas is Sulphur Hexafluoride (SF_6) due to its excellent insulation properties.

The PD mechanism depends on the type of gas, gas pressure, and electrods distance.

2.1.1. Type of Defects

Partial discharges are categorised based on the underlying defect within the GIS, as detailed in [3] and [37].

Cavity Discharges occur within a gas-filled cavity embedded in a solid dielectric. The dissimilarity in permittivity between the solid and gas dielectrics results in a field enhancement in the gas. As the electric field surpasses a critical threshold, accumulated electrons in the cavity are emitted, causing a breakdown. In the initial stage within a virgin cavity, a Streamer occurs without a cathode for a feedback process. Over time, the PDs generate byproducts acting as electrodes, facilitating the Townsend mechanism. Under Alternating Current (AC) conditions, a third stage, known as pitting, emerges, forming crystals inside the cavity, leading to field concentration and streamer discharges, termed "pulseless discharge." This defect originates during the manufacturing process with atmospheric air trapped in the cavity.

Surface Discharge is another category of PD that occurs along dielectric interfaces within GIS. This typically occurs where a significant tangential field strength is present. In GIS, these interfaces are situated between the electrode, spacer, and gas. Particles on the spacer's

surface enhance the field in the interface, resulting in a streamer-type discharge, characterised by a sharp rising time and a slow falling time due to the long gap.

Corona Discharge involves the accumulation of charges at sharp points on the high voltage or ground electrode. Under both AC and Direct Current (DC) conditions, negative corona initiates at a similar voltage level, originating the starting electron through field emission from the cathode. In the case of SF_6, positive corona behaves differently, with the starting electron generally originating away from the sharp point due to the photo-ionisation mechanism. The Townsend mechanism governs the negative corona, while the positive corona follows the Streamer mechanism. Corona discharges may occur if GIS conductors are not well-polished.

Floating Electrode is a floating conductor, possessing capacitance between the high-voltage and ground electrodes, acting as a voltage divider. A discharge occurs if the induced voltage in the floating electrode reaches the inception voltage. This discharge is associated with a GIS conductor that is not correctly connected.

Jumping particle involves a free-moving conductor that, in its resting position, is in contact with the grounded electrode. Upon the energisation of the GIS, this particle acquires charge, interacting with the external electric field. Subjected to Coulomb's force and gravity, the particle accelerates in the direction of the resultant force, ultimately discharging in the electrode and returning to the grounded electrode. Minuscule metallic particles may become trapped inside the GIS during manufacturing, onsite installation or maintenance.

Figure 2.1 shows a graphical representation of the typical defects in a GIS.

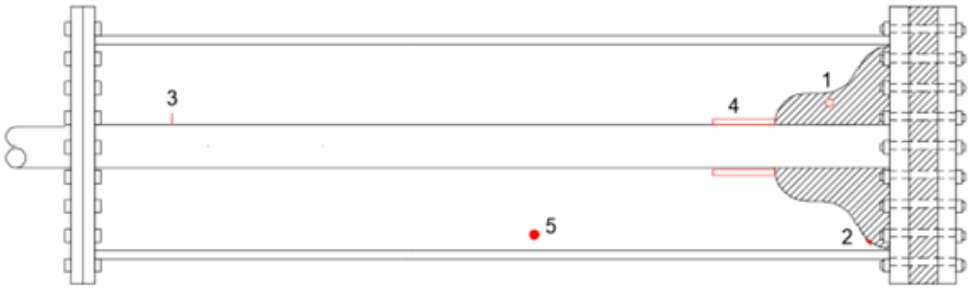

Figure 2.1. Defects in a GIS: 1) cavity, 2) surface particle, 3) protrusion in the HV electrode, 4) floating electrode, 5) jumping particle, [38].

2.1.2. PD Pulse Waveshape

A partial discharge is the movement of electrons in a short period, producing a current pulse. Parameters such as the pulse waveshape, PD repetition rate, PD pattern, and PD charge are valuable for identifying the type of defect and assessing the insulation degradation [16], [39]–[43].

The PD pattern proves to be a highly effective technique for discerning defect types and interference. In AC voltage, the PD pattern synchronises with the 50/60 Hz power voltage,

known as phase-resolved PD patterns. This method, well-established over the years [43], becomes impractical for DC systems lacking an AC-based signal, and discharges are less frequent, preventing pattern generation. Instead, pulse sequence analysis plots the discharge magnitude over time between successive discharges [44]. Machine learning techniques have recently been developed for partial discharge identification [40], [45] and [46].

The pulse waveshape not only provides insights into the physics of the discharge but also aids in deriving parameters for PD identification [40] and charge estimation. Moreover, the pulse rise and fall time determine the Bandwidth (BW) of the PD measuring system. Depending on the nature of the PD source, such as gas composition, gas pressure, and defect type, the pulse rise and fall time can vary from hundreds of picoseconds to tens of nanoseconds. The pulse frequency spectrum is crucial for determining the BW of the detection system. Reference [47] represents a PD as a Gaussian pulse, using equations (2.1) and (2.2) in the time and frequency domains, respectively. Here, I_0 denotes the pulse peak in Amperes and Amperes/seconds for the time and frequency domain, respectively; σ is related to the pulse width measured in seconds; t is time; and f is the frequency. Figure 2.2 a) and b) depict a Gaussian pulse's time and frequency domain representation with σ=30 ps, respectively.

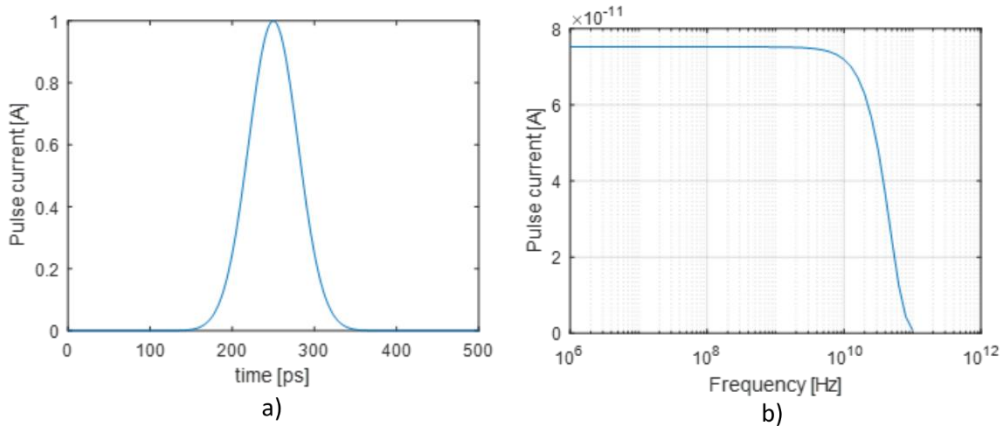

Figure 2.2. a) time domain and b) frequency domain of a Gaussian pulse with σ=30ps.

$$i(t) = I_0 e^{-t^2/2\sigma^2} \tag{2.1}$$

$$\boldsymbol{I}(\omega) = I_0 \sigma \sqrt{2\pi} e^{-1/2(2\pi f \sigma)^2} \tag{2.2}$$

The relationship between bandwidth and the pulse rise time, t_r, can be determined through (2.3) and (2.4). By definition, the rise time represents the duration for the pulse to transition from 10% to 90% of its peak value. Applying this definition to (2.1), along with the parameter σ, leads to equation (2.3). Subsequently, solving (2.2) with respect to the frequency and substituting σ with the derived expression from (2.3) yields the cut-off frequency (-3 dB = 0.7) as expressed in (2.4). It's essential to note that this represents a simplified calculation of the cut-off frequency; real partial discharges typically exhibit a slower fall time compared to the rise time.

$$\sigma = \frac{t_r}{\sqrt{-2ln(0.1)} - \sqrt{-2ln(0.9)}} = \frac{t_r}{1.7} \tag{2.3}$$

$$f_{3dB} = \frac{\sqrt{-2ln(.7)}}{2\pi t_r} * 1.7 = \frac{0.22}{t_r} \tag{2.4}$$

Table 2.1 presents the rise and fall times and frequencies for a corona discharge of SF_6 and alternative gases at 1 bar [48], with all pressures presented in this thesis being absolute. The data reveals that SF_6 exhibits faster characteristics than other gases, resulting in a higher bandwidth. As previously explained, this rapid behaviour in partial discharges is attributed to SF_6's electronegativity. Notably, the measured BW doesn't precisely correspond to the PD pulse, as the characteristics of the measuring system also influence it. Reference [47] demonstrates a test setup with sufficient resolution to measure 1 bar SF_6 pulses with a rise time of 64 ps (f_{3dB}=3.5 GHz).

Table 2.1. Waveshape parameters for different gases at 0.1MPa [48].

Gas	Rise time [ns]	Fall time [ns]	Cut-off frequency [MHz]
SF_6	0.8	2	279
N_2	8	100	28
CO_2	2	30	112
SF_6/ N_2 (1%/99%)	8	1	28
SF_6/ N_2 (60%/40%)	1	3	223

SF_6 has been used for more than 60 years thanks to its superior electric insulation and arc quenching [49]. However, due to SF_6's high global warming potential, its phase-out has been mandated in the coming years [50]. Synthetic air, composed of 80% nitrogen and 20% oxygen, emerges as a promising alternative to SF_6, offering advantages such as zero global warming potential, non-toxicity, and ease of handling but requiring a higher pressure to be comparable with SF_6. To assess the required PD measuring system for these alternative gases, the waveshape of clean air and other gases were measured using a test setup with a bandwidth above the VHF range.

To measure PD pulses in the UHF range, a test setup similar to the one used in [47] was constructed in the High-Voltage Lab at Delft University of Technology (TUDelft). SF_6, CO_2, C_4-FN/CO_2 (5%/95%), and clean air were analysed using the test setup depicted in Figure 2.3, showcasing a test cell designed for UHF measurements. Here, the needle is grounded through the 50 Ω coaxial connection, minimising parasitic elements that could reduce the bandwidth. An Oscilloscope Tektronix MSO58 with 2 GHz BW served as the acquisition unit, protected with a 1 dB-1 GHz attenuator and a 20 dB-1 GHz amplifier at the test cell's output. For personal protection, a 100 V-1 GHz surge arrester was connected to the oscilloscope input, as shown schematically in Figure 2.3 b).

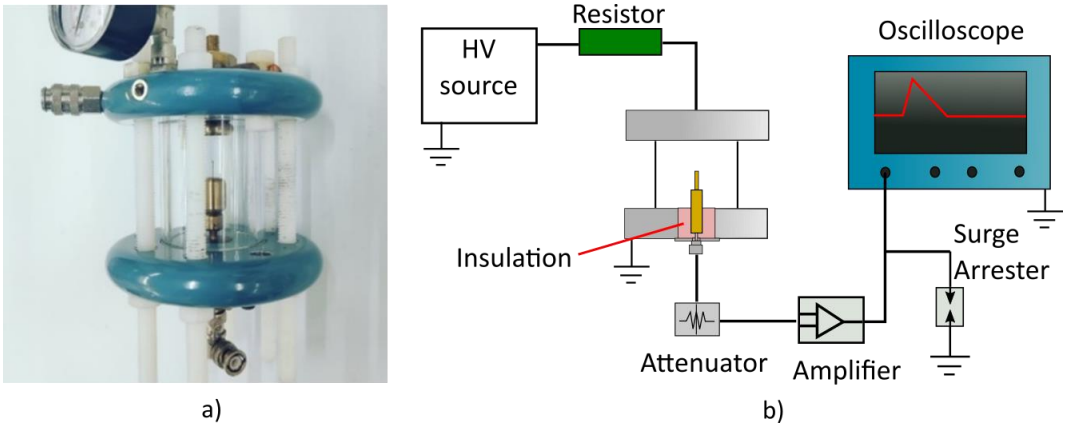

Figure 2.3. a) UHF Test cell, [51]. b) schematic of the test setup.

Table 2.2 summarises the mean values for 1000 samples per gas. Reference [47] demonstrated that SF_6-PD bandwidth can exceed 3 GHz, meaning that the BW in the test setup in Figure 2.3 is the one measured with the SF_6 gas, which is 655 MHz. In the case of the other gases, they exhibit lower BW even at high pressure. The BW in air discharges increases with pressure up to 4 bar, consistent with the findings in [52]. However, according to [52], a similar spectrum is achieved between SF_6 and air, conflicting with Table 2.2 and Figure 2.4, which compares an SF_6 pulse at 3 bar and an air one at 4 bar. Further research is necessary to clarify the differences between both experiments. Nevertheless, based on this table, VHF measuring systems are more suitable for SF_6-alternative gases. The impact of SF_6-alternative gases on PD waveforms is of great interest to electric power engineers, resulting in the new Cigre working group D1.78, [53].

Table 2.2. Waveshape parameters for different gases using a UHF test setup.

Gas	Rise time	Fall time	Cut-off frequency
SF_6 @3 bar	0.33 ns	0.37 ns	655 MHz
CO_2 @1 bar	2.4 ns	24 ns	103 MHz
C_4-FN/CO_2 @1 bar	1.3 ns	2.3 ns	183 MHz
Clean air @1 bar	14 ns	90 ns	19 MHz
Clean air @2 bar	3.2 ns	25 ns	128 MHz
Clean air @4 bar	1.3 ns	9.4 ns	192 MHz
Clean air @5 bar	1.7 ns	5.9 ns	155 MHz

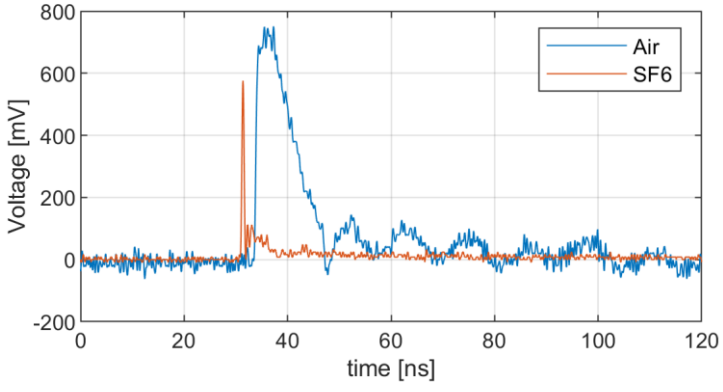

Figure 2.4. Air @4 bar and SF_6 @3 bar waveshape.

2.1.3. Charge Estimation Methods

The PD charge stands out as a parameter independent of the measured frequency, making it a universal metric for insulation diagnostics and the calibration of PD measuring systems. In contrast, other measured PD pulse parameters, such as peak value, rise time, and fall time, depend on the measuring system's bandwidth, rendering them inadequate as universal comparison parameters. Although the charge is used as a fundamental parameter of the PD, this is not the actual charge produced in the defect. What is measured is a portion of the charge, known as the apparent charge.

Figure 2.5 explains the definition of the apparent charge using the ABC model. When a PD occurs at the cavity with a capacitance C, the voltage collapses, and ΔV_c results in the PD charge $q_c=\Delta V_c C$. This charge is compensated by all the capacitance (A) in parallel with the defect and the capacitance of the measuring coupling capacitor (C_k). Therefore, the current used to measure the apparent charge is i_{Ck}, a fraction of the real PD current [54].

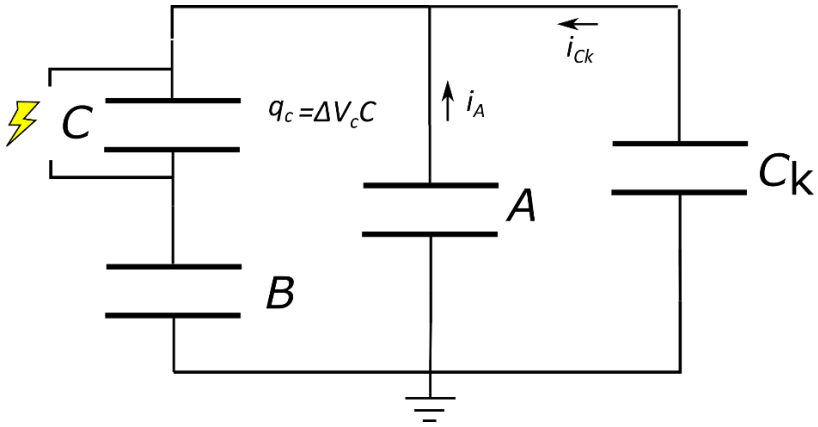

Figure 2.5 ABC circuit illustrating the origin of the apparent charge.

By definition, the charge is the integral of the current, as expressed in (2.5), where T denotes the integration time, equivalent to the measured window. Utilising the definition of the Fourier transform (2.6) and evaluating the current at zero frequency, then it results in (2.7). This equation is equivalent to (2.5), demonstrating that the charge corresponds to the DC component of the current. Equation (2.2) and Figure 2.2 b) illustrated that the frequency response of a pulse remains flat with the DC value in the low-frequency range. Two fundamental conclusions can be drawn from this analysis:

- The PD charge information is contained in the low-frequency range.
- The PD charge is not attenuated with the frequency.

$$\mathrm{q} = \int_0^T i(t)dt \tag{2.5}$$

$$F(\omega) = \int_{-\infty}^{\infty} f(t) e^{-j\omega t} dt \tag{2.6}$$

$$F(0) = \frac{1}{T} \int_{0}^{T} i(t) dt \tag{2.7}$$

From the previous analysis, the following charge estimation methods are extracted:

Time-domain charge estimation

This method employs (2.5) to estimate the charge, acknowledging that this equation represents the DC component, and thus, it cannot be measured with a derivative sensor (inductive or capacitive). However, [55] demonstrates that the charge can be approximated by integrating from the pulse starting time (t_0) to the first zero-crossing (t_1), giving a nonzero value for derivative sensors. This shorter integration time minimises white noise and offsets errors. To relate the sensor's output voltage $v_o(t)$ with the input PD current, the sensor's transfer impedance $\boldsymbol{G}(f)$ is used, resulting in the charge estimation in (2.8), where $\boldsymbol{G}(f)$ is the frequency-domain-flat-region gain.

$$\mathrm{q} \approx \frac{1}{\boldsymbol{G}(f)} \int_{t_0}^{t_1} v_o(t) dt \tag{2.8}$$

As demonstrated in [55], the accuracy of (2.8) depends on the BW of the measuring system. Figure 2.6 illustrates the output measurements for sensors with different BW, showcasing how accuracy decreases with decreasing BW. As the BW decreases, the pulses respond with an undershoot a), and the charge estimation accuracy decreases b). As the integration time increases, the charge estimation approaches zero; therefore, the charge is improved by integrating up to the first zero-crossings (vertical lines). Resistive sensors, such as oscilloscopes, have a Low-Pass Filter (LPF) response, so in principle, they can accurately measure the charge. This estimation method is used through this thesis for reference sensors composed of an HFCT and a directly connected oscilloscope.

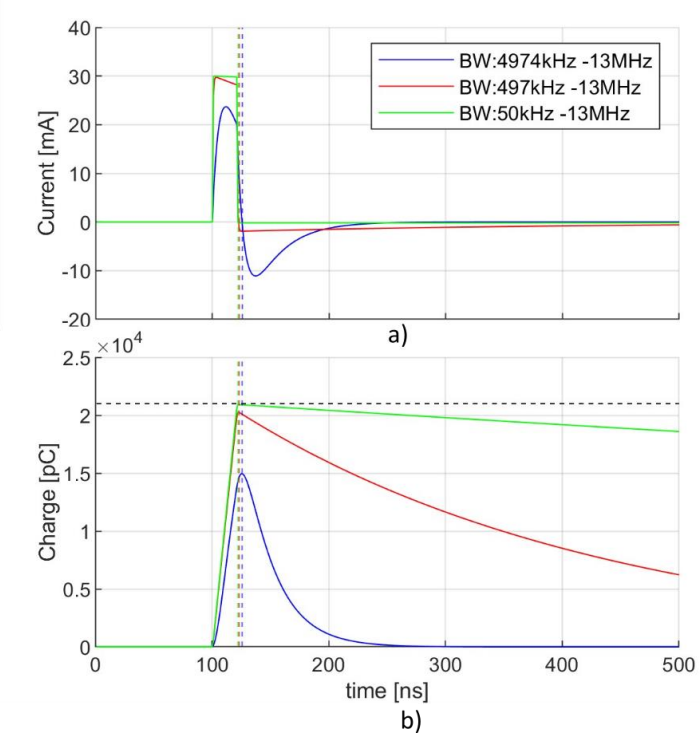

Figure 2.6. a) Output voltages for derivative sensors with different BW, and b) accumulated estimated charge. The horizontal line represents the real charge, and the vertical lines are the first zero-crossings for each waveshape.

Frequency-domain charge estimation

This method is based on the PD pulse and sensor frequency response. As demonstrated in section 2.1.2, the frequency response of a pulse resembles a low-pass filter. A sensor with a BW covering the pulse's flat region can estimate the charge using (2.9), where $\boldsymbol{V}_o$ is the sensor's measured output in the frequency domain, and f_0 is a frequency component approximating the DC one. This method was not employed in this thesis due to noise accumulation, but more information about it can be found in [55].

$$q \approx \frac{\boldsymbol{V}_o(f_0)}{\boldsymbol{G}(f_0)} \tag{2.9}$$

Voltage-Double-Integration method

Figure 2.6 illustrated that the time-domain charge integration method based on the current integration is inaccurate for narrow BW sensors. The Voltage-Double-Integration (V2I) method is another time-domain method effective for narrow-band sensors exhibiting prominent undershoot. The charge is estimated using (2.10), where k is the calibration constant [56].

$$q \approx \frac{1}{k}\int_0^t \int_0^t V_o(t)dtdt \tag{2.10}$$

Figure 2.7 compares the same waveshapes from Figure 2.6 and their charge estimation using the V2I method. In this case, a better estimation is obtained with the shorter BW, contrary to the first method. The signals are integrated up to the second zero-crossing to avoid

the double accumulation of white noise and offset. The waveshapes in Figure 2.7 are noiseless ideal signals, so the second zero-crossing is never reached; therefore, the voltage is integrated up to the time when the second zero-crossing approaches 1% of the peak value ($t=t_{2z}$). The sensors presented in this thesis are suitable for this method, so an extended explanation of the V2I process is given in Chapter 0 once the sensors are characterised in Chapters 0 and 0.

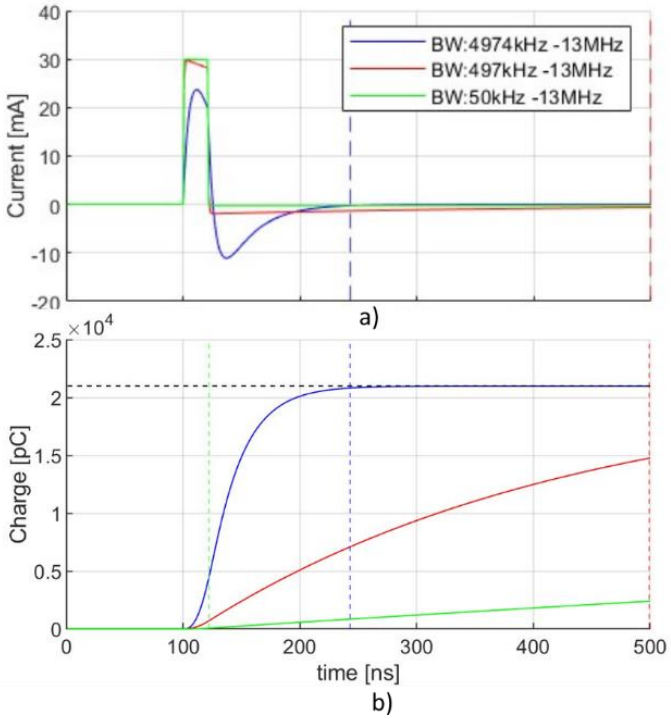

Figure 2.7. a) Output voltages for derivative sensors with different BW, and b) accumulated estimated charge. The horizontal line represents the real charge, and the vertical lines approximate the second zero-crossings (1% of the peak value).

Quasi-integration charge estimation

The IEC 60270 is the standard method for partial discharge measurements based on the quasi-integration method. This conventional method is illustrated in Figure 2.8, consisting of an HV source connected to a limiting impedance (Z), the device under test (DUT) and a coupling capacitor (C_k) in series with a coupling device (CD). The PD current flows through the coupling capacitor and device, which is the path with less impedance. The coupling device typically comprises a resistor and an inductor in parallel with a capacitor in series, ensuring that the measuring instrument (MI) detects only the high-frequency signal and not the power-frequency voltage, [6], [54] and [57]. Additionally, a step-up transformer is connected between the CD and MI to increase the SNR, [36].

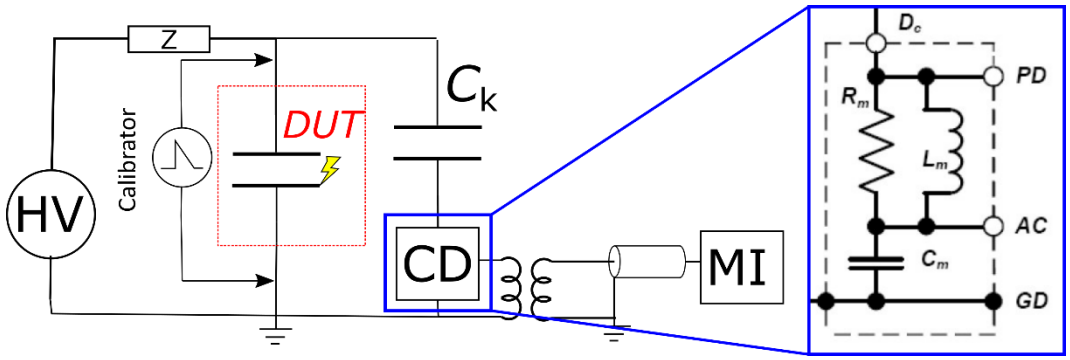

Figure 2.8. IEC 60270 measuring circuit with the elements of the coupling device, [58].

To calibrate the measuring system, a current pulse with a known charge is injected into the DUT, and the output peak signal is measured. Then, when a PD happens, the measured peak output is proportional to the calibrator's charge and peak voltage, according to (2.11). This proportionality holds when both the calibrator and the PD pulse have a flat frequency response at the BW of the measuring system. Figure 2.9 illustrates an example with the BW of the measuring system within and outside the flat part of a 251 nC calibrator and 125 nC PD. For the 50-200 kHz bandpass filter, the output peak voltages are proportional to the charges, contrary to the 0.5-2 MHz filter.

$$q_{PD} \approx \frac{q_{Cal}}{V_{peakCal}} V_{peakPD} \tag{2.11}$$

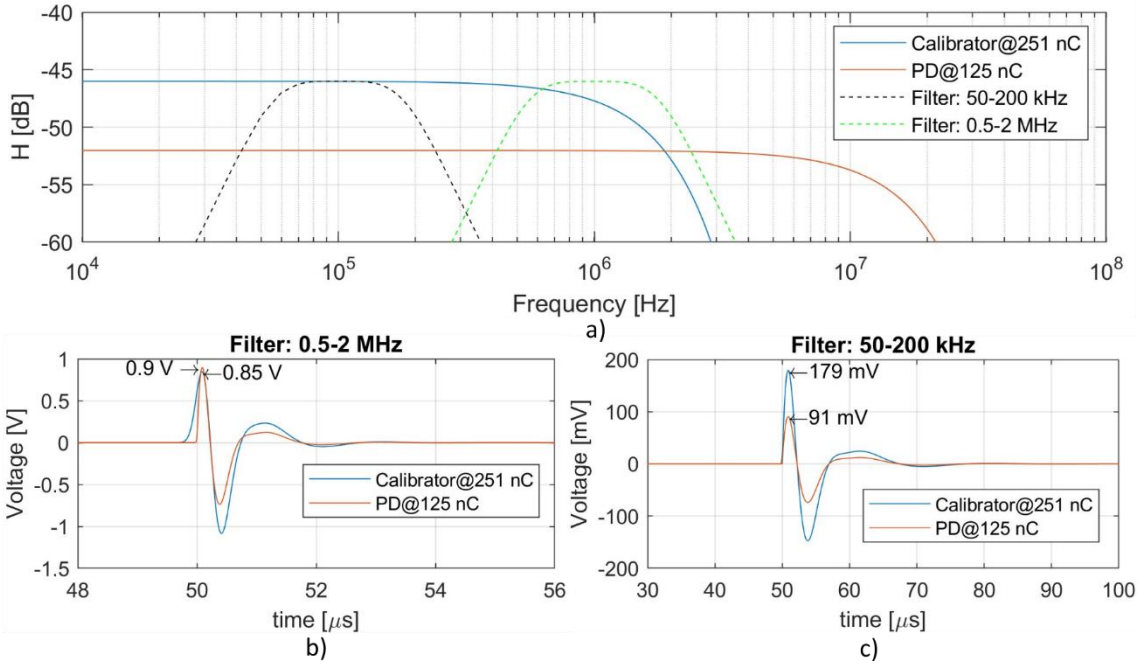

Figure 2.9. Quasi-integration method applied to two filters with different BW. a) Frequency response of the Calibrator, PD pulse and different filters. PD and calibrator time-domain measurements using a b) 0.5-2 MHz bandpass filter and a c) 50-200 kHz bandpass filter.

2.2. GIS Wave Propagation

A partial discharge is the rapid acceleration of electrons lasting less than a few nanoseconds, requiring its modelling as a propagation wave. Existing literature [59] suggests that lumped element models lose validity when the electric wavelength is less than ten times the physical length. This section initially reviews electromagnetic (EM) wave propagation in GIS as presented in [60]. Then, the consequences of the PD propagation to measurements are described.

2.2.1. Propagation Modes

The acceleration of charge induces electromagnetic waves according to Maxwell's curl equations:

$$\nabla \times \hat{E} = -j\omega\mu\hat{H} \tag{2.12}$$

$$\nabla \times \hat{H} = j\omega\mu\hat{E} \tag{2.13}$$

The solutions for Maxwell's equations in the propagation direction (z-direction) are classified based on whether one or both EM components are zero in the same direction:

- Transverse Electric and Magnetic (TEM): $E_z = H_z = 0$
- Transverse Electric (TE): $E_z = 0$ and $H_z \neq 0$
- Transverse Magnetic (TM): $H_z = 0$ and $E_z \neq 0$

Maxwell's equations have three orthogonal solutions: two curl-based solutions (TE and TM) and one gradient-based solution linked to the charges (TEM). When a PD occur, the GIS guides the energy as a coaxial waveguide where these three modes propagate.

Transverse electromagnetic mode

The TEM is a plane wave since there is no field in the direction of propagation. Equation (2.14) shows the Helmholtz equation in cylindrical coordinates, where γ is the propagation constant in a lossless medium equal to (2.15), and μ and ε are the permeability and permittivity of the medium, respectively. The electric and magnetic field solutions are given in (2.16) and (2.17), respectively, where η is the wave impedance, $E_\rho{}^+$ is the forward wave and $E_\rho{}^-$ is the backwards wave. If circuit parameters are used instead of wave parameters (voltage and current), the TEM mode can be modelled using Transmission Line (TL) theory. In a coaxial line, the characteristic impedance Z_{0TEM} and group velocity v_{gTEM} are given by (2.19) and (2.20), respectively, where b is the outer conductor diameter, a is the inner conductor diameter, and c is the speed of light in vacuum.

$$\frac{\partial^2 E_\rho(\omega,z)}{\partial z^2} - \gamma^2 E_\rho(\omega,z) = 0 \tag{2.14}$$

$$\gamma = j\omega\sqrt{\mu\varepsilon} \tag{2.15}$$

$$E_\rho(\omega,z) = E_\rho{}^+ e^{-\gamma z} + E_\rho{}^- e^{\gamma z} \tag{2.16}$$

$$H_\varphi(\omega,z) = \frac{E_\rho(\omega,z)}{\eta} \tag{2.17}$$

$$\eta = \sqrt{\mu/\varepsilon} \tag{2.18}$$

$$Z_{0TEM} = \frac{V}{I} = \frac{\eta}{2\pi} ln(b/a) \tag{2.19}$$

$$v_{gTEM} = \frac{c}{\sqrt{\varepsilon\mu}} \tag{2.20}$$

Transverse electric and magnetic modes

In the TE and TM modes, one of the fields has the same direction as the propagation. By solving Maxwell's equations under this condition, the propagation constant equals (2.21). If $k_c > \omega^2\mu\varepsilon$ in (2.21), the TE and TM modes can propagate. The TE (2.22) and TM (2.23) cut-off frequencies in a coaxial waveguide are taken from [61], where m and n are the integers that determine the mode of operation of the TE and TM modes, respectively. Unlike the TEM mode, the characteristic impedance of the TM and TE mode is frequency-dependent, as expressed in (2.24) and (2.25).

$$\gamma_{TE,TM} = \sqrt{k^2{}_c - \omega^2\mu\varepsilon} \tag{2.21}$$

$$f_{cTE} = \frac{c \cdot m}{\pi(a+b)} \tag{2.22}$$

$$f_{cTM} = \frac{c \cdot n}{2(b - a)} \tag{2.23}$$

$$Z_{0TE} = Z_{0TEM} \frac{1}{\sqrt{1 - {f_{cTE}}^2 / f^2}} \tag{2.24}$$

$$Z_{0TM} = Z_{0TEM} \sqrt{1 - {f_{cTE}}^2 / f^2} \tag{2.25}$$

The group and phase velocities are equal in the TEM mode, contrary to the TE and TM modes, where the group and phase velocities differ. The phase velocity is higher than the speed of light, but it is an apparent speed. The propagation of energy is dictated by the group velocity, which is lower than in the TEM mode and is defined in (2.26).

$$V_{gTE/TM} = V_{gTEM} \sqrt{1 - \left(f_{cTE/TM} / f\right)^2} \tag{2.26}$$

2.2.2. EM Propagation in GIS discontinuities

The TEM mode propagates in any frequency excluding DC; above the TE cut-off frequency, f_{cTE}, the TEM and TE modes can propagate, and beyond the TM cut-off frequency, f_{cTM}, any of the three modes can propagate. In this section, the frequency below the TE mode cut-off frequency ($f_c < f_{cTE}$) will be referred to as the EM wave exclusively in TEM mode. Reference [12] classifies non-conventional electric methods in UHF and HF/VHF ranges. The UHF range (0.3-3 GHz) is above f_c: capacitive coupling antennas are in this category, and the VHF range (30-300 MHz) is below f_c, where the magnetic sensor presented in [23] belongs. According to [12]–[14] and [55], it is impossible to estimate the PD charge with sensors having a BW exceeding the f_c; therefore, the magnetic sensor's frequency is expected to be used under f_c. Table 2.3 shows the cut of frequencies for the GIS installed in the TUDelft HV lab using (2.22) and (2.23). This GIS was used for the experiments in this thesis.

Table 2.3. Dimensions and cut-off frequencies for the GIS in TUDelft, where *a* and *b* are the inner and outer diameters.

Dimensions	TEM cut-off frequency	TE_{11} cut-off frequency	TM_{11} cut-off frequency
b=53 cm, a= 10 cm	0	284 MHz	698 MHz

Gas-insulated switchgears comprise several sections with different impacts on wave propagation: straight lines, spacers, change of diameter, L-sections, T-sections, disconnectors and bushings. The next sections present the propagation in each discontinuity.

Straight lines

Reference [62] mentions the attenuation in straight GIS sections for each mode: TEM: 2-3 dB/km, TE: 0-4 dB/km and TM: 3-10 dB/km. This attenuation might be considerable in gas-

insulated lines, but the dimensions are a few tens of meters for a gas-insulated substation. On the other hand, the relative position between the PD source and the sensor affects the TE and TM modes. Reference [14] demonstrated through finite difference-time domain simulation that the TE and TM propagation modes vary along the line. The results show that the sensor's and PD source's relative angular position attenuates the measurement, giving a maximum value at 0° and a minimum at 90°, [63]. Even when the sensor and the defect are aligned, the measurement is attenuated because each propagation mode is delayed by their speed difference (2.26).

Signals below the f_c propagate uniformly far from the source, but the current is not homogeneous near the source location. The current density depends on the diffusive fields and is calculated using (2.27) to (2.29), where $\hat{J}$ is the current density and σ is the electric conductivity of the conductor.

$$\nabla \times \hat{H} + \hat{J} = 0 \tag{2.27}$$

$$\nabla \times \hat{E} + \omega\mu\hat{H} = 0 \tag{2.28}$$

$$\hat{J} = \sigma\hat{E} \tag{2.29}$$

References [18] and [38] presented a PD measuring method in a GIS using HFCTs. Figure 2.10 a) depicts how the HFCT couples the PD current that flows through the GIS-flange bolts. Using this method, the distribution of the current near the PD source was measured by injecting a pulse in the GIS's inner conductor and to the top surface of the enclosure, as illustrated in Figure 2.10 b). Then, the current was measured using HFCTs installed in the top and bottom bolts of the spacers, as shown in Figure 2.11 a). The current distribution from one spacer to the next one was measured (Figure 2.11 b), limited by the distance between spacers (spacer1: 7 cm and spacer2: 226 cm from source).

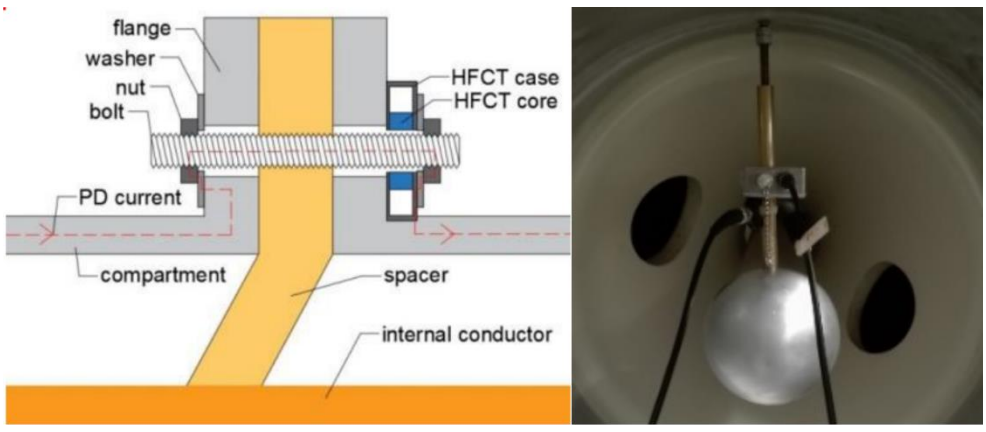

Figure 2.10. a) HFCT method for PD measurements in GIS [18]. b) Injection of a pulse to the top surface of the enclosure, [38].

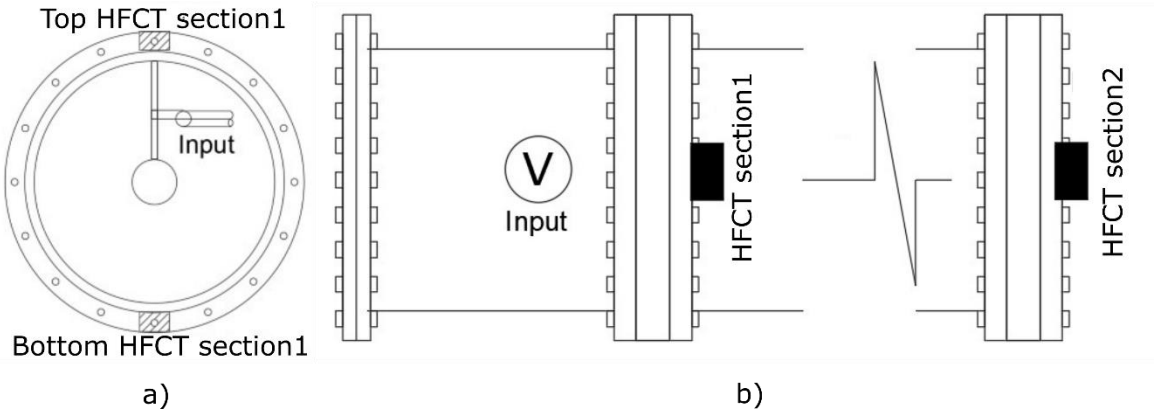

Figure 2.11. Test setup for measuring the current distribution near the PD. a) transversal view and b) top view

Table 2.4 shows the voltages ratios between the top and bottom HFCTs at different frequencies. At 226 cm, the current is already uniform, but at 7cm, the current is still dense at the top of the enclosure. The long-distance between spacers prevents the acknowledgement of the exact distance where the current is uniform in the transverse direction. Hence, a Finite Element Method (FEM) simulation was done.

Table 2.4. Current distribution results in the frequency and time domain for 7 cm and 226 cm distance.

	Bottom/Top current ratio	
Frequency and time domain	7 cm	226 cm
1 MHz	0.41	1.00
10 MHz	0.51	1.00
100 MHz	0.58	1.00
Voltage peak	0.42	1.00

Using TUDelft's GIS dimensions, the distance in which the current is uniform was estimated with FEM. A current source was connected from the inner conductor to the outer conductor. The ratio between the current at the top and bottom of the enclosure is compared and plotted for different distances from the source and enclosure sizes. Figure 2.12 shows the lateral view of the current distribution in the enclosure surface, where a maximum density flows at the top and a minimum at the bottom. The current density is already uniform at 50 cm from the source. Figure 2.13 illustrates the results from different enclosure radii, giving a uniform current for the three configurations at 50 cm: the lower the enclosure's radius, the faster the current is distributed. The difference between the simulation and the measurements at 7 cm is because, in the experimentation, all the current was forced to flow in the direction of the bolt axis, contrary to the simulation where the current had components in the three axes.

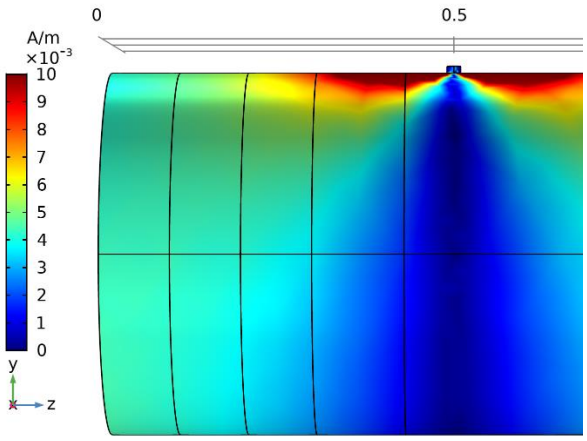

Figure 2.12. Lateral view of the current distribution in the GIS using an enclosure with a radius of 265 cm.

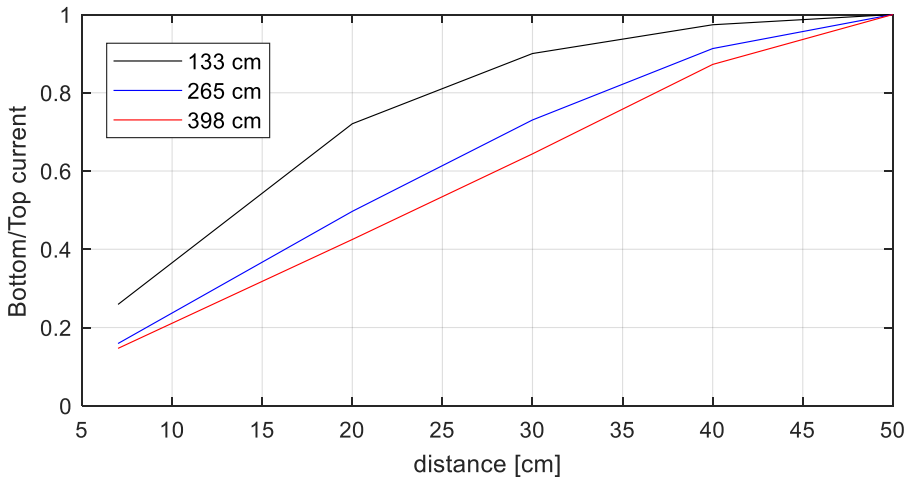

Figure 2.13. Bottom/Top current ratio at different distances from the source and for different enclosure radii.

Spacers

The spacers are a solid support to separate the inner conductor and the enclosure. Figure 2.14 illustrates the two types of spaces used in GIS: a) metal flange type and b) bush type. Using UHF sensors, [57] found that the signal attenuation through spacers is attributed to the group velocity split in different propagation modes. Additionally, the authors found higher attenuation in the bush-type spacers: the EM wave escapes from the GIS through the spacer.

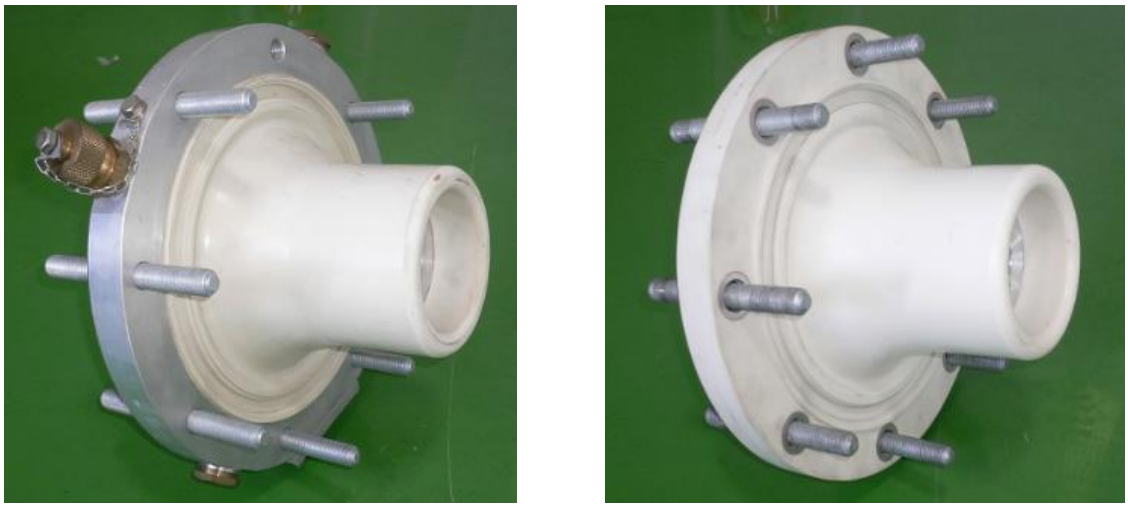

a) b)

Figure 2.14. Different types of spacers, a) metal flange type, b) bush type. Figures taken from [64].

Reference [65] found that the attenuation of the TEM mode in a spacer is due to the change of the characteristic impedance, reflecting the incident travelling wave. A spacer is a discontinuity in the transmission line, and the impedance difference between the discontinuity and the rest of the transmission line causes a reflection at the interface. Equations (2.30) and (2.31) show the reflection and transmission coefficient, respectively, from the GIS and the spacer interface (Figure 2.15), where the subindex identifies the transmission line after and before the interface.

$$\Gamma_{12} = \frac{Z_2 - Z_1}{Z_1 + Z_2} \tag{2.30}$$

$$T_{12} = 1 + \Gamma_{12} \tag{2.31}$$

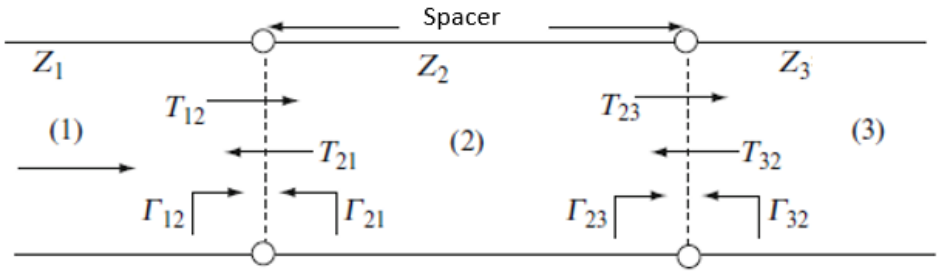

Figure 2.15. Transmission line representation of the GIS and spacer interface. Modified picture taken from [60].

Using the previous equations, the reflected and transmitted voltages are represented in (2.32) and (2.33), where $V_0{}^+$ is the incident wave. By repeating the process for each incident voltage wave at each interference, the voltage reflection diagram is assembled. The wave can be calculated for any position and time by knowing the propagation speed, as shown in Figure 2.16, after five iterations.

$$V_1{}^- = V_0{}^+ \Gamma_{12} \tag{2.32}$$

$$V_1{}^+ = V_0{}^+ T_{12} \tag{2.33}$$

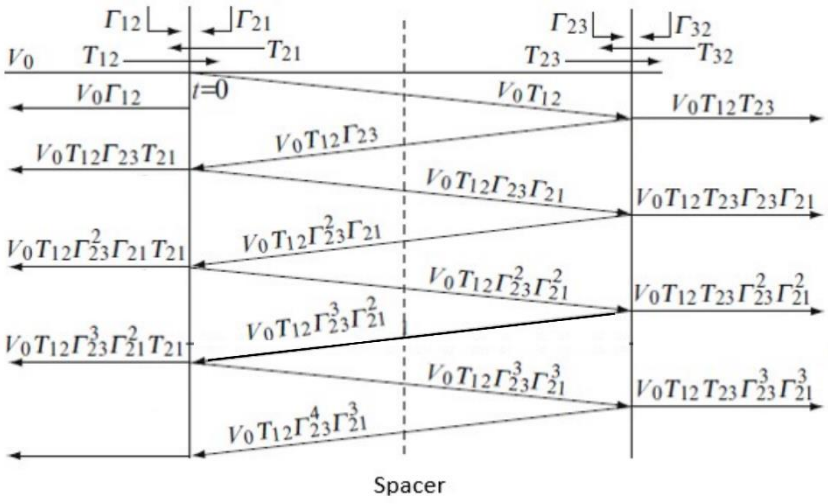

Figure 2.16. Voltage reflection diagram after five steps. Modified picture taken from [60].

If more spacers are considered, each transmitted wave resulting from the first spacer is taken as the incident wave for the next spacer and so on. The process becomes too elaborate for a GIS with many spacers, requiring transient analysis software. The attenuation in the TEM mode of a single spacer was calculated using Simulink, RF module. Making the same assumption as in [66], a disc geometry of the spacer with a relative permittivity of 5.3 (according to [62]) and a length of 30 cm was taken. Figure 2.17 a) shows the time domain and b) the frequency domain of the spacer-transmitted pulse. According to the results, the signal frequency above 100 MHz is attenuated by 3 dB.

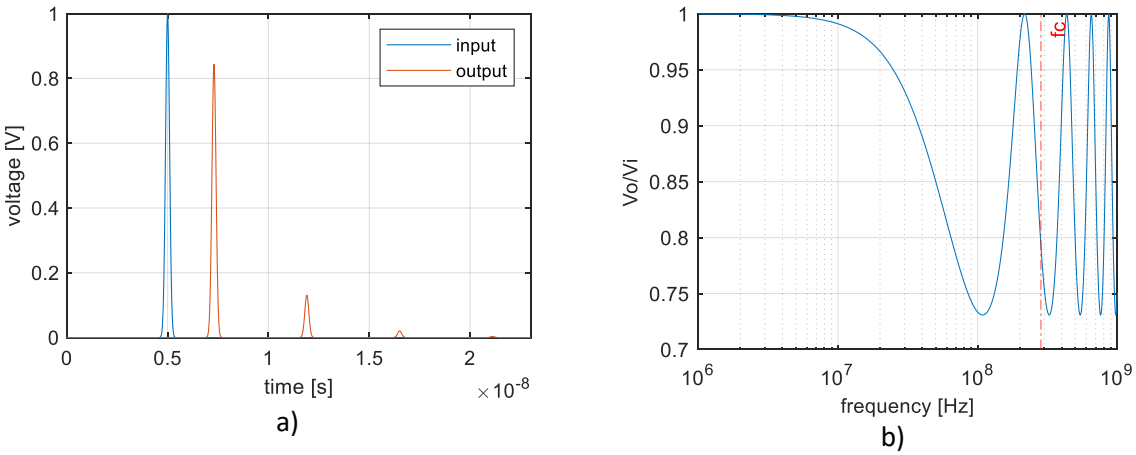

Figure 2.17. a) Incident and transmitted pulse in the time domain. b) S21 parameter after a spacer.

Change of GIS diameter

GIS commonly exhibit sections with different diameters, e.g., a circuit breaker or a disconnector. The characteristic impedance of the section is different depending on the geometry. For frequencies below f_c, the wave propagation is calculated similarly to the spacer. For example, the circuit breaker of the GIS installed at TUDelft has an enclosure diameter 1.7 times larger than the rest of the switchgear, assuming that the inner conductor diameter is maintained: the characteristic impedance results in 132 Ω, hence, 1.3 times larger than the

rest of the GIS. Although the difference in characteristic impedance is not as significant as with the spacer, the length of the section is affected in lower frequencies.

Using Simulink, RF module, the attenuation in the TEM mode was calculated, with a circuit breaker 1.8 m long. Figure 2.18 illustrates the simulated GIS section, where the "input" is the section before the circuit breaker, the "inbetween" section represents the measure in the middle of the discontinuity, and the "output" section is measured subsequently to the discontinuity. Figure 2.19 a) shows the incident and transmitted pulses. To better perceive the section's length effect, b) shows the calculation of the transmission coefficient for different electric length and wavelength ratios. In [67], the pulse inside the "inbetween" section was attenuated, differing from this simulation. However, the measurements in [67] were made with an electric coupler without considering that the gain of this sensor decreases with the relative distance between the GIS inner and outer conductors [66].

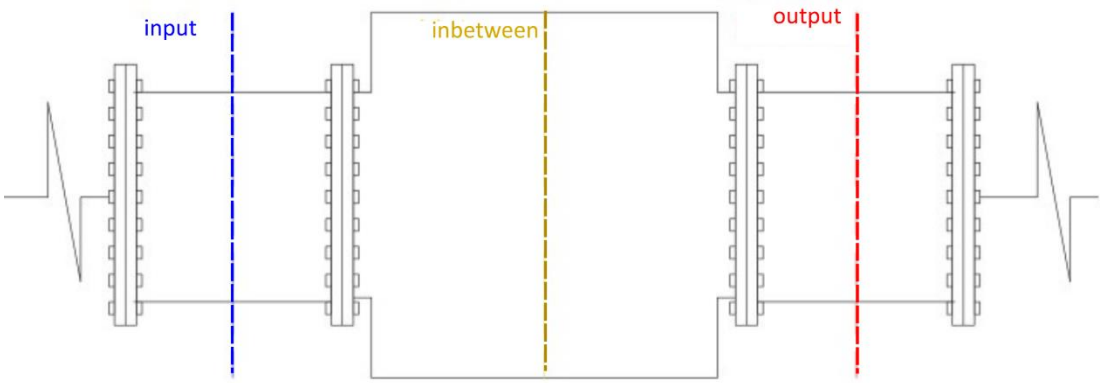

Figure 2.18. Diagram of the higher diameter discontinuity with the simulated outputs indicated.

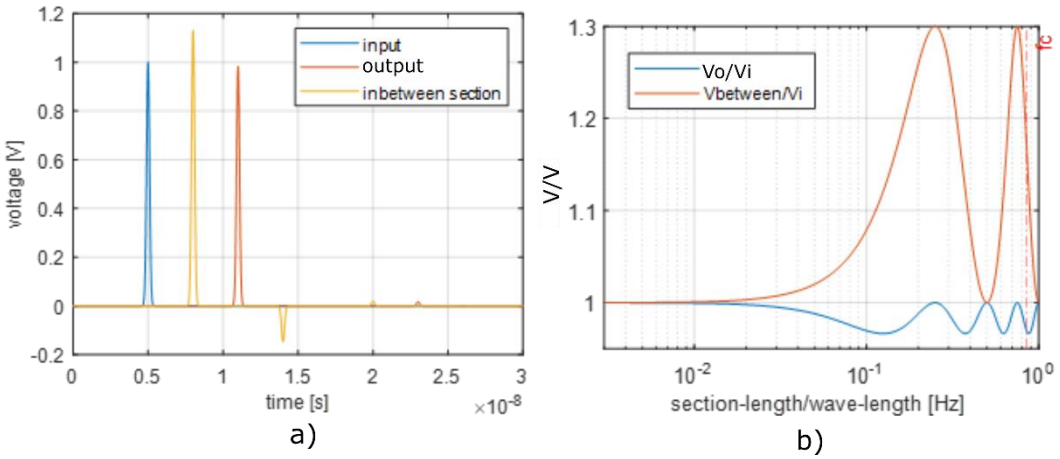

Figure 2.19. a) Incident and transmitted pulses in the time domain. b) Output and inbetween-discontinuity S_{21} parameter.

L-section

A typical section in a GIS is a 90° elbow, also known as an L-section, affecting the EM wave propagation. References [61], [65] and [68] agree that the L-section does not affect the signal below f_c. However, the current is not uniformly distributed immediately after the 90° turn; it takes some length to disperse equally in the transversal direction. A FEM simulation

was performed using Table 2.3 dimensions, where the input current was injected at the top port and measured in the left port from Figure 2.20 a). Figure 2.20 b) shows the current ratio between the top and bottom half of the enclosure: the current is uniformly distributed after 50 cm in any frequency; as the frequency increases, the current is more uniform at lower distances. However, above 100 MHz, the current loses its uniformity due to a change from TEM to TE mode. References [61] and [64] explain that the TEM mode is attenuated at high frequency by transforming into the TE mode.

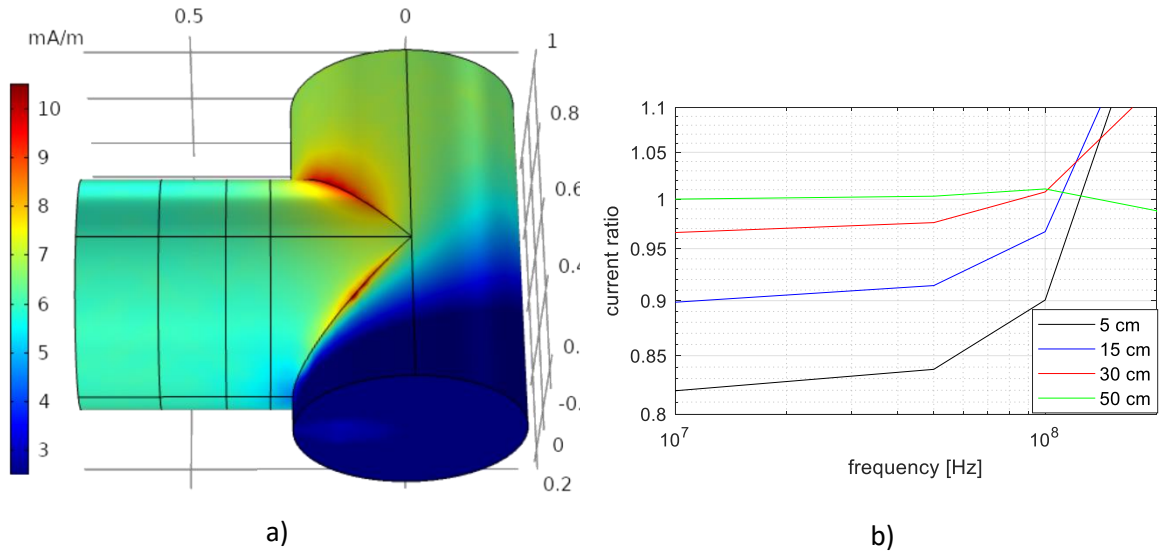

Figure 2.20. Current distribution after an L branch. a) FEM simulation and b) current ratio results for different lengths after the L-section.

The incident TE and TM modes have different propagation through the L-section depending on the frequency and position of the PD. Reference [61] shows a numerical simulation where the TE_{11} mode is highly reflected when the sensor and the PD have a relative position of 90°. Reference [63] displays a similar result, explaining that at the 0° position, the TE11 transform to the TEM mode. In the case of the TM mode, [61] concludes that this mode has lower attenuation because the longitudinal electric field component acts as a source for the magnetic field.

T-section

T-sections can be found in the GIS when the busbar is divided into two circuits. The EM wave below the TE cut-off frequency sees the T-section as the characteristic impedance of the other two ports in parallel. Since the characteristic impedance is the same in each port (2.34), using (2.35), the transition coefficient in each output port results in 0.66, in unison with [69]. For $f>f_c$, [64] and [65] agree that the T-section behaves like the L-branch in the 90° direction, with less attenuation in the straight direction. Additionally, using a high pass filter to guarantee a frequency beyond f_c, [69] shows a signal decrease of 40-50% for the turning direction and 20-30% for the straight direction.

$$Z_1 = Z_2 = Z_0 \rightarrow Z_2 || Z_3 = Z_0/2 \tag{2.34}$$

$$T = \frac{2Z_2||Z_3}{Z_1 + Z_2||Z_3} = \frac{2}{3} \tag{2.35}$$

Disconnecting switch

A disconnecting switch plays a crucial role in GIS and can be either a circuit breaker or a disconnector. When the switch is in an open state, the GIS changes from a coaxial to a circular waveguide, impacting the EM wave based on the propagation mode. The TEM mode requires both electrodes and cannot propagate in a circular waveguide. Nevertheless, studies by [56] and [66] indicate that the TEM signal isn't completely attenuated, and this attenuation varies with the gap length —I attribute this phenomenon to the flow of displacement current through the gap—. In contrast, the TE and TM modes can propagate in a circular waveguide, resulting in less attenuation.

Bushing

The bushing connects the GIS to the rest of the power system. Although limited information exists regarding the attenuation induced by a bushing, this termination significantly influences the signal propagation. In [62], the reflection coefficient for the 400 kV TUDelft GIS was computed, resulting in a value of 0.65. This calculation relied on the average area per data point. While this method does not distinguish between attenuation in different propagation modes, it does provide a qualitative understanding of the magnitude involved.

Summary

Table 2.5 shows a summary of the attenuation in different GIS discontinuities. The wave propagation is divided in the frequency range below and above the TE_{11} cut-off frequency (f_c). Below f_c, the wave propagation can be analysed as a transmission line covering the BW of the very high-frequency sensors. Above that frequency, the transmission line theory does not describe all propagation modes.

Table 2.5. Summary of the propagation characteristics in different discontinuities.

Discontinuity	$f<f_c$	$f>f_c$
Straight line	• Attenuation below 3dB/km. • Irregular current distribution near the source.	• TE attenuation below 4dB/km and TM below 10 dB/km • High attenuation when the sensor position relative to the PD source is 90°. • Attenuation of signal due to speed difference between propagation modes.
Spacer	• Attenuation depending on the spacer length and the characteristic impedance.	• Attenuation of signal due to speed difference between propagation modes. • Higher attenuation in bush-type than metal-type.
Change of diameter	• Attenuation depending on the discontinuity length and the characteristic impedance.	• Attenuated signal after the discontinuity. • Attenuated signal inside the discontinuity.
L-section	• Irregular current distribution near the change of direction.	• 0° relative position: Change of propagation mode. • 90° relative position: reflected wave.
T-section	• Irregular current distribution near the change of direction. • 33% of attenuation after the T-section	• 0° relative position: Change of propagation mode. • 90° relative position: reflected wave. • Higher attenuation in the 90° turn than in the straight part.
Disconnecting switch	• High attenuation, dependent on the gap length.	• Low attenuation, propagation in a circular waveguide.
Bushing	• high reflection due to the high characteristic impedance.	• reflection coefficient of 0.65 according to [62].

2.2.3. Unconventional Methods

The IEC 60270 method has proved very effective in electrically small objects. The standard assumes that the calibrator is connected to the terminals where the PD occurs, which holds for small objects that can be modelled as lumped elements. However, when the pulse wavelength is comparable to the device's length, the device under test behaves as a distributed element, causing the propagation of the PD pulses as in a TL. This results in a possible shift between the calibrator's connection point and the position of the defect [9]. This scenario is common in cables and long GIS, as depicted in Figure 2.21, where the defect is electrically far from the calibrator connection. Moreover, onsite GIS installations are typically connected to a cable or a transformer, rendering the live conductor inaccessible for the calibrator and the coupling capacitor (C_k) connection. Therefore, different measuring systems are required for such applications.

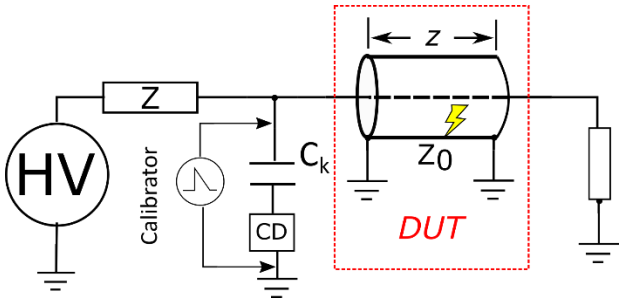

Figure 2.21. The IEC 60270 measuring circuit in a distributed element.

The challenges associated with measuring partial discharges in electrically long online devices have led to the development of alternative solutions, often referred to as unconventional methods. PDs generate electromagnetic waves, acoustic vibrations, light, and chemical products, which can be detected by various sensors. However, the IEC 62478 [11] and CIGRE [12] specifically address acoustic and electrical partial discharge measurement methods, including those for GIS.

Within the electromagnetic sensor spectrum, unconventional methods are categorised into HF/VHF and UHF ranges. The former relies on capacitive and inductive detection principles, while the latter utilises near-field antennas. Examples of HF/VHF sensors include capacitors, HFCTs, Rogowski coils, directional couplers, film electrodes, axial field couplers, transient earth voltage probes, and resistive couplers. Sensors on the UHF side include disc, cone-shaped, external windows, hatch, barrier couplers, field grading electrodes, and UHF antennas. The following table summarises the advantages and disadvantages of conventional and unconventional VHF and UHF methods in GIS.

Table 2.6. Summary of conventional and electromagnetic measuring systems for GIS.

	IEC 60270 (30-900 kHz)	HF/VHF (3-300 MHz)	UHF (0.3-3 GHz)
Calibrated measurement	yes	It is possible in theory (topic addressed in this thesis)	Not possible: a sensitivity check can be done
Installation for onsite substations	Complicated, it requires access to the live conductor	Yes	
Online monitoring	No, the calibration is done for the GIS without the rest of the power system.	Yes, the GIS can be considered independent of the rest of the power system because of the propagation time.	
Noise and disturbance immunity.	Bad, many power system transients at this frequency	Good, some power system transients are coupled	Best, works in frequency outside the range of the power system transients
PD Localisation	Very difficult	Good	Best, the higher frequency gives better resolution to the measurement
Waveshape determination	Not possible: too low and narrow frequency	Best, captures the pulse waveshape with a reasonable BW	Bad, affected by resonant effects
Cost	Low	Medium	High

This table is derived from the current state-of-the-art, highlighting distinct advantages within each frequency range. The present thesis concentrates on two aspects delineated in the table concerning VHF sensors: calibrated measurements and interference immunity. Through the enhancements introduced in this research, the very-high frequency methodology is expected to emerge as a viable candidate for partial discharge measurements and monitoring in gas-insulated systems.

2.3. Chapter Conclusions

An overview of partial discharge phenomena in gas-insulated systems is given. PD exhibits electrical characteristics that can be utilized for evaluating the level of degradation and for designing the measuring system. The dynamics of a PD depends on the insulation gas, pressure, and ageing, ranging from tens of picoseconds to a few nanoseconds. PD charge is the most employed parameter to determine the degradation level, with various charge estimation methods available. Gas-insulated systems are large electrical devices that cannot be modelled as lumped elements. In this context, energy propagates as a waveguide in the TEM, TE, and TM modes. In the TEM mode, the wave follows transmission line theory, where each GIS discontinuity is modelled as a change of impedance. The IEC 60270 standard is the established method for calibrated PD measurements. However, applying this conventional method in GIS can be challenging, necessitating unconventional methods, where the most

popular unconventional methods include UHF and VHF, with the latter being employed in this thesis due to its calibration possibilities.

3

"All the measurement in the world is useless if you don't make any changes based on the data".

- Amber Naslund

3. VHF Electric and Magnetic Sensors*

The previous chapter explained the phenomena to be measured and the measuring medium, leading to the core element of a measuring system, the sensor. The sensor, positioned as the initial element in data acquisition, is responsible for detecting the signal of interest that will undergo signal processing. As established in the previous chapter, the conventional method for partial discharge is impractical for monitoring GIS, leading to the proposition of unconventional methods. VHF sensors, positioned between conventional and UHF sensors, offer advantages from both frequency ranges.

This thesis focuses on VHF derivative sensors, encompassing both inductive and capacitive types. The electric and magnetic couplers sense TEM waves propagating in the GIS as electrostatic and magnetostatic fields, as depicted in Figure 3.1. The magnetic sensor captures the changing magnetic field produced by the current surrounding the mounting hole,

*This chapter is based on the following publications:

- C. M. Escurra and A. R. Mor, "Test Bench and Frequency Response of a Magnetic Antenna used in GIS PD Measurements," in 2021 Electrical Insulation Conference, EIC 2021, 2021, no. 2, pp. 269–272. doi: 10.1109/EIC49891.2021.9612372.
- C. Mier, A. R. Mor, and P. Vaessen, "Design and Characterization of a Magnetic Loop Antenna for Partial Discharge Measurements in Gas Insulated Substations," IEEE Sensors Journal, vol. 21, no. 17, pp. 18618–18625, 2021, doi: 10.1109/JSEN.2021.3089084.
- C. M. Escurra and A. R. Mor, "Balanced Magnetic Antenna for Partial Discharge Measurements in Gas-Insulated Substations," in 2022 9th International Conference on Condition Monitoring and Diagnosis, CMD 2022, 2022, pp. 509–512, doi: 10.23919/CMD54214.2022.9991698.
- C. Mier, A. Rodrigo Mor, L. Castro, and P. Vaessen, "Magnetic and electric antennas calibration for partial discharge charge estimation in gas-insulated substations," International Journal of Electric Power Energy Systems, vol. 141, no. January, p. 108226, 2022, doi: 10.1016/j.ijepes.2022.108226.

while the electric sensor captures the changing electric field produced by the voltage between the inner conductor and the sensor.

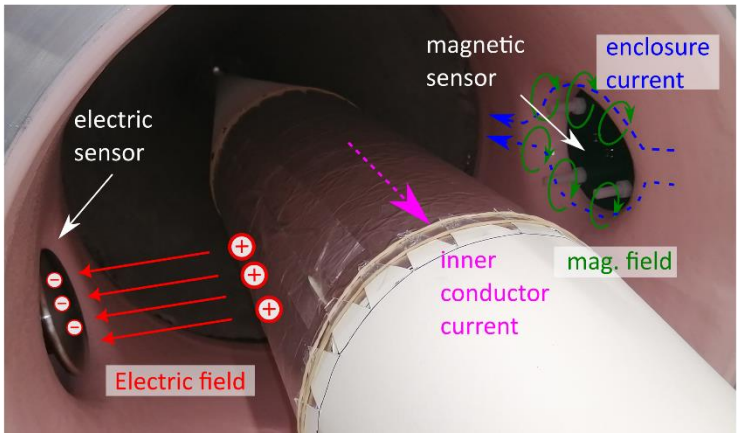

Figure 3.1. Illustration of electromagnetic fields coupled to electric (left) and magnetic (right) sensors in the GIS, showing the inner conductor current (pink arrow), the enclosure current (blue arrows), the mounting hole's magnetic field (green arrows), and the charges induced in the electric coupler (red dots), [31].

While both sensors operate within the VHF range, their distinct physical principles give them differences in terms of gain, bandwidth, SNR and power-frequency electric field grading. The gain determines the amplitude of the measured signal, and the BW dictates the sensors' frequency operation, with both aspects being influenced by the electric parameters of the sensors. The SNR quantifies the strength of the signal of interest relative to the noise and is influenced by the gain and BW. Finally, the shielding of the power-frequency electric field is detrimental to HV applications, leading to the introduction of the electric sensor, which is later combined with the magnetic sensor in Chapter 4.

This chapter first outlines the test setup for characterizing the sensors to determine their respective gains and bandwidths. Subsequently, the magnetic sensor and its various versions are described, modelled, and measured in both the frequency and time domains. Then, the analysis developed for the magnetic sensor is extended to the electric sensor. Finally, the results of both sensors are discussed in the conclusions. The analysis of the electric and magnetic sensors in this chapter sets the stage for the following chapter, which combines both sensors for an enhanced measuring system.

3.1. TEM Testbench

One of the many physical phenomena a PD produces is the propagation of electromagnetic waves. The GIS acts as a coaxial waveguide with three propagation modes: transverse electromagnetic, transverse electric and transverse magnetic. The TE and TM have a cut-off frequency which depends on the geometry of the cross-section of the GIS. The previous chapter discussed that extracting the charge magnitude from ultra-high frequency signals in a GIS is impossible. Therefore, a measuring system operating solely in the TEM mode must be used for charge estimation.

A TEM testbench was designed to characterize the VHF sensors in the transverse electromagnetic mode. The sensors' Transfer Function (TF) is estimated by measuring the output and input signal in the desired frequency ranges with a Vector Network Analyzer (VNA). VNAs and oscilloscopes have inputs with an impedance of 50 Ω. Thus, the characteristic impedance through the whole testbench must be maintained to transfer the energy without any reflections, matching the testbench to 50 Ω. Considering the GIS as a coaxial line, the relation between the outer (b) and inner (a) diameter conductors in (3.1) must be 2.3:1.

$$Z_0 = \sqrt{\frac{\mu}{\varepsilon}} \frac{ln\left(b/a\right)}{2\pi} \tag{3.1}$$

The TEM propagation is obtained by a smooth transition of each element in the testbench. The signal is transmitted from the VNA to the GIS through a N-type connector. This connector has a small diameter compared to the GIS's diameter; thus, a smooth transition must be implemented between them. A transition cone, which grows from the diameter of the N-type connector to the diameter of the GIS, is used for this purpose. The smoothness of the transition depends on the length of the cones, where a large cone gives a better transition.

The testbench was built to resemble a real GIS. A straight GIS enclosure section measuring 360 mm in length and 415 mm in diameter was used. The transition cones were handcrafted in a workshop: the inner conductor was assembled with cylindrical and conical paperboard covered with aluminium foil, making it lightweight to be solely supported by the pin of the N-type connector, as shown in Figure 3.2 a). The outer cone was hand-rolled using a 1 mm-thick aluminium sheet, and an aluminium flange was welded in the base and vertex of the cones. The result is shown in Figure 3.2 b).

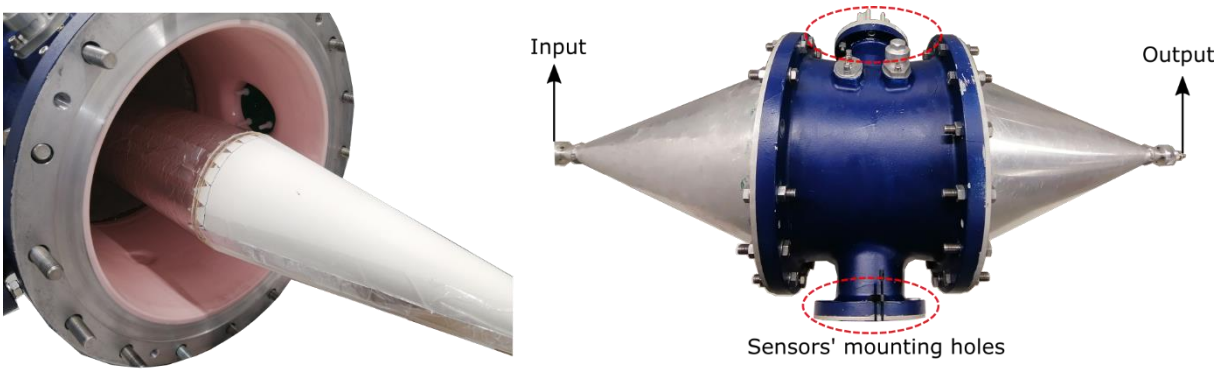

Figure 3.2. a) Inner conductor construction for the TEM testbench. The cylindrical section has the aluminium foil on the outside, and the conical part has the aluminium foil on the inner surface. b) Assembled TEM testbench, [31].

This testbench can be used for frequency and time domain measurements. Figure 3.3 a) shows the testbench dimensions and the configuration used for the frequency analysis. One cone's termination is connected to the VNA input, and the other one is terminated to a 50 Ω load. Another VNA port connects the sensor through a signal conditioning device (filter and amplifier). A similar test setup is built for measurements in the time domain, as shown in

Figure 3.3 b), where the cone input and sensor's output are connected to an oscilloscope, while a pulse source is connected to the other cone.

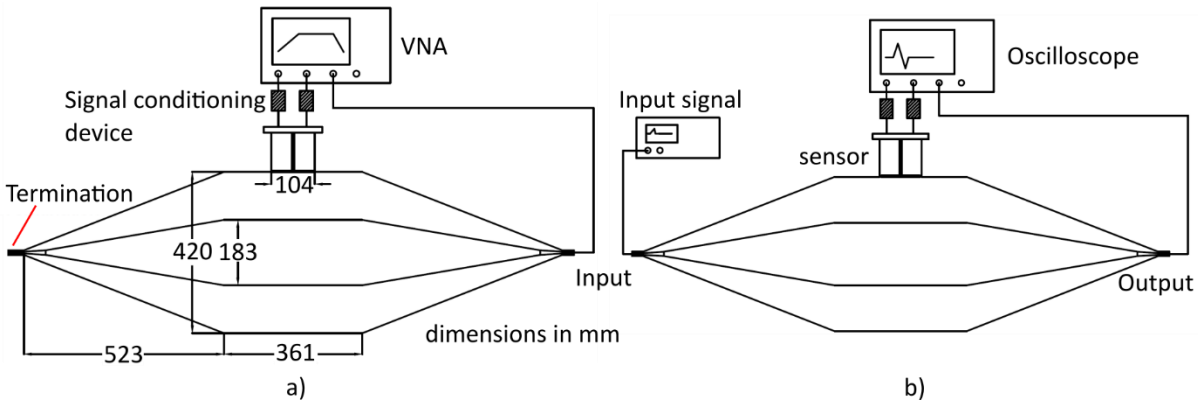

Figure 3.3. a) Frequency and b) time domain test setups in the TEM testbench, [27].

Figure 3.4 illustrates the frequency response of the testbench using a ROHDE&SCHWARS ZVB4 (300KHz-4GHz) VNA. The transmission parameter (S21) is above -1dB up to 1 GHz, covering the frequency of interest for the sensors. The phase plot shows a shift at 10 MHz because of the signal's time delay, which can be corrected using (3.2), where *l* is the length between the N-type connector input and the sensor, *c* is the speed of light in vacuum, *f* is the frequency, and φ is the phase delay.

$$\varphi = 2\pi f \sqrt{\epsilon} \frac{l}{c} \tag{3.2}$$

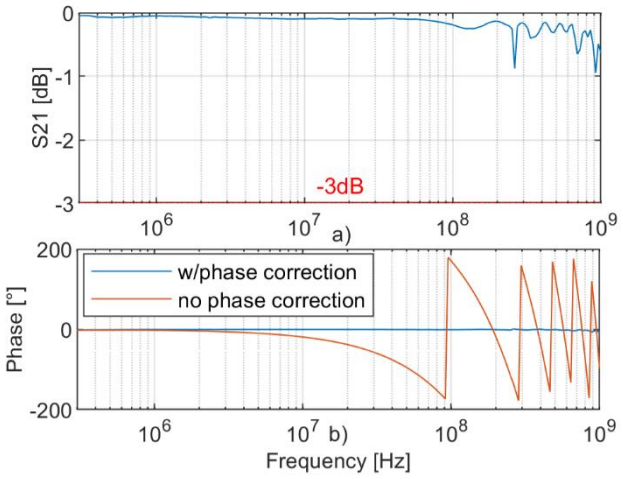

Figure 3.4. Testbench frequency response, [71].

This testbench is matched to 50 Ω within 1 GHz frequency spectrum, offering a reflection-free setting for the sensors and the signal conditioning devises' characterization in the frequency and time domain (Chapter 3). Furthermore, this testbench is used in the thesis for testing the suppression of reflections (Chapter 4), the calibration process (Chapter 5) and the interference discrimination technique (Chapter 6).

3.2. The Magnetic Sensor

In a GIS, PD pulses flow uniformly in the inner layer of the enclosure. Reference [23] demonstrates that this current induces a magnetic field at the GIS mounting holes (Figure 3.5), which can be picked with a magnetic loop.

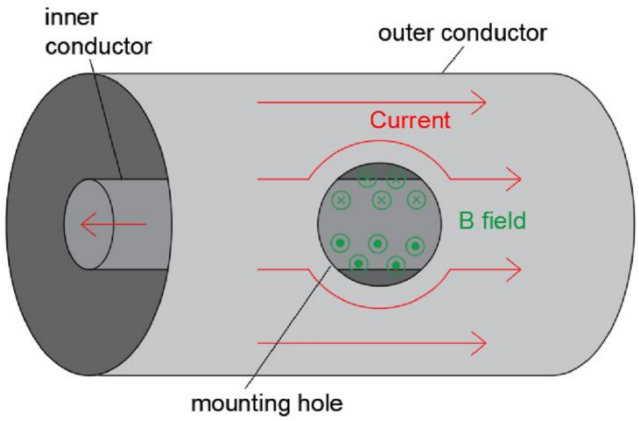

Figure 3.5 PD's magnetic field induced in the GIS's mounting hole, [27].

Single loop sensors are designed for radio-frequency applications, with two configurations: unshielded and shielded magnetic antennas. The unshielded magnetic loop sensor is described in Figure 3.6 a), consisting of a loop printed in a PCB, with the loop terminals connected to an SMA connector. The shielded magnetic loop sensor consists of a shielded loop made of RG174A-U coaxial cable. At the loop's termination, the inner conductor is connected to the coaxial cable's shield, and the outer conductor is open-circuited (Figure 3.6 b)). In both sensors, the shield of the feeder coaxial cable is grounded to the mounting hole lid.

The magnetic loop sensor is designed to capture the maximum amount of magnetic field produced by the PD. Using the Finite Element Method simulation in [23] and via experimentation, it was found that most of the PD current flows through the upper edge of the neck (illustrated in red in Figure 3.6 b)); hence, the sensor is levelled to this plane. The dimensions are shared for both sensors and are indicated in Figure 3.6 a). In the case of the shielded loop, the gap between the open circuit and the feeder cable is about 10 mm.

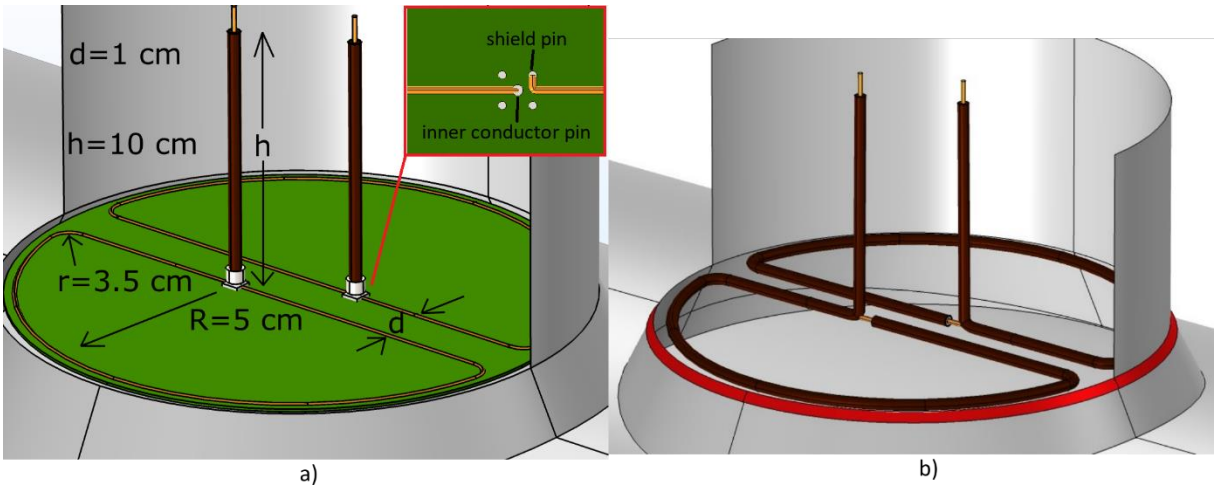

Figure 3.6. Illustration and dimensions of a) unshielded and b) shielded magnetic loop sensor, [27].

3.2.1. Unbalanced Loop

Unshielded mathematical model

A single unshielded loop sensor follows the same model as a current transformer but without a core and with a single turn. Figure 3.7 shows the electric circuit of the magnetic sensor. The PD current (I_{pd}) that flows around the mounting hole is coupled (M) to the sensor. Then, the current generated in the sensor induces an opposing voltage represented as a self-inductance (L), with a parasitic capacitance (C) in parallel between the loop and the grounded GIS enclosure. This loop is connected to a load (R), where the output voltage (V_o) is measured. The equation representing the time domain circuit is (3.3), and the transfer function corresponding to this equation is (3.4), relating the output voltage, V_o, with the PD current, I_{pd}. Equation (3.4) is the typical response of a derivative sensor with a zero and two poles. The sensor's small diameter of 10 cm allows the lumped element model to cover the VHF range.

$$\frac{di_{pd}(t)}{dt} = \frac{LC}{M}\frac{d^2v_o(t)}{dt^2} + \frac{L}{RM}\frac{dv_o(t)}{dt} + \frac{v_o(t)}{M} \tag{3.3}$$

$$H(s) = \frac{\boldsymbol{V}_o(s)}{I_{pd}(s)} = \frac{sM}{s^2LC + s\,{}^{L}/_{R} + 1} \tag{3.4}$$

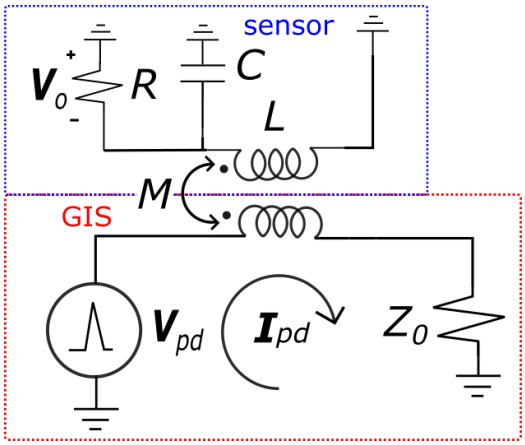

Figure 3.7. Unshielded loop electric circuit.

Shielded mathematical model

To improve the electromagnetic compatibility of loop sensors, radio-frequency applications shield the loop of the sensor [72]. Shielding the bare conductor adds an additional transmission line to the sensor. Considering the 30 cm loop length, a lumped element model is valid below 100 MHz. To extend the frequency range of this model, the shielded loop is treated as a transmission line.

According to [70] and [71], when the current depth of penetration is less than 10% of the shield thickness, the external magnetic field only induces Electromotive Force (EMF) in the outer layer of the shield; hence, the inner layer of the shield and the inner conductor of the coaxial line do not interact with these external fields. However, the voltage at the gap terminals (V_1) is seen by the inner layer sheath and the inner conductor (Figure 3.8).

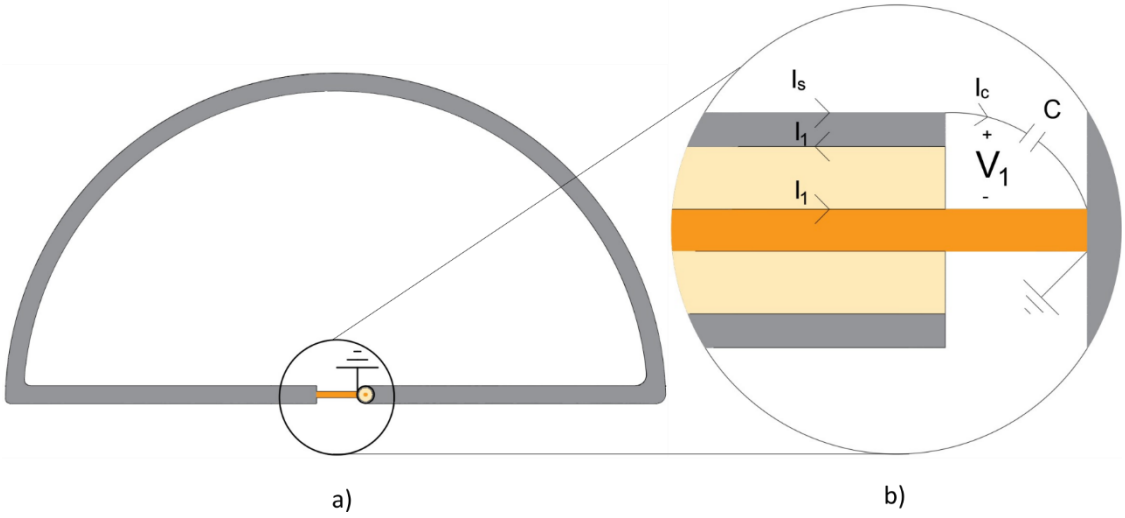

Figure 3.8 a) Shielded loop top view. b) Amplification of the inner conductor connected to the feeder shield, [27].

Following the previous explanation, Figure 3.9 illustrates the electric circuit of the shielded loop. The outer shield current mesh, coloured in red, is represented by (3.5), where $\boldsymbol{V}_{in}$ is the voltage source resulted from the PD current ($\boldsymbol{I}_{pd}$) and the sensor's mutual inductance (M) (3.6); L_s is the self-inductance of the outer shield; and $\boldsymbol{V}_c$ is the gap voltage due to the capacitance C, (3.7).

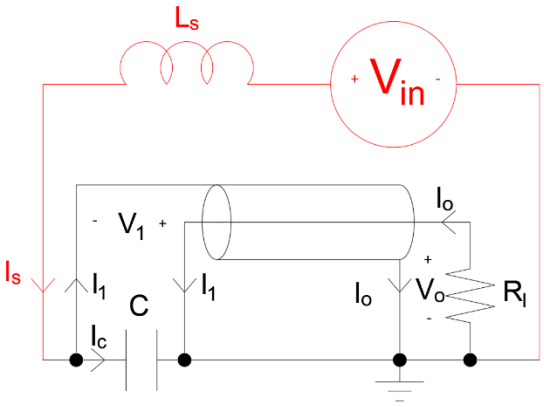

Figure 3.9. Electric circuit diagram of the shielded loop sensor, [27].

$$\boldsymbol{V}_{in} = j\omega L_s \boldsymbol{I}_s + \boldsymbol{V}_c \tag{3.5}$$

$$\boldsymbol{V}_{in} = j\omega \boldsymbol{I}_{pd} M \tag{3.6}$$

$$\boldsymbol{V}_c = -\frac{j\boldsymbol{I}_c}{\omega C} \tag{3.7}$$

At the gap, the shield current is divided between the gap capacitance and the inner layer of the shield (3.8). The gap capacitance and the coaxial cable input share the same voltage but with opposite polarity (3.9). This coaxial input voltage (V_1) is equal to the inner layer current (with opposite polarity) and the input characteristic impedance (Z_{in}), (3.10), where Z_{in} is equal to (3.11).

$$\boldsymbol{I}_s = \boldsymbol{I}_1 + \boldsymbol{I}_c \tag{3.8}$$

$$\boldsymbol{V}_c = -\boldsymbol{V}_1 \tag{3.9}$$

$$\boldsymbol{V}_1 = -\boldsymbol{I}_1 Z_{in} \tag{3.10}$$

$$Z_{in} = Z_0 \frac{R + jZ_0 tan(\beta l)}{Z_0 + jR tan(\beta l)} \tag{3.11}$$

The voltage at any point of the coaxial cable is calculated with (3.12). Where z is the distance propagated in the coaxial cable; β is the propagation constant for a lossless line and is equal to $\beta=\omega Z_0 C_c$; C_c is the capacitance per unit length; and Z_0 is the characteristic impedance of the coaxial cable. Additionally, Γ_l is the voltage reflection coefficient at the load's terminals and is calculated with (3.13). When (3.12) is analysed at the total length of the line ($z=l$) and at the start of the coaxial cable ($z=0$), it results in (3.14) and (3.15), respectively, where $\boldsymbol{V}_o$ is the voltage at the load R.

$$\boldsymbol{V}(z) = \boldsymbol{V}_0{}^{+}\left(e^{j\beta z} + \Gamma_l e^{-j\beta z}\right) \tag{3.12}$$

$$\Gamma_l = \frac{Z_l - Z_0}{Z_l + Z_0} \tag{3.13}$$

$$\boldsymbol{V}(l) = \boldsymbol{V}_0{}^{+}\left(e^{j\beta l} + \Gamma_l e^{-j\beta l}\right) \tag{3.14}$$

$$\boldsymbol{V}(0) = \boldsymbol{V}_o = \frac{V_1(1+\Gamma_l)}{(e^{j\beta l} + \Gamma_l e^{-j\beta l})} \tag{3.15}$$

By substituting equations (3.9) into (3.7) and (3.8) and (3.10) into (3.5), we get (3.16). Then, by replacing (3.7) and (3.15) into (3.16) and rearranging, the transfer function results in (3.17). If $R=Z_0$, the previous equation is reduced to (3.18), giving a similar result to the TF of the unshielded sensor (3.4), with two exceptions: a time delay caused by the coaxial loop and a change of polarity of the output signal.

$$V_{in} = -j\omega L_s \frac{V_1}{Z_{in}} + \omega^2 L_s C V_1 - V_1 \tag{3.16}$$

$$\frac{V_o}{I_{pd}} = \frac{-j\omega M(1+\Gamma_l)}{\left(1 + {}^{j\omega L_s}/_{Z_{in}} - \omega^2 L_s C\right)(e^{j\beta l} + \Gamma_l e^{-j\beta l})} \tag{3.17}$$

$$\frac{V_o}{I_{pd}} = -\frac{j\omega M e^{-j\beta l}}{-\omega^2 L_s C + {}^{j\omega L_s}/_{R} + 1} \tag{3.18}$$

The magnetic loop consists of two symmetrical lobes (Figure 3.6). One lobe induces a back EMF in the other and vice versa. Since the current in each lobe is equal, the induced back EMF can be represented by an increase in the self-inductance, raising an apparent self-inductance, $L_s=L_{self} + M_{lobes}$, where L_{self} is the self-inductance of the loop, and M_{lobes} is the mutual inductance between the lobes. Consequently, the magnetic coupling between the lobes of the sensor can be accounted for (3.4) and (3.18) using the apparent self-inductance L_s.

All the values from the model can be estimated by experimentation:

- **Mutual inductance (M):** reference [56] shows that the mutual inductance value approximates the TF's slope at low frequencies. By injecting a low-frequency sinusoidal into the GIS and measuring it at the sensor's output, the mutual inductance is calculated using (3.19).

$$H(\omega) = \frac{V_o(\omega)}{I_{pd}(\omega)} = j\omega M \quad when\ \omega \to 0\ rad/s \tag{3.19}$$

- **Apparent self-inductance (L_s):** it is calculated by loading the sensor with a known capacitor (C_l) and measuring the resonance frequency. The calculation depends on the capacitor's location. The apparent self-inductance is calculated with (3.20) when the capacitor is connected at the shield gap. However, if it is in parallel with the load (R), (3.18) must be used, replacing R with the equivalent parallel impedance of R with the reactance of C_l. When a sufficiently big capacitor is used, the resonance occurs at a frequency where the wavelength is ten times bigger than the transmission line length. Therefore, the coaxial cable can be considered a lumped inductance and capacitance, resulting in an apparent self-inductance equal to (3.21).

$$L_s = \frac{1}{C_l \omega^2} \tag{3.20}$$

$$L_s = \frac{1}{(C_l + C_c)\omega^2} - Z_0{}^2 C_c \tag{3.21}$$

- **Mutual inductance between lobes (M_{lobes}):** is calculated using (3.19) by injecting a sinusoidal voltage on one lobe and measuring at the other.

- **Gap capacitance (C):** The gap capacitance is complicated to measure; however, by doing a FEM and by analytical calculation according to [74], an approximate value is obtained.

Table 3.1 shows the electric circuit parameters of the unbalanced loop sensors.

Table 3.1. Electric circuit parameters of unbalanced loop sensors.

Parameter	Shielded Sensor	Unshielded Sensor
Mutual inductance (M)	0.96 nH	0.96 nH
Apparent self-inductance (L_s)	170 nH	290 nH
Mutual inductance between lobes (M_{lobes})	35.0 nH	30.0 nH
Self-inductance (L_{self})	135 nH	260 nH
Gap capacitance (C)	0.1-1.0 pF	Not applicable

Unbalanced loop sensors' measurements

The sensors' frequency and time domain measurements were obtained using the TEM testbench. Figure 3.10 a) and b) compare the magnitude and phase of the two sensors. The sensors' outputs were connected to 25 dB, 1 GHz bandwidth, 50 Ω matched voltage amplifiers. The sensors show a slope in the low-frequency range due to the mutual inductance between the GIS's mounting hole and the loop. After some tens of MHz, the sensor reaches the cut-off frequency influenced by the loop's self-inductance and the load impedance. The shielded loop has a thicker conductor than the unshielded one, giving lower self-inductance and, thus, higher gain. Another notable result is the resonances at 150 MHz and 200 MHz for the shielded and unshielded sensors, respectively. Other resonances appear at higher frequencies but are above the TEM propagation mode.

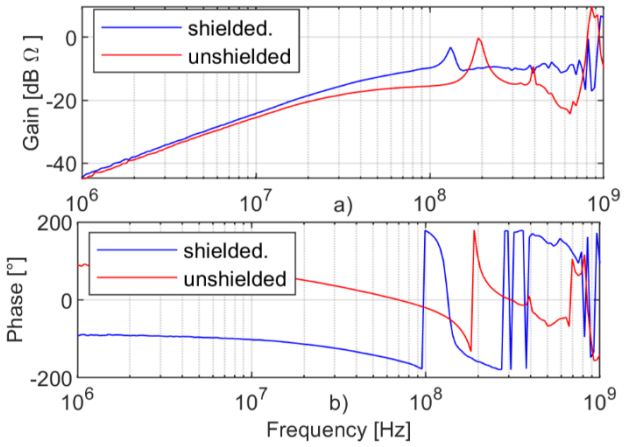

Figure 3.10. Shielded and unshielded loop sensors' frequency response: a) magnitude and b) phase, [75].

The authors in [21] show that it is possible to discriminate interference from PD signals by using symmetric lobes in each half of the mounting hole. Figure 3.11 illustrates the symmetry of the measurements using a UHF pulse calibrator with a rise time of 640 ps. An intentional delay between signals was introduced to better visualize the results in the time domain. Figure 3.11 a) and b) show the measured pulses for the shielded and unshielded sensors, respectively. The unshielded sensor presents more oscillation than the shielded sensor; this extra oscillation is attributed to an external electric field coupled to the sensor.

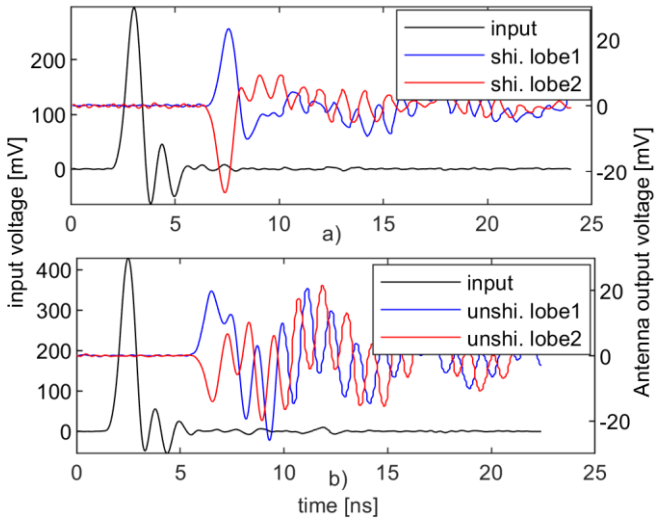

Figure 3.11. UHF pulse measured with symmetric lobes in a) shielded and b) unshielded magnetic sensors, [75].

Figure 3.12 shows the Fast Fourier Transform (FFT) of the shielded output. The resonance at the same frequency as in Figure 3.10 demonstrates that the oscillation is a product of the sensor's resonance. This oscillation is attributed to the series resonance between the GIS capacitive coupling and the sensor's self-inductance. The common-mode current that flows in the sensor at the resonance frequency is identified in other loop antenna applications shown in [76]. Following up are some reasons that support the previous

hypothesis about the series resonance between the GIS capacitive coupling and the sensor's self-inductance:

- When the aluminium lid of the mounting hole is replaced by plastic, the resonance disappears; there is no conductive path for the CMC to circulate.
- If the sensor is rotated 90°, no voltage is induced in the loop [23]. However, the resonance is maintained at almost the same frequency because the capacitance and the self-inductance do not change. Figure 3.13 shows that the amplitude and phase of the sensor are the same, irrespective of the rotation.
- If the sensor is moved further inside the mounting hole, the resonance frequency is shifted due to the change in the coupling capacitance.

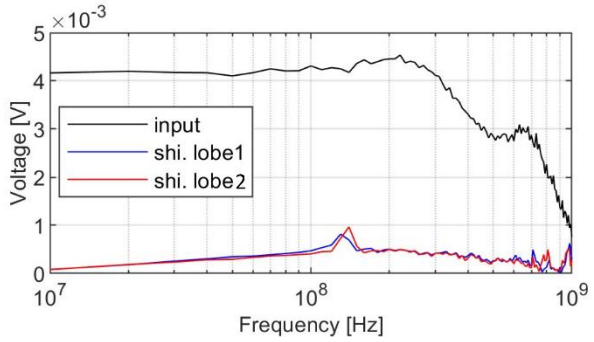

Figure 3.12. FFT of the input pulse and shielded sensor's output, [75].

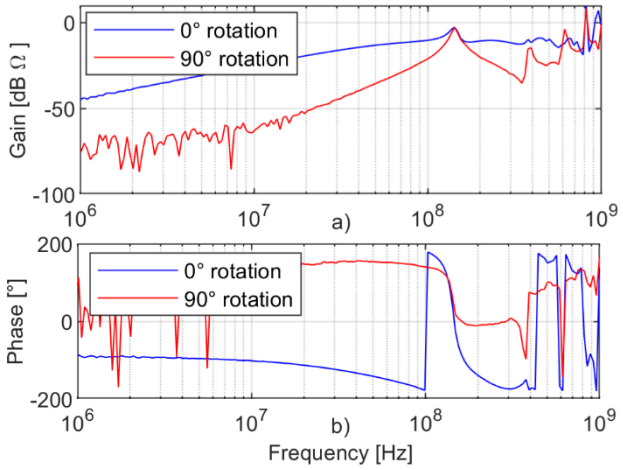

Figure 3.13 Bode plot of the sensor positioned at 0° (in blue) and 90° (in red), a) magnitude and b) phase, [75].

The CMC was reduced by employing a ferrite bead clamped in the feeder coaxial cable (see Figure 3.14). At the resonance frequency, the CMC flows through the feeder cable, inducing a magnetic field in the ferrite and eliminating the resonance (Figure 3.15).

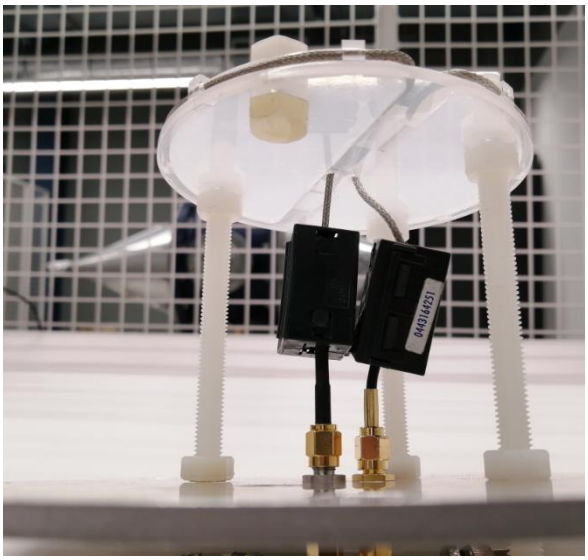

Figure 3.14. Picture of the ferrites clamped in the sensor's feeder cables, [75].

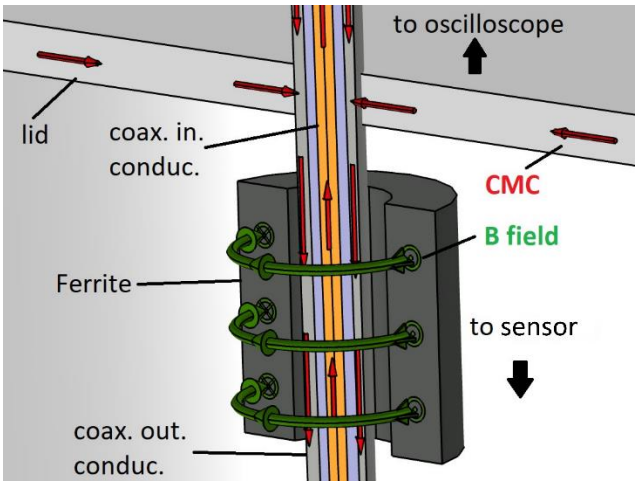

Figure 3.15. Magnetic field induced in the ferrite due to the common-mode current, [75].

The comparison with and without the ferrite was done in the frequency and time domain. Figure 3.16 shows the frequency response for the unshielded and shielded sensors with the implementation of the ferrite. A Fair-Rite ferrite (part number: 443164251) was used, inducing almost 300 Ω at the resonance frequency. As a result, no resonance is observed below 300 MHz in Figure 3.16. Figure 3.17 shows the sensors' response to the UHF calibration pulse using the ferrite a) without filter and b) with a 250 MHz 1st-order LPF. By filtering the signal, higher frequency resonances are eliminated. However, filtered pulses are slower, overlapping with reflected pulses near a discontinuity in a full-scale GIS. Therefore, the BW of the filter must be properly analysed to produce a signal with enough sensitivity and time resolution.

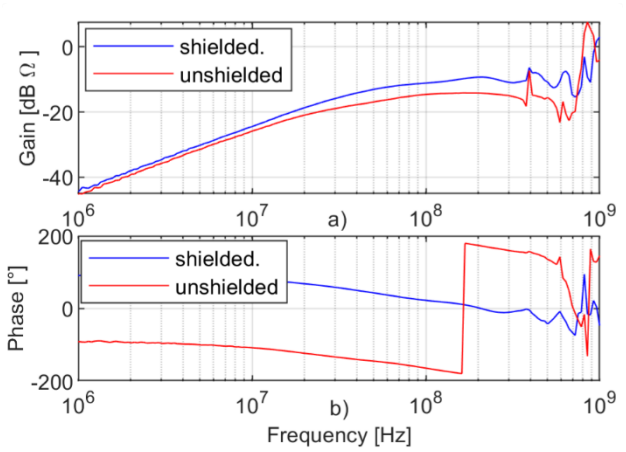

Figure 3.16. Frequency response of shielded and unshielded loop sensor using a ferrite: a) magnitude, and b) phase, [75].

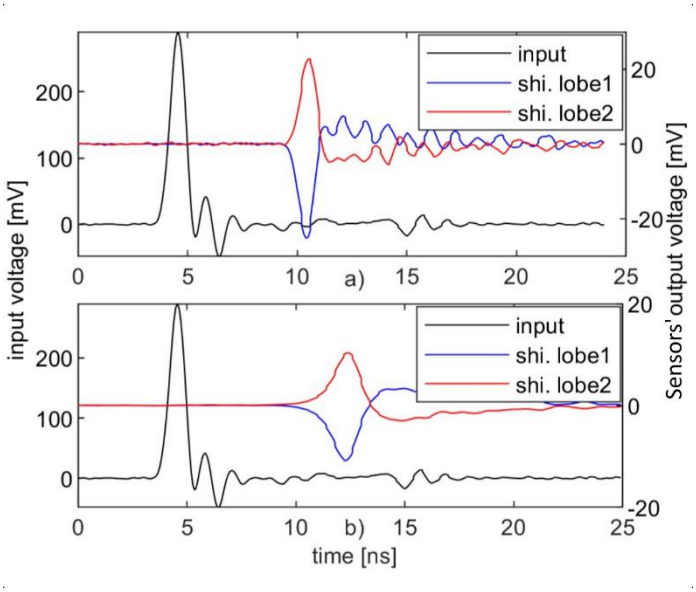

Figure 3.17. Time domain response of a shielded loop sensor to a UHF pulse, using a ferrite a) without filter and b) with a 250 MHz LPF, [75].

It is worth mentioning that (3.18) does not consider the CMC, so no resonances are modelled. Figure 3.18 compares the shielded loop with the ferrites and the proposed model in (3.18), having a similar magnitude and phase in the VHF range. Figure 3.19 compares the measured and computed output signals with a 270 MHz, 1st order LPF for a) a σ=25 ns Gaussian input pulse and b) the UHF calibrator. The simulated output pulses closely resemble the measurements, validating the mathematical model.

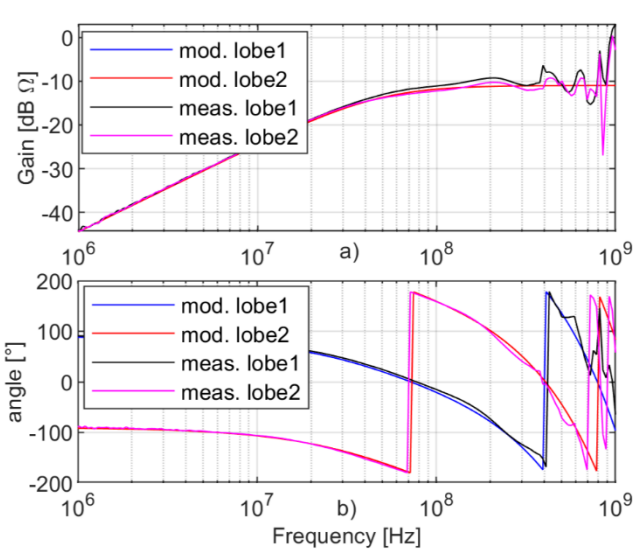

Figure 3.18 a) magnitude and b) phase comparison between measurements and model of the shielded loop, [75].

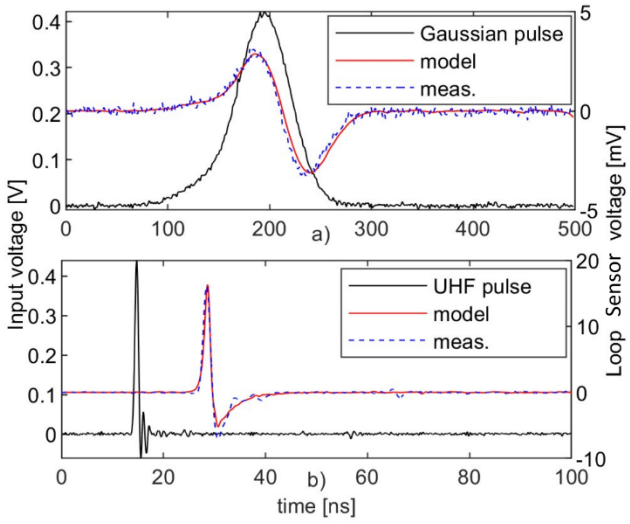

Figure 3.19 Comparison between measurement and model for a) a σ=25 ns Gaussian input pulse and b) the UHF input pulse, [75].

3.2.2. Balanced Loop

Balanced Shielded Loops (BSL) are well known in radio transmission applications and are characterized for having good common-mode rejection [73], sensing magnetic fields while rejecting electric fields. Reference [76] describes how the gap location in the shielded loop determines the effectiveness of the CMC rejection. A balanced shielded sensor is obtained when the gap is located in the middle of the loop (Figure 3.20 a)), while the sensor presented in the previous section consisted of a "lateral-gap" structure (Figure 3.20 b)), which is a type of Unbalanced Shielded Loop (UBSL).

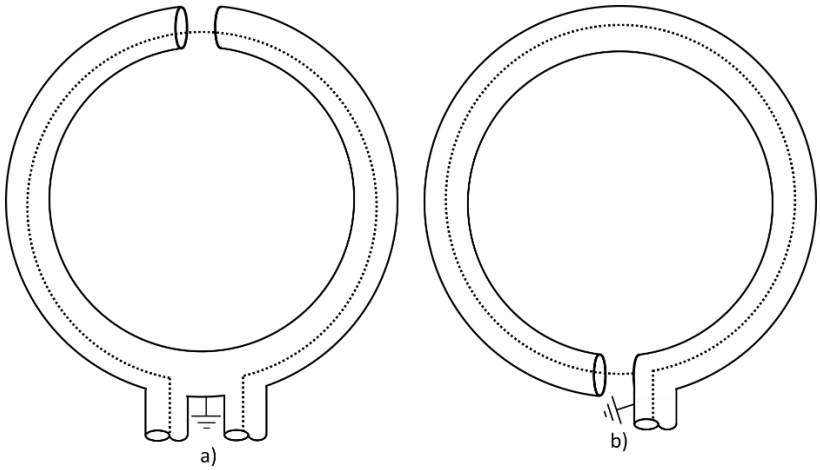

Figure 3.20 a) Balanced-gap and b) lateral-gap magnetic loop configurations.

The mathematical model of a balanced shielded loop can be derived similarly to the unbalanced one. The electric circuit of the BSL is shown in Figure 3.21. By neglecting the gap capacitance, the TF results in (3.22). The BSL divides the loop into two equal arms, resulting in two outputs with the same equation as the UBSL but with half coupling inductance, half self-inductance, half TL length and opposite polarity.

$$\frac{V_o}{I_{pd}} = \pm \frac{j\omega {}^{M}/_{2}\, e^{-j\beta l/2}}{1 + {}^{j\omega L_s}/_{2R}} \tag{3.22}$$

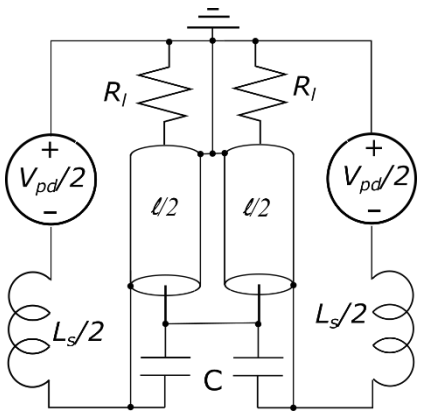

Figure 3.21 Balanced shielded loop electric diagram, [28].

Common-mode currents

The magnetic sensors are intended to measure only the magnetic field; however, the electric field is also induced, producing common-mode currents. In the BSL, the CMC are divided equally (same magnitude and phase) in the loop arms, creating a zero magnetic field: Figure 3.22 a). In the UBSL, each arm has a different length with a different inductance and capacitance, dividing the CM current unevenly and inducing a magnetic field in the loop Figure 3.22 b). The purpose of the BSL configuration is to eliminate the residual CMC that remained in the sensor even with the ferrites.

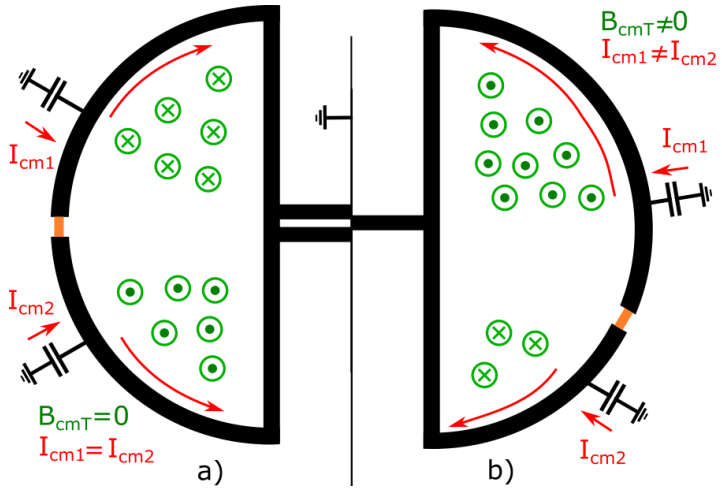

Figure 3.22 CMC and induced magnetic field in a) BSL and b) UBSL, [28].

Eight-shaped sensor

Equation (3.22) shows that the BSL's coupling inductance is reduced by half compared to the UBSL. One way to double the BSL's coupling is by increasing the loop area using the complete mounting hole's area. In a circular shape, no total magnetic field is coupled because it has opposite polarity in each half area of the mounting hole [23]. By shaping the loop as an "eight", the magnetic field in each half contributes to the total induced electromotive force. Figure 3.23 illustrates how the PD current (I_{pd}) splits when encountering the GIS's mounting hole, producing a magnetic field (B_{pd}) with opposite polarity in each half of the mounting hole, resulting in a total electromotive force in the eight-shaped path.

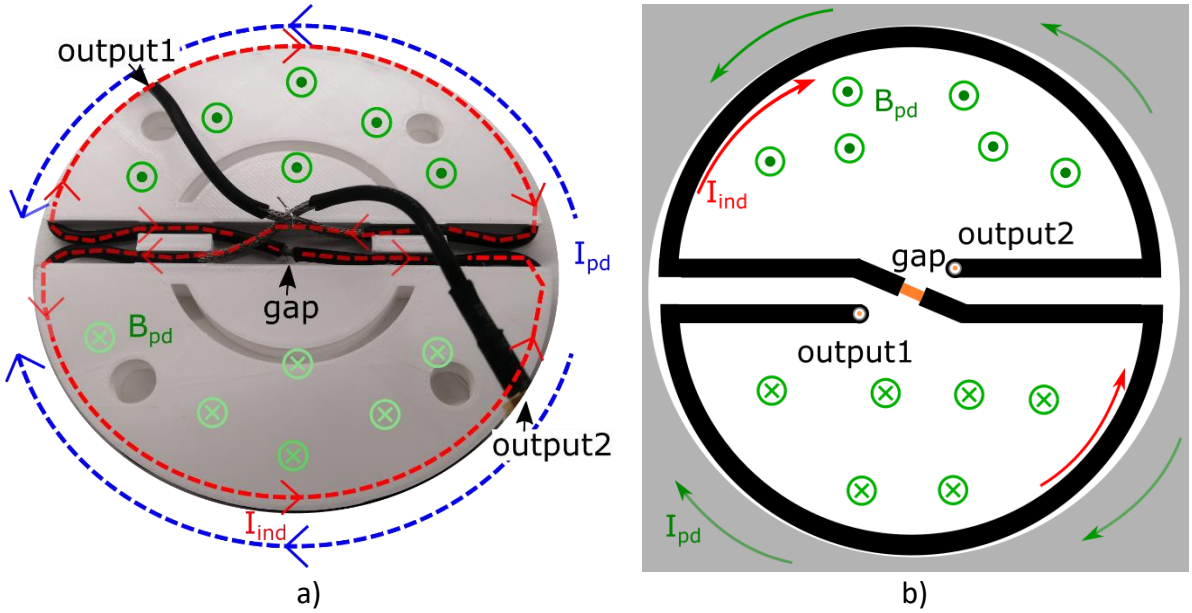

Figure 3.23 Eight-shaped BSL sensor showing the PD current, the induced magnetic field, the induced current, the outputs and the gap, [28].

Figure 3.24 shows a picture with the dimensions of the 8-shaped loop, and Table 3.2 shows its electric parameters compared with the balanced single lobe. The magnetic coupling of the 8-shaped loop is lower than the unbalanced one due to the smaller loop area. This

smaller loop area was chosen to fit the sensor in the mounting hole of the testbench and the one of the full-scale GIS, which is smaller.

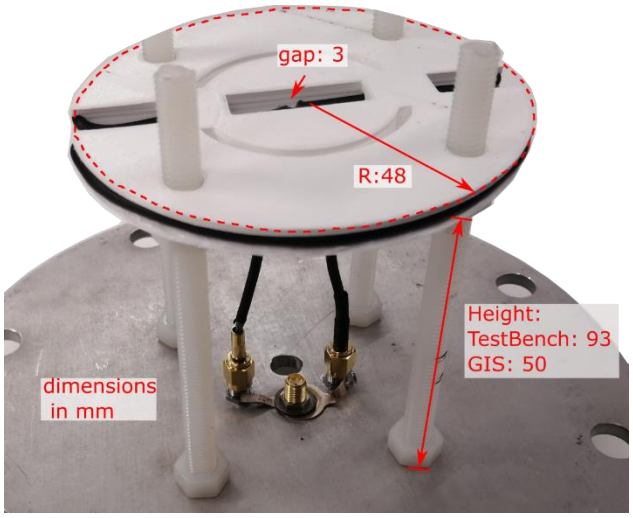

Figure 3.24. Picture and dimensions of the 8-shaped magnetic loop for the testbench, [30].

Table 3.2 8-shaped magnetic loop electric parameters using the dimensions in Figure 3.24.

	Balanced loop	8-shaped balanced loop
M	0.34 nH	0.72 nH
Ls	79 nH	160 nH

Balun

The BSL's design has two outputs with opposite polarity. The output signal can be doubled by measuring inner conductors and subtracting them. A balun transformer is an analogic solution without signal processing. Figure 3.25 shows a balun's diagram, where Z_0 is the characteristic impedance of the sensor's coaxial cable; $V_{1\text{-}2}$ is the balanced voltage, which is the addition of both output voltages V_1 and V_2; V_3 is the unbalanced output of the balun; and Z_3 is the output impedance seen by the balun.

To match the sensor's outputs, the reflected impedance must be twice Z_0; in this case, 100 Ω for a 50 Ω coaxial line. This reflected impedance results from the secondary impedance and the number of turns. A 1:1 balun (CoilCraft, WBC1-1TL) was connected to an amplifier (Op-Amp AD8000) with 100 Ω input and 50 Ω output.

Any transformer is not perfectly coupled, leaving a leakage inductance in series with the load. The sensor sees this inductance as an unmatched load, resulting in resonances in the frequency domain. The resonance can be shifted to higher frequencies by reducing the sensors' transmission line length before the balun.

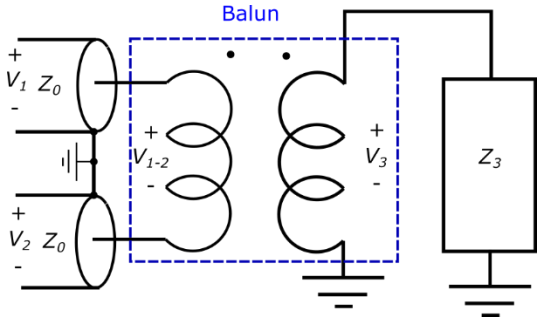

Figure 3.25 Balun transformer electric diagram, [28].

Balanced shielded loop measurements

The main intention of the BSL is to reduce the CMC coming from the coupled electric field. It is hard to measure the CMC in normal operating conditions since the differential signal eclipses it. However, only the CMCs are measured if the sensor is rotated 90°. Figure 3.26 shows the frequency response for the UBSL and BSL in normal operation and rotated 90°, resulting in the following observations:

- The UBSL shows a higher magnitude in the low-frequency range during normal operation because of the higher coupling inductance.
- When the sensors are rotated 90°, the magnitude of the UBSL is higher than in the BSL. The UBSL CMC is almost 10 % of the differential signal, whereas the signal is about 1 % in the BSL case.
- The BSL-measured noise is attributed to the gap not being perfectly centred. Even in perfectly designed sensors, other noises are coupled, [76].

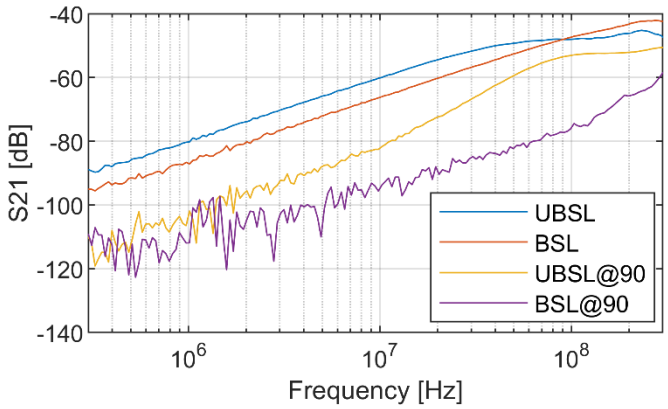

Figure 3.26 Frequency response for the UBSL and BSL in normal operation and rotated 90°, [77].

Figure 3.27 shows the Bode plot of the eight-shaped BSL compared to the single-lobe BSL. The eight-shaped sensor has double coupling and double self-inductance compared to the BSL, giving a frequency response similar to the UBSL. The eight-shaped loop performs with the CMC rejection of a BSL but with the gain of the UBSL. Figure 3.27 also shows the frequency response when using the balun with different transmission line lengths. The shortest TL was obtained with the BSL directly connected to the balun, giving a length of 12 cm. The BSL lobe

connected to the balun through a 12 cm feeder cable provides a total length of 24 cm. At last, the longest TL (36 cm) was obtained with the 8-shaped BSL connected to the feeder cable. The BSL with a 24 cm TL length gives a resonance of around 215 MHz, but when the distance is decreased to 12 cm, the resonance shifts to 300 MHz. The eight-shaped has the longest TL length, moving the resonance to 150 MHz. For better PD charge estimation, the resonances must be avoided.

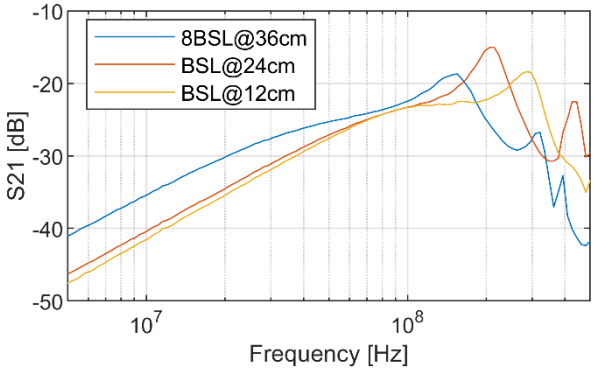

Figure 3.27 Frequency response for a balun using different TL lengths, [77].

3.3. Electric Sensor

UHF sensors are capacitive couplers, also known as electric sensors and are used for ultra-high frequency measurements. At this frequency, the sensors are electrically large compared to the wavelength, complicating the derivation of a mathematical model. However, at lower frequencies, the sensor can be modelled as lumped elements [66].

Electric sensor mathematical model

Figure 3.28 shows the electric circuit of the electric coupler. The coupling capacitance between the sensor and the GIS' inner conductor (C_1) is in parallel with the sensor's load (R) and the capacitance between the sensor and the GIS enclosure (C_2). The parasitic inductance (L) becomes relevant when the feeder conductor is thin. Equations (3.23) and (3.24) show the electric circuit's equations in the time domain. By solving them in the Laplace domain, the TF (3.25) is obtained, where $\boldsymbol{V_o}$ is the measured voltage, and $\boldsymbol{V_{pd}}$ is the propagated PD voltage. According to [66] $C_1 << C_2$, so the previous equation can be simplified as (3.26).

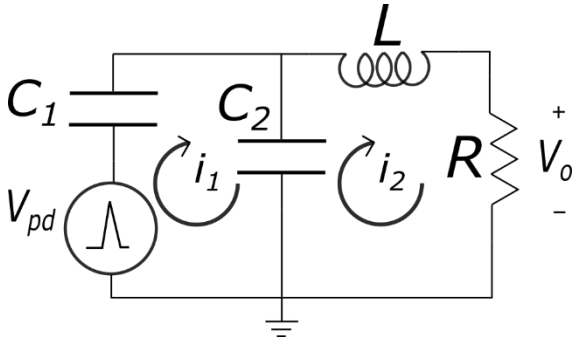

Figure 3.28 Electric circuit of an electric sensor in the VHF range, [32].

$$v_{pd}(t) = \frac{1}{C_1}\int_0^{\infty} i_1(t)dt + \frac{1}{C_2}\int_0^{\infty} i_1(t)dt - \frac{1}{C_2}\int_0^{\infty} i_2(t)dt \tag{3.23}$$

$$\frac{1}{C_2}\int_0^{\infty} i_1(t)dt = \frac{1}{C_2}\int_0^{\infty} i_2(t)dt + L\frac{di_2(t)}{dt} + Ri_2(t) \tag{3.24}$$

$$\frac{V_o}{V_{pd}} = \frac{sRC_1}{s^2LC_2 + s(RC_2 + LC_1 + RC_1) + 1} \tag{3.25}$$

$$\frac{V_o}{V_{pd}} \approx \frac{sRC_1}{s^2LC_2 + sRC_2 + 1} \tag{3.26}$$

Equation (3.26) associates the propagated PD voltage with the measured voltage. However, the PD current (I_{pd}) is required to determine the PD charge. Since the GIS behaves as a transmission line, $\boldsymbol{I_{pd}}$ can be obtained with Ohm's law ($\boldsymbol{I_{pd}} = \boldsymbol{V_{pd}}/Z_0$). Here, Z_0 is the local characteristic impedance in the GIS section where the sensor is placed. Hence, the output voltage relates to the propagated PD current, as shown in (3.27). The electric (3.27) and magnetic sensor's (3.4) models result in derivative and second-order TFs and can be generalized with (3.28), where k is the calibration constant, and ω_1 and ω_2 are the first and second-order poles.

$$\frac{V_o}{V_{pd}/Z_0} = \frac{V_o}{I_{pd}} \approx \frac{sRC_1Z_0}{s^2LC_2 + sRC_2 + 1} \tag{3.27}$$

$$H(s) = \frac{sk}{s^2/\omega_2{}^2 + s/\omega_1 + 1} \tag{3.28}$$

The testbench and the HV-lab GIS mounting holes have different dimensions, giving different parameters in (3.27) for each electric coupler. These parameters are calculated in the following way, obtaining the values in Table 3.3 for the sensors in Figure 3.29.

- $\boldsymbol{R}$ is the sensor load, normally terminated at 50 Ω.
- $\boldsymbol{Z_0}$ is calculated with the GIS geometry at the position of the sensor using (2.9).
- $\boldsymbol{C_1}$ is obtained with the same procedure of the magnetic sensor to obtain M, using (3.19).
- $\boldsymbol{C_2}$ can be obtained in the testbench by measuring the frequency response. However, this is not possible in a full-scale GIS, so C_2 was obtained with FEM simulation using the methodology in [23]. The FEM and measurement results in the testbench give similar results.
- $\boldsymbol{L}$ is neglectable for the feeder's thickness and frequency range.

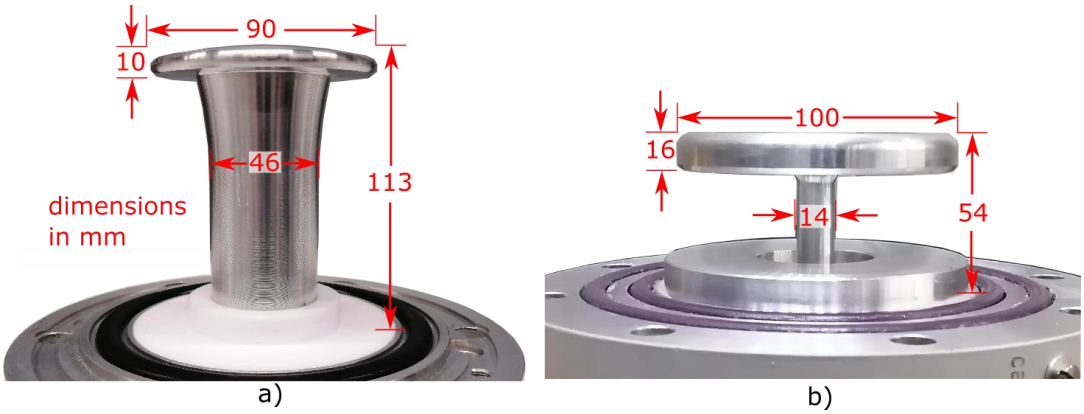

Figure 3.29 Electric couplers with dimensions for the a) testbench and b) full-scale GIS, [30].

Table 3.3 Electric parameters from sensors in Figure 3.29.

Parameter	Testbench	Full-scale GIS
Mutual capacitance (C_1)	0.49 pF	0.30 pF
Load (R)	50 Ω	50 Ω
Local characteristic impedance (Z_0)	50 Ω	70 Ω
Enclosure capacitance (C_2)	10 pF	17 pF

Electric sensor measurements

Using the parameters in Table 3.3, Figure 3.30 shows the TFs comparison between the testbench measurements and the model (3.27), approximating each other in the VHF range. Above that frequency, the electric sensor's dimensions become important, behaving as a cavity resonator and measuring higher propagation modes. The electric coupler shows higher gain than the magnetic sensor due to its higher calibration constant and first pole value.

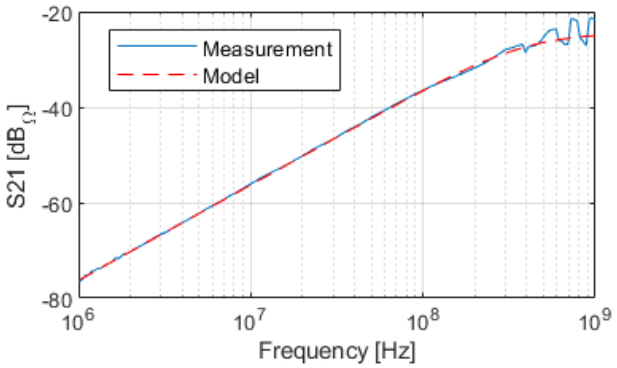

Figure 3.30 Electric sensor's transfer function measurements and model.

3.4. Chapter Conclusions

This paper introduces two very-high-frequency sensors, providing an electric model for both magnetic and electric sensors within the VHF range. The unbalanced loops experience interference from coupled common-mode currents that is mitigated by incorporating common-mode ferrites and a balanced loop configuration. The 8-shaped balanced shielded

loop demonstrated the highest gain and lower common-mode current of all the magnetic sensors shown in this thesis. The balun serves as a viable option for enhancing sensor gain, albeit at the cost of reduced bandwidth. In the case of the electric sensor, two commercial electric couplers were examined, demonstrating superior gain compared to magnetic sensors. The mathematical model aids in comprehending the impact of each electric element on the design and facilitates an investigation into the relationship between the sensor and the charge estimation method.

4

"One accurate measurement is worth a thousand expert opinions".

- Grace Hopper

4. Electric and Magnetic Sensors' Combination*

The previous chapter presented two derivative sensors based on the detection of the electric and magnetic fields produced by a PD. Their time and frequency domains were measured in a matched testbench, resulting in signals without reflections. However, a full-scale GIS has multiple discontinuities, creating overlapped reflections that distort the measured pulses. This chapter proposes a method that integrates both sensors into the same GIS transversal position, providing additional advantages such as the identification of forward and backward propagation, reduction of overlapped pulses, and determination of the PD pulse power flow. The combination of both sensors is known throughout the thesis as "synergy".

The chapter begins by explaining the measured electromagnetic waves using electric and magnetic sensors. Subsequently, the combination of both sensors is introduced through two methods that are explored in sections 4.2 and 4.3. The first method integrates the sensors by digitally processing the electric and magnetic signals, designated as "software combination". The second method involves a "hardware combination" where the electric and magnetic couplers are physically merged, resembling a directional coupler. Thereafter, the

* This chapter is based on the following publications:

- C. Mier, A. Rodrigo Mor, P. Vaessen, and A. Lathouwers, "Magnetic and electric antennas synergy for partial discharge measurements in gas-insulated substations: Power flow and reflection suppression," International Journal of Electric Power Energy Systems, vol. 144, no. January 2023, pp. 1–9, 2023, doi: 10.1016/j.ijepes.2022.108530.
- C. Mier, A. Rodrigo Mor, and P. Vaessen, "A directional coupler for partial discharge measurements in gas-insulated substations," Measurement: Journal of the International Measurement Confederation, vol. 225, 2024, doi: 10.1016/j.measurement.2023.113996.

software and hardware combinations are tested in a full-scale GIS. Finally, a chapter conclusion is given.

4.1. Pulse Propagation in a GIS

4.1.1. Power flow

When a PD occurs, an electromagnetic wave propagates in all directions. Given that a single-phase GIS behaves as a coaxial waveguide, the PD propagates in two directions in the waveguide axis. The EM propagation direction is independent of the PD polarity and can be characterized using the Poynting vector. The Poynting vector represents the Power Flow (PF) per unit area. If it is integrated over the coaxial cross-section, it results in the voltage and current product (4.1), where $\vec{e}$ is the electric field, $\vec{h}$ is the magnetic field, $\vec{A}$ is the cross-section, v is the voltage, and i is the current. An example is illustrated in Figure 4.1 using cylindrical coordinates (r,φ,z). The PD current and voltage can be measured with a magnetic and an electric sensor, and thus, the power flow can be obtained in a GIS.

$$PF = \int_A \vec{e} \times \vec{h} \cdot d\vec{A} = vi \tag{4.1}$$

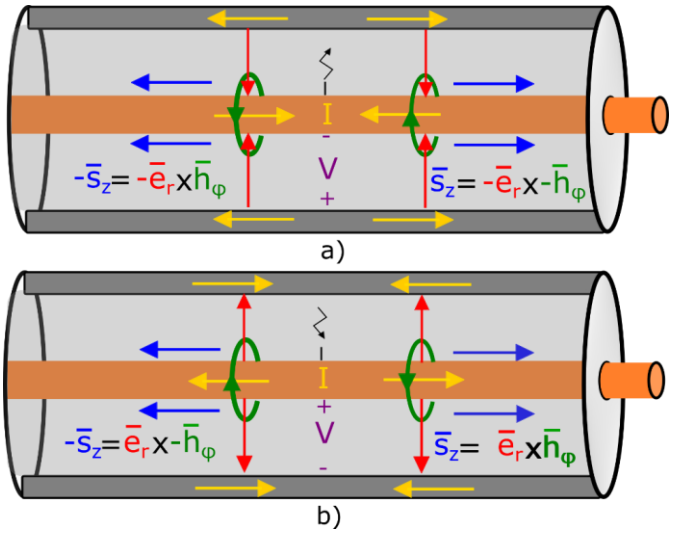

Figure 4.1 Poynting vector ($\vec{S}$) for a) positive and b) negative discharge, [30].

When a transmission line is not matched, the measured signal is formed by the incident pulse followed by forward and backward components. Equations (4.2) and (4.3) represent the voltages and currents when the TL has discontinuities, where v^+ and v^- are the forward and backward voltage pulses, respectively; i^+ and i^- are the forward and backward current pulses, respectively; Z_1 and Z_2 are the impedances before and after the discontinuity; z is the distance from the discontinuity to the observation point (sensor location), c is the speed of light in the medium, $2z/c$ the time delay between the incident and the reflected pulse; and Γ is the reflection coefficient.

$$v^-(z,t) = \Gamma v^+\left(t + \frac{2z}{c}\right) \; where \; \Gamma = \frac{Z_2 - Z_1}{Z_2 + Z_1} \tag{4.2}$$

$$i^+(z,t) = \frac{v^+(z,t)}{Z_0} \; and \; i^-(z,t) = -\frac{v^-(z,t)}{Z_0} \tag{4.3}$$

The signal's instantaneous power cannot be recovered with GIS PD sensors due to their narrow bandwidth; however, the signal's power flow can be represented. Forward and backward pulses can be distinguished using the power flow equation (4.4), where the first term is all forward pulses, and the second term is all backward pulses, having opposite polarity between them. A pulse overlapping happens when the delay between backward and forward signals is shorter than the pulse duration. This overlapping can be avoided by eliminating the reflections using the magnetic and electric sensors, as shown in the next sections. Distinguishing the reflected pulses improves the PD charge estimation, PD waveshape, and defect location.

$$PF(z,t) = v^-(z,t) * i^-(z,t) = \underbrace{\frac{{v^+}^2(z,t)}{Z_0}}_{forward} - \underbrace{\frac{\Gamma^2 {v^+}^2(t + 2z/c)}{Z_0}}_{backward} \tag{4.4}$$

4.1.2. Elimination of Pulse Reflections

Equation (4.3) demonstrated that the reflected current has an opposite polarity than the reflected voltage. This fact can be used to add the forward components and reduce the backward ones. Equations (4.5) and (4.6) show the electric and magnetic sensors' measurements with the forward and backward components. If the electric output, for instance, is scaled (α) to match the magnetic output, according to (4.3), the backward component changes polarity and results in (4.7). Therefore, adding the magnetic and the scaled electric output results in a doubled forward component and an eliminated backward component, as demonstrated in (4.8). Equation (4.8) is an ideal situation where the scale factor perfectly matches both sensors. The following section shows two proposed scale functions to reduce reflections.

$$v_e(t) = {v^+}_e(t) + {v^-}_e(t) \tag{4.5}$$

$$v_m(t) = {v^+}_m(t) - {v^-}_m(t) \tag{4.6}$$

$$\alpha v_e(t) = {v^+}_m(t) + {v^-}_m(t) \tag{4.7}$$

$$v_m(t) + \alpha v_e(t) = 2{v^+}_m(t) \tag{4.8}$$

4.2. Software Combination

To effectively mitigate backward reflections, it is crucial to align the responses of the magnetic end electric sensors. As detailed in section 3.3, both sensors share the same TF,

wherein determining the second-order pole presents challenges. However, the transfer function can be simplified by introducing a low-pass filter. The LPF not only reduces the TFs, but it is also necessary to reject high-frequency noise. By filtering the sensors with a low-pass frequency (ω_f) significantly lower than the sensors' second pole, (3.28) can be expressed as (4.9). Solving (4.9) for the output voltage and acknowledging that the short duration of the PD pulse resembles a Dirac delta pulse in the Laplace domain, characterized by a magnitude equal to the charge Q and a time delay t_d, obtaining (4.10). To simplify the evaluation, a 1st-order filter and a Dirac delta pulse with $t_d=0$ were chosen, yielding the time-domain function in (4.11). The time-domain (4.11) and frequency-domain (4.9) functions serve as the foundation of the scale functions.

$$\frac{\boldsymbol{V}_o(s)}{\boldsymbol{I}_{pd}(s)} = \underbrace{\frac{sk}{s/\omega_1 + 1}}_{sensor} \underbrace{\boldsymbol{H}(s)}_{filter} \tag{4.9}$$

$$\boldsymbol{V}_o(s) = Qe^{-st_d}\frac{sk}{\frac{s}{\omega_1}+1}\boldsymbol{H}(s) \tag{4.10}$$

$$v_o(t) = Q\frac{k{\omega_1}^2\omega_f}{\omega_0-\omega_f}e^{-\omega_1 t} - Q\frac{k{\omega_f}^2\omega_1}{\omega_0-\omega_f}e^{-\omega_f t} \tag{4.11}$$

4.2.1. Peaks Scale Factor

One proposal to match the electric and magnetic sensors in (4.8) is to scale α with their measured peaks. From (4.11), we can see that the peak occurs when $t=0$, resulting in (4.12). Therefore, the electric and magnetic peak's ratio is the factor C_{pk} equal to (4.13). Now, if the backward component of the electric sensor (v_e^-) is subtracted from the scaled magnetic sensor's backward component ($v_m^- C_{pk}$), the resultant backward pulse (v_{em}^-) is obtained in (4.14). Note in (4.14) that the reflections are eliminated if the filters and sensors' cut-off frequencies are equal. The filters' corner frequencies can be selected as wished, but ω_1 depends on the self-inductance and parasitic capacitance of the magnetic and electric sensors, respectively. This inductance and capacitance can be manipulated by the physical design (as in section 4.3), with the risk of altering other electric parameters.

$$v_o(0) = V_{peak} = Qk\omega_1\omega_f \tag{4.12}$$

$$C_{pk} = \frac{V_{peak-e}}{V_{peak-m}} = \frac{Qk_e\omega_{1e}\omega_{fe}}{Qk_m\omega_{1m}\omega_{fm}} \tag{4.13}$$

$$C_{pk}v^-_m(t) - v^-_e(t) = v^-_{em}(t) = Q\left(\begin{array}{l}\frac{k_e\omega_{1e}\omega_{1m}\omega_{fe}}{\omega_{1m}-\omega_{fm}}e^{-\omega_{1m}t} - \frac{k_e{\omega_{1e}}^2\omega_{fe}}{\omega_{1e}-\omega_{fe}}e^{-\omega_{1e}t} - \\ -\frac{k_e\omega_{1e}\omega_{fe}\omega_{fm}}{\omega_{1m}-\omega_{fm}}e^{-\omega_{fm}t} - \frac{k_e{\omega_{fe}}^2\omega_{0e}}{\omega_{1e}-\omega_{fe}}e^{-\omega_{fe}t}\end{array}\right) \tag{4.14}$$

4.2.2. Transformation Filter Scale Function

An alternative method is to process the signal in a way that both sensors have the same transfer function. To mimic one coupler's output signal into the other, a convolution is done using the sensor's output to be scaled and a Transformation Filter (TRF). Equation (4.15) shows the transformation of the magnetic output ($v_{m\to e}$), where $H_{e/m}$ represents the TRF. Superimposing the electric and scaled magnetic outputs results in (4.16)—the same procedure can be done to mimic the magnetic sensor's output ($v_{e\to m}$)—. The TRF is the sensor's TF to be emulated over the sensor's transfer function to be scaled (4.17) and can be represented with (4.18) using electric parameters, where C_1 and C_2 are the coupling and parasitic capacitances of the electric sensor, M and L_s are the coupling inductance and self-inductance of the magnetic sensor, and R is the load for both couplers.

$$v_{m\to e}(t) = \frac{1}{2\pi j}\int_0^t e^{st}\big(\boldsymbol{V}_m(s) * \boldsymbol{H}_{e/m}(s)\big)ds \tag{4.15}$$

$$v_{em}(t) = v_e(t) + v_{m\to e}(t) \tag{4.16}$$

$$H_{e/m}(s) = \frac{V_e(s)}{V_m(s)} = \frac{k_e\left(\frac{s}{\omega_{1m}}+1\right)}{k_m\left(\frac{s}{\omega_{1e}}+1\right)} \tag{4.17}$$

$$H_{e/m}(s) = \frac{C_1 R Z_0\left(\frac{sL_s}{R}+1\right)}{M(sC_2R+1)} \tag{4.18}$$

A minimum time lag between the couplers is required to use the software combination effectively. In the peaks and TRF approaches, the electric and magnetic sensors must be located at the same longitudinal position at the GIS, so that the propagated pulse is induced in both sensors simultaneously. Section 3.2.1 showed that a shielded magnetic loop introduces a time delay to the sensed signal, demanding a correction to ensure no time delay between couplers.

4.2.3. Testbench Experimentation

The power flow and reflection elimination estimations require the PD current and voltage measurements, which can be done with a magnetic and an electric sensor. The sensors used were the 8-shaped shielded balance magnetic from Figure 3.24 and the electric coupler from Figure 3.29 a). The experiments were done in the TEM testbench with both mounting holes placed in the same transversal position, as illustrated in Figure 3.1.

To evaluate the pulse power flow, a pulse was injected in both directions, with both polarities and with the opposite cone short-circuited and open-circuited.

The reflection elimination and charge estimation were evaluated for two different cases: 1) with no pulse overlap, having an open circuit 596 cm away from the sensors to create a reflection of the same polarity (extending the testbench with a coaxial cable) and 2) with

pulse overlap, having a short circuit 76 cm apart from the sensors, using a 10 ns width pulse to create a reflection with reversed polarity. In both cases, pulses were injected from both ends for different propagation directions.

Power flow results

Figure 4.2 presents the measured pulses for different input pulses and discontinuities: a) is a positive polarity pulse propagating from the left-hand side in an open-circuited testbench, b) is a positive polarity pulse propagating from the right-hand side in a short-circuited testbench, c) is the same as a) but with a negative polarity pulse, d) is the same as b) but with a negative polarity pulse. The magnetic sensor's output is scaled with the C_{pk} factor for better visualization. Using the measured pulses in Figure 4.2, Figure 4.3 shows the power flow for each combination: a) is the PF for Figure 4.2 a) and c), and b) is for Figure 4.2 b) and d). The individual electric or magnetic sensors' outputs in Figure 4.2 do not provide the propagation direction: the incident polarity, the reflection coefficient, and the pulse direction affect the pulse polarity. On the contrary, the power flow correctly identifies the direction of the propagation independently of previous variables, where the positive power flow is pulses coming from the right, and negative PF is pulses coming from the left. The power flow provides a better tool for PD defects' localization, reducing the number of required sensors.

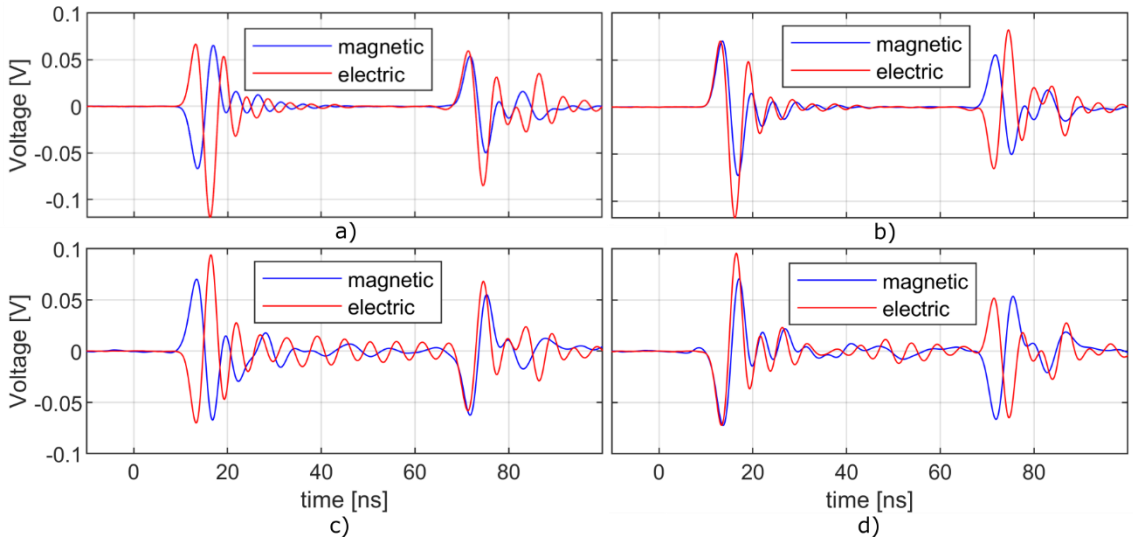

Figure 4.2. Electric and scaled magnetic sensors' measurements where: a) left propagated positive polarity pulse in an open-circuited testbench, b) right propagated positive polarity pulse in a short-circuited testbench, c) same as a) but with a negative polarity pulse, d) is the same as b) but with a negative polarity pulse [78].

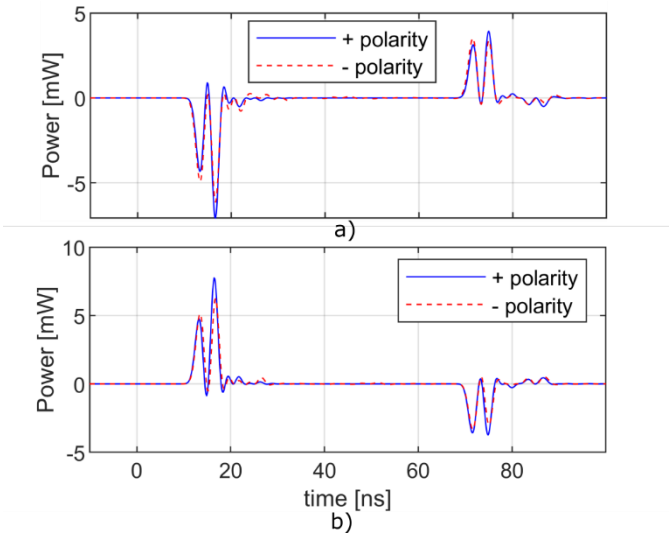

Figure 4.3 a) Power flow for both polarity pulses in an open circuit testbench, propagated from the left, and b) power flow for both polarity pulses in a short circuit testbench, propagated from the right [78].

Reflection elimination and charge estimation results

This section presents the reflection elimination using (4.8) with the peaks scale function (4.13) and the transformation filter methods (4.18).

Figure 4.4 shows the measurements when a short circuit is placed 76 cm away from the sensors, creating overlapped pulses: a) magnetic and electric measured pulses with discontinuity compared with matched (no reflections) pulses, b) discerned incident and reflected pulses using the peak method and compared with a matched pulse, and c) is the same as b) but using the TRF method applied to the electric sensor. Figure 4.4 a) shows that the measured waveforms are distorted compared to the matched case. Since the discontinuity is a short-circuit, the magnetic sensor has a constructive superposition, while the electric coupler has a destructive one. In b) and c), the forward pulse approximates the matched case, having a better result when applying the TRF method than the peak method because the superposition affects the peak values. The reflected pulse is well segregated, coinciding with the space delay (5.3[ns]*30[cm/ns]) with the 2x76[cm] discontinuity distance. Please note that in b), the matched electric measurement is used for comparison since the peak's constant is applied to the magnetic sensor, and in c), the matched magnetic output is used because the TRF method is applied to the electric sensor.

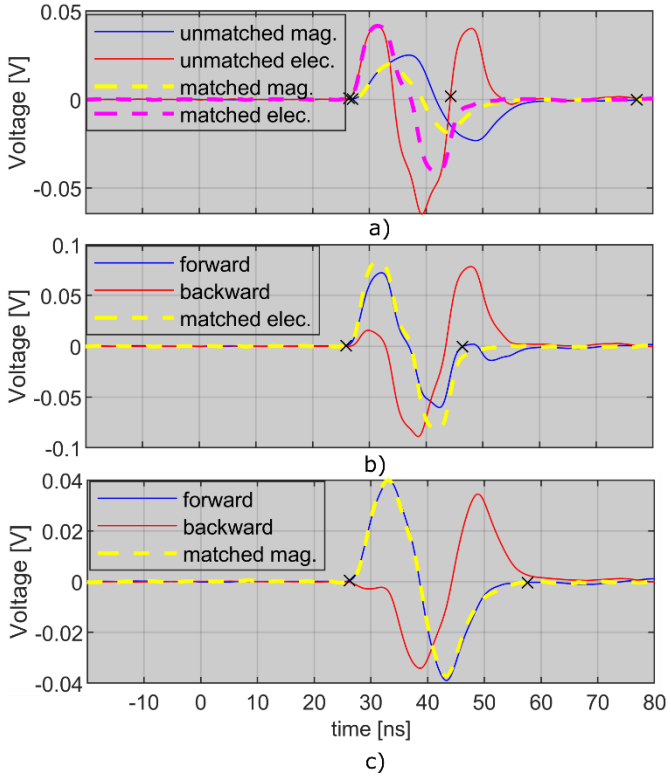

Figure 4.4 Short-circuited testbench at 76 mm: a) unmatched and matched magnetic and electric measured pulses, b) incident and reflected pulses using the peaks method and matched electric pulse, and c) incident and reflected pulses using the TRF method and matched magnetic pulse [78]**. The black crosses indicate the zero crossings used for the charge calculation.**

Figure 4.5 shows the non-overlapping situation (Figure 4.5). The transformation filter also shows a better reflection elimination because the sensor cut-off frequency difference affects the peaks method. Using the voltage double integration method presented in section 2.1.3, the charges were estimated to evaluate the effectiveness of the reflection elimination. A full explanation of the calibration method is provided in the next chapter. Table 4.1 shows the calculated charge errors without and with combining the sensors, with the discontinuity at 596 cm (no pulse overlap) and at 76 cm (pulse overlap) away from the sensors. The charge estimation is improved using the combination method when the pulse is overlapped, from above 60% to below 7% error (in the TRF case). Also, better PD identification can be obtained by constructing the pulse waveshape [40].

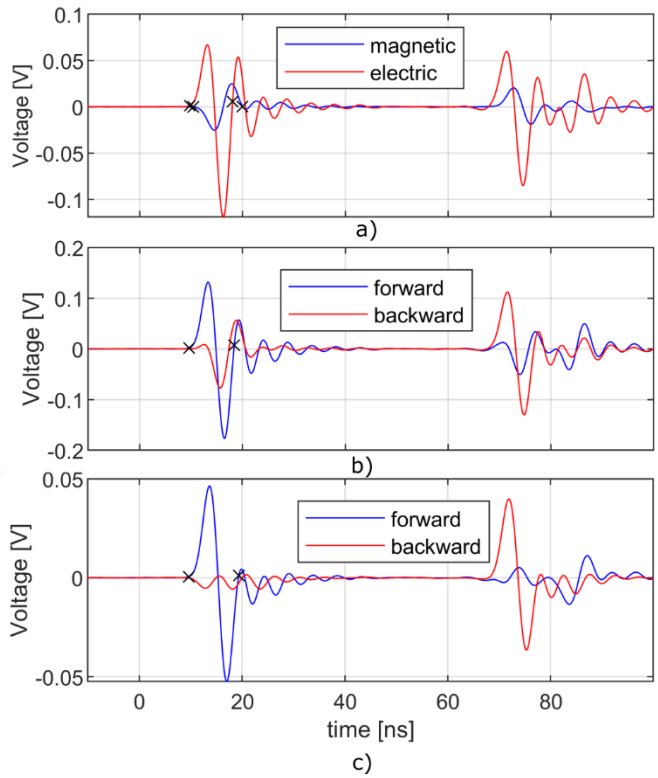

Figure 4.5 Testbench open-circuited at 596 mm: a) magnetic and electric sensors measured pulses, b) incident and reflected pulses using the peaks method, and c) incident and reflected pulses using the TRF method, [78].

Table 4.1 Charge estimation error without and with synergy with a discontinuity at 596 and 76 cm, [78].

	Error @ 76 cm (pulse overlap)	Error @ 596 cm (no pulse overlap)
Magnetic	89 %	-15 %
Electric	-60 %	-15 %
Peaks	-18 %	-23 %
TRF Electric	4.2 %	-0.2 %
TRF Magnetic	6.2 %	-29 %

4.3. Hardware Combination

In the software synergy, the sensors were installed in the same transversal position within the GIS but in adjacent mounting holes. Using the signals measured by both sensors, the combination of electric and magnetic measurements eliminates the backward component, enhancing the PD charge estimation when PD pulses overlap due to pulse reflections within the GIS. However, this method requires both sensors' signals to arrive simultaneously, representing an additional challenge to the software method.

The "hardware combination" method physically combines the electric and magnetic couplers in a manner similar to a directional coupler. The combination of both couplers, identified in this research as Directional GIS Coupler (DGISC), offers advantages over the previous method, including power-frequency voltage shielding, single mounting hole installation, and incident and reflected pulses segregation without the need for additional

digital signal processing. However, the physical combination of both sensors requires additional considerations regarding the sensor design and the calibration procedure.

4.3.1. The directional Coupler

Directional couplers are widely used for radio frequency applications. Their primary function is to measure incident and reflected waves, and they are used to check the connection integrity of antennas and vector network analysers [79]. Figure 4.6 shows the fundamentals of the directional coupler. In a), a wave travels in the main circuit (top line) from left to right, with its current (blue arrow) in the same direction. This wave produces an electric field (red arrows) and a magnetic field (green cross) in the secondary circuit (bottom circuit), where the electric field induces a common-mode current (light-red arrows) and the magnetic field a counterclockwise current (light-blue arrows). These induced electric and magnetic currents are added in the left resistor and subtracted in the right one. Now, if the secondary circuit is designed to couple the same amount of inductive and capacitive current, the induced voltage is doubled and nulled in the left and right loads, respectively. In b), the wave travels from right to left, inducing an electric field in the same direction as in the previous case but with an opposite polarity magnetic field. This results in a doubled and a nulled voltage in the right and left loads, respectively. Therefore, this configuration measures the forward component in one load and the backward component in the other. The directional coupler's ability to separate the forward and backward wave propagation is quantified by the directivity.

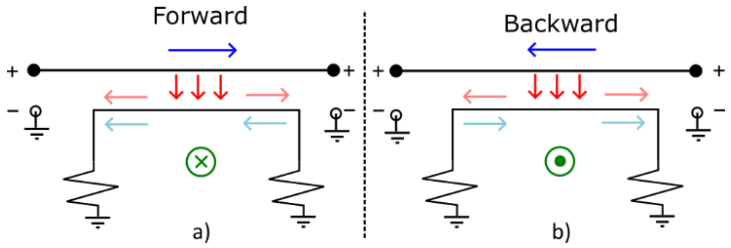

Figure 4.6 a) Forward and b) backward components induced in a directional coupler, [31].

The GIS PD electric and magnetic sensors can be configured similarly to the directional coupler. In this case, the GIS acts as the primary circuit, and the sensors function as the couplers of the secondary circuit. A notable distinction between a traditional directional coupler and the DGISC lies in the high voltage associated with the latter. This imposes limitations on the sensor's positioning and geometry, requiring it to be adapted to the GIS mounting hole and to cope with the electric field at the power frequency, typically 50/60 Hz or DC.

The sensors depicted in Figure 3.1 can be interconnected to simultaneously couple the PD electric and magnetic fields, as illustrated in Figure 4.7 a). The integration of both sensors into a single circuit leads to the electric model depicted in Figure 4.7 b). In this representation, the lower circuit corresponds to the GIS, while the upper one corresponds to the sensor. The DGISC model (4.19) results from the superposition of the electric (3.18) and magnetic (3.26)

sensors' transfer functions. The addition or subtraction between the magnetic and electric components depends upon the propagation direction, as with the directional coupler.

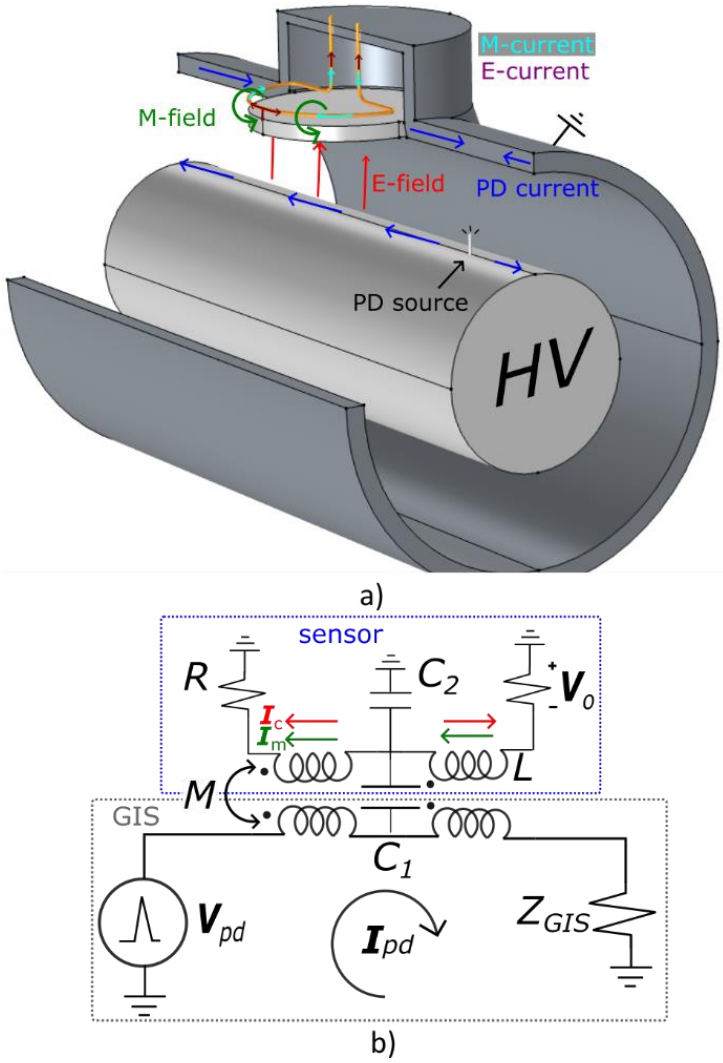

Figure 4.7. DGISC a) induced forward and backward components illustration and b) electric circuit, [31].

$$\frac{\boldsymbol{V}_{oe}+\boldsymbol{V}_{om}}{\boldsymbol{I}_{pd}}=\frac{\boldsymbol{V}_{o}}{\boldsymbol{I}_{pd}}\approx\underbrace{\frac{sk_e}{s^2/{\omega_{2e}}^2+s/\omega_{1e}+1}}_{electric-component}\pm\underbrace{\frac{sk_m}{s^2/{\omega_{2m}}^2+s/\omega_{1m}+1}}_{magnetic-component} \tag{4.19}$$

The DGISC measures a PD's forward and backward components, providing advantages over using a single magnetic or electric sensor. In addition to the advantages mentioned in the previous section, in the DGISC, the electric coupler shields the magnetic coupler against the power-frequency voltage. However, combining both sensors in the same mounting hole leads to undesirable interactions between them. The subsequent section outlines these interactions between the couplers and details the solutions adopted to minimise them.

4.3.2. Electric and Magnetic Sensors Interaction

This section explores the interaction between both couplers within the same mounting hole without being connected to form a directional coupler. On one hand, the magnetic field

coupled to the magnetic loop is reduced by incorporating the electric shield. On the other hand, the attachment of the electric coupler to the magnetic loop introduces an undesired resonance. To investigate these interactions, frequency-domain FEM simulations were conducted at 100 MHz, employing the electromagnetic wave equation (4.20). Here, μ_r represents the relative permeability, μ_0 and ε_0 denote the permeability and permittivity of free space, ω is the angular frequency, and $\hat{\varepsilon}$ represents the lossy permittivity (4.21). The first term in (4.21) is associated with the polarizability of the dielectric (ε_r), while the second is related to the conduction losses, where σ is the DC conductivity. Moreover, frequency-domain measurements were performed on the TEM testbench.

$$\nabla \times \frac{1}{\mu_r}(\nabla \times \mathbf{E}) - \omega^2 \varepsilon_0 \mu_0 \hat{\varepsilon} \boldsymbol{E} = 0 \tag{4.20}$$

$$\hat{\varepsilon} = \varepsilon_r - \frac{j\sigma}{\omega \varepsilon_0}^{2} \tag{4.21}$$

Reference [23] demonstrated that the PD current generates a magnetic field in the xy-plane of the GIS mounting hole, illustrated in the coloured plane in Figure 4.8 a). The time-varying magnetic field induces a voltage in the magnetic sensor, and any other conductor within the same xy-plane generates a counter-electromotive force in the magnetic coupler, reducing its sensitivity. Based on the TEM testbench, a FEM simulation was conducted to evaluate the capacitive and magnetic coupling of the electric and magnetic sensors, respectively. The electric sensor is mounted between the high-voltage conductor and the magnetic loop, so the magnetic sensor does not interfere with the electric coupling. The magnetic loop was omitted to reduce the simulation time, but by knowing the magnetic flux in the magnetic sensor's plane ($\boldsymbol{\Phi}_z$) and the charge (Q) at the electric sensor's bottom face, their corresponding coupling inductance and capacitance can be approximated with (4.22).

$$M = \frac{d\boldsymbol{\Phi}_z}{d\boldsymbol{I}_{pd}} \; and \; C_1 = \frac{Q}{\boldsymbol{I}_{pd} Z_{GIS}} \tag{4.22}$$

Figure 4.8 b) shows the mutual capacitance and inductance of the sensors concerning three variables: magnetic plane position (● [mm]), electric coupler diameter (O [mm]), and electric disk lossy permittivity (✕). The magnetic plane position is measured from the GIS enclosure, aligning with the electric disk's top face (see Figure 4.8a). For reference, the sensors' maximum capacitance (C_{max}) and inductance (M_{max}) were determined individually with a 98 mm diameter aluminium (conductivity 7×10^7 S/m) disk and a magnetic plane placed at ✕=2 mm. These variables were independently simulated while keeping the remaining variables constant to the reference values, as shown in Table 4.2.

Results from varying the magnetic plane position indicate that the maximum magnetic flux no longer occurs at 2 mm due to the presence of the electric disk; instead, it shifts to 11 mm. Another approach to diminish the electric-disk's magnetic coupling is by reducing the electric disk diameter. As depicted in Figure 4.8 a), most of the magnetic field lies at the edge

due to the proximity effect. Thus, decreasing the electric disk diameter diminishes the counter-electromotive force, reducing the electric coupling (C_1) as well. The third option involves increasing the disk impedance, revealing an optimal electric and magnetic coupling with a lossy permittivity of $1x10^3$. It is crucial to control this material permittivity to maintain the effectiveness of the power-frequency shield grading.

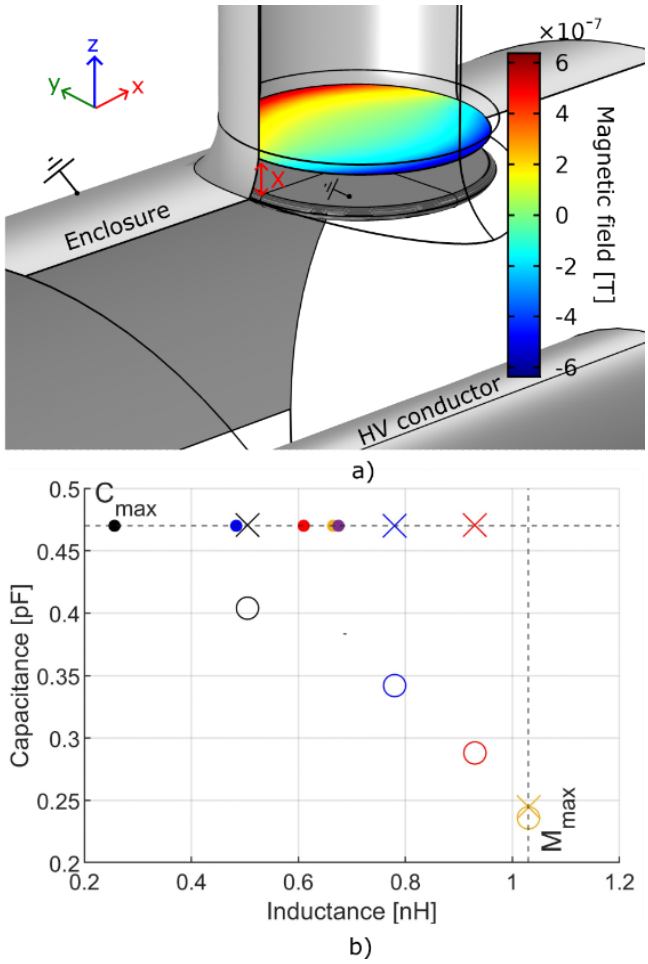

Figure 4.8. a) Finite element method simulation of the magnetic field induced in a xy-plane in the presence of an electric disk. b) Capacitance and inductance simulation as a function of the parameters shown in Table 4.2, [31].

Table 4.2 Parameters used for FEM simulation in Figure 4.8, [31].

	Magnetic plane position [mm]	Electric coupler diameter [mm]	Electric disk lossy permittivity
●	2	98	1E+10
●	5	98	1E+10
●	8	98	1E+10
●	11	98	1E+10
●	14	98	1E+10
O	2	94	1E+10
O	2	90	1E+10
O	2	86	1E+10
O	2	82	1E+10
×	2	98	1E+06
×	2	98	1E+04
×	2	98	1E+03
×	2	98	2E+00

The material properties of the electric disk must fulfil the trade-off between shielding the 50/60 Hz power-frequency electric field and blocking the high-frequency Eddy currents. A finite element simulation was conducted to determine the minimum required conductivity for an effective grading shield. The criterion involved reducing the shield's conductivity until the electric field at the magnetic loop exceeded the field when no loop was placed, resulting in a value of $4x10^{-7}$ S/m at 50 Hz. The material's lossy permittivity can be manipulated by incorporating Carbon Black into an epoxy resin mixture (CB). An Araldite® epoxy resin with 5% carbon black was cast, yielding a 100 MHz lossy permittivity of 20 and a 50 Hz conductivity of $1.7x10^{-5}$ S/m, as measured with the vector network analyser.

Various parameters must be considered to achieve maximum gain with the two sensors. Figure 4.9 shows the frequency response of the electric (a) and magnetic (b) couplers, both sharing the same mounting hole with different disk configurations. The blue line represents a 100 mm diameter aluminium disk, matching the mounting hole's diameter, providing optimal electric coupling but with increased Eddy current. The red plot represents an aluminium disk reduced to 60 mm diameter, yielding a lower electric sensor's gain but without affecting the magnetic coupler. An alternative solution, plotted in black, is a 70 mm diameter aluminium disk with a 16 mm thick CB rim (Figure 4.10). As demonstrated in Figure 4.8, decreasing the material's permittivity at the disk's edge preserves the magnetic sensor's magnetic field. Furthermore, incorporating the aluminium disk into the CB rim allows better electric contact. The described interaction between the electric and magnetic couplers arises from sharing the same mounting hole, even before interconnecting them to form a directional coupler.

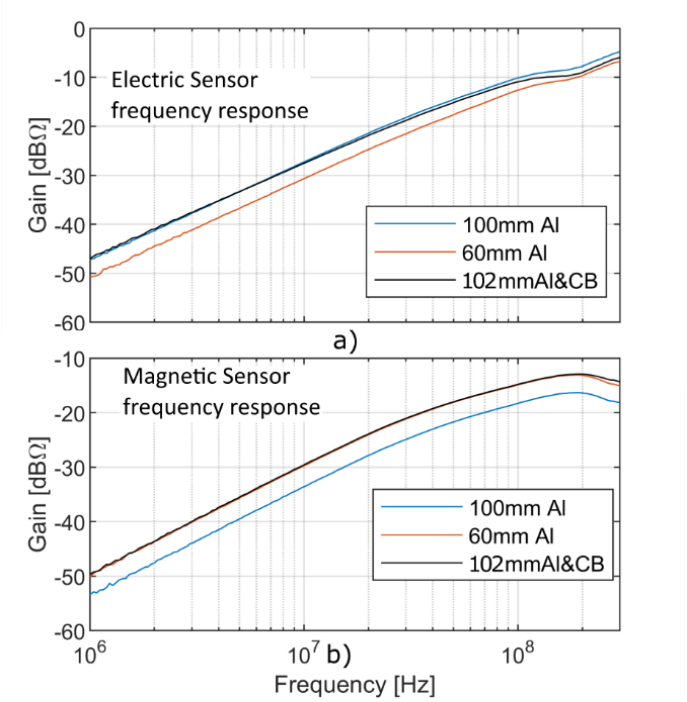

Figure 4.9. a) Electric and b) magnetic sensors' frequency response with different disk configurations [80].

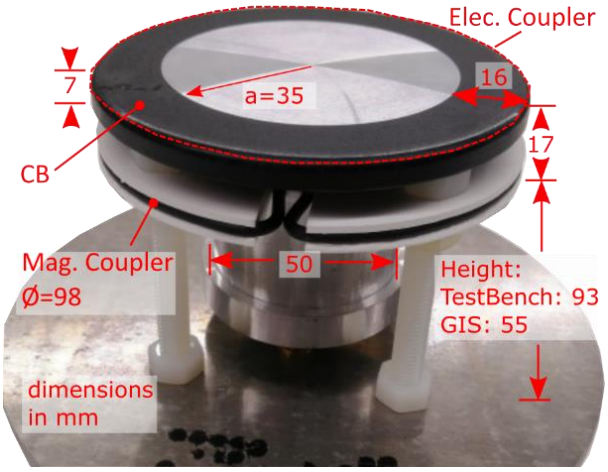

Figure 4.10. Picture and dimensions of the electric and magnetic sensors in a single mounting hole configuration, [31].

4.3.3. Directional GIS Coupler Design

The electric connection of the electric and magnetic couplers can be conceptualized as a single sensor with an electric component (electric sensor's contribution) and a magnetic component (magnetic sensor's contribution). As shown in (4.19), to enhance the directional coupler's directivity, the magnetic and electric components must be similar to segregate forward and backward pulses effectively. Consequently, the design has to be tailored to align each component's zeros and poles. These parameters depend upon the sensor geometry subjected to the GIS mounting hole dimensions.

The electric and magnetic coupling constants (k) can be matched by adjusting the electric and magnetic couplings (C_1 and M) with the parameters shown in Figure 4.8. However, for the case of ω_1, adjusting the self-inductance (L) and the ground capacitance (C_2) proves

challenging without influencing the other parameters. Figure 4.7 shows that the currents originating from the electric coupler (I_e) are common mode, while the magnetic currents (I_m) are differential mode. Introducing a ferrite choke in the feeder conductor allows the adjustment of the electric's first pole without affecting other parameters. Figure 4.11 depicts the induced impedance to a conductor coupled to the ferrite, reflected in the circuit as shown in Figure 4.12 and resulting in (4.23). Lastly, the second pole is typically above the frequency of interest, rendering it negligible and thus ignored.

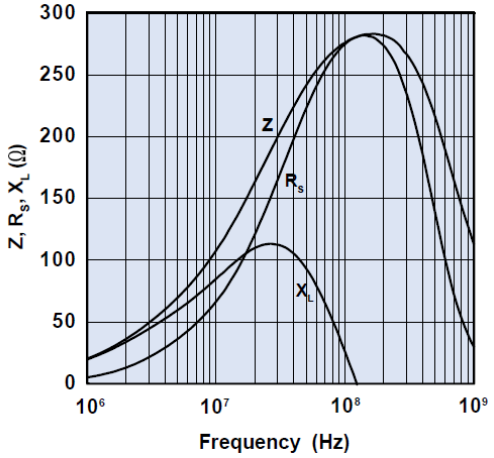

Figure 4.11. Induced impedance in a cable coupled to a Fair-Rite 0443164251.

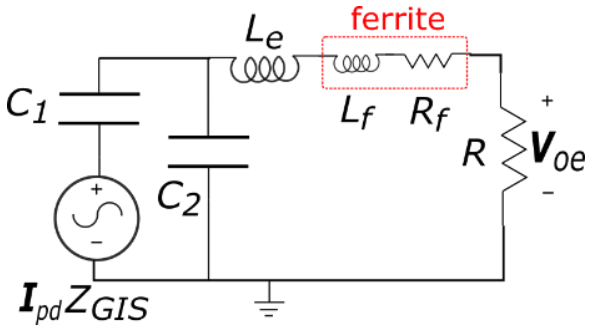

Figure 4.12. Electric-component circuit with the ferrite choke, [31].

$$\frac{\boldsymbol{V}_{oe}(s)}{\boldsymbol{I}_{pd}(s)} \approx \frac{sRC_1Z_{GIS}}{s^2(L_e + L_f(s))C_2 + sC_2(R + R_f(s)) + 1} \tag{4.23}$$

The differential mode can be satisfied with a shielded magnetic loop probe, as demonstrated in section 3.2.2. The only accessible location for connecting the electric coupler to the shielded loop is at the gap of the shield. Figure 4.13 illustrates the electric coupler connected to an unbalanced (bottom lobe) and a balanced (top lobe) loop. In the unbalanced configuration, nearly all the electric component's current (red arrows) flows through the grounded gap path. Conversely, in the balanced configuration, the electric component current encounters identical paths at the middle gap. Consequently, the self-inductance is reduced since the current flows evenly in each direction but with different polarities. The 8-shaped balanced magnetic loop facilitates the gap connection in the centre of the electric disk.

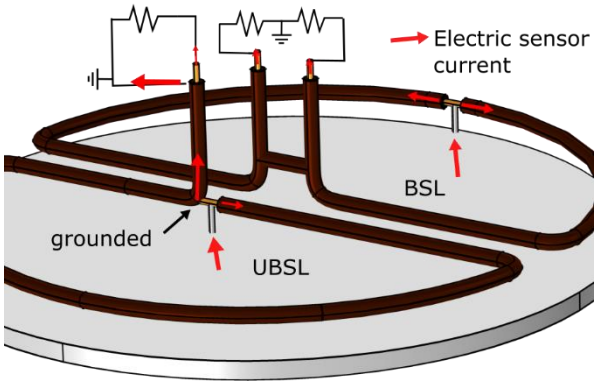

Figure 4.13. Electric coupler's current distribution (red arrows) in an UBSL (bottom lobe) and a BSL (top lobe) , [31].

To evaluate the DGISC and assess the impact of the ferrite, measurements in the testbench were taken of the sensor's backward and forward outputs using the "8-shaped" balanced loop connected to a 90 mm diameter aluminium electric disk (Figure 4.14). As previously mentioned, the forward output ($\boldsymbol{V^+}$) is the sum of both components, while the backward output ($\boldsymbol{V^-}$) is the difference between them, (4.24). Adding or subtracting these outputs allows the calculation of the electric ($\boldsymbol{E_c}$) and the magnetic ($\boldsymbol{M_c}$) voltage components, as indicated in (4.25). Figure 4.15 a) displays the outputs with and without ferrite chokes, demonstrating that the ferrites shift the cut-off frequency and reduce the resonance peak. Figure 4.15 b) illustrates both outputs with ferrite choke and the estimated electric and magnetic components using (4.25). Due to the inequality between the electric and magnetic elements, the backward output is not completely eliminated, having a 15 dB difference with the forward output.

$$\boldsymbol{V^+ = E_c + M_c} \; and \; \boldsymbol{V^- = E_c - M_c} \tag{4.24}$$

$$\boldsymbol{E_c = \frac{V^+ + V^-}{2}} \; and \; \boldsymbol{M_c = \frac{V^+ - V^-}{2}} \tag{4.25}$$

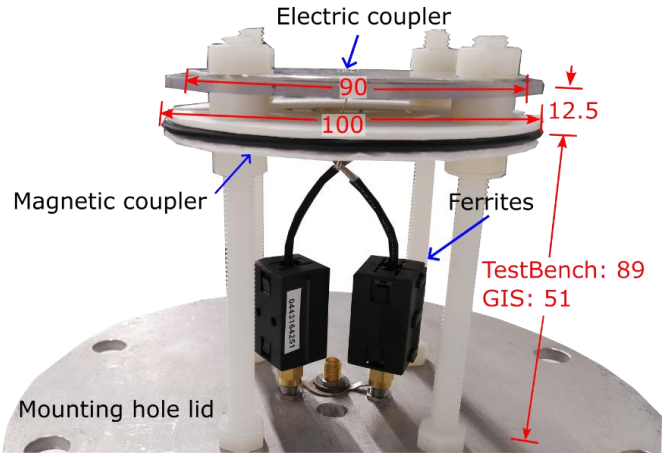

Figure 4.14. Photo and dimensions of the DGISC, [31].

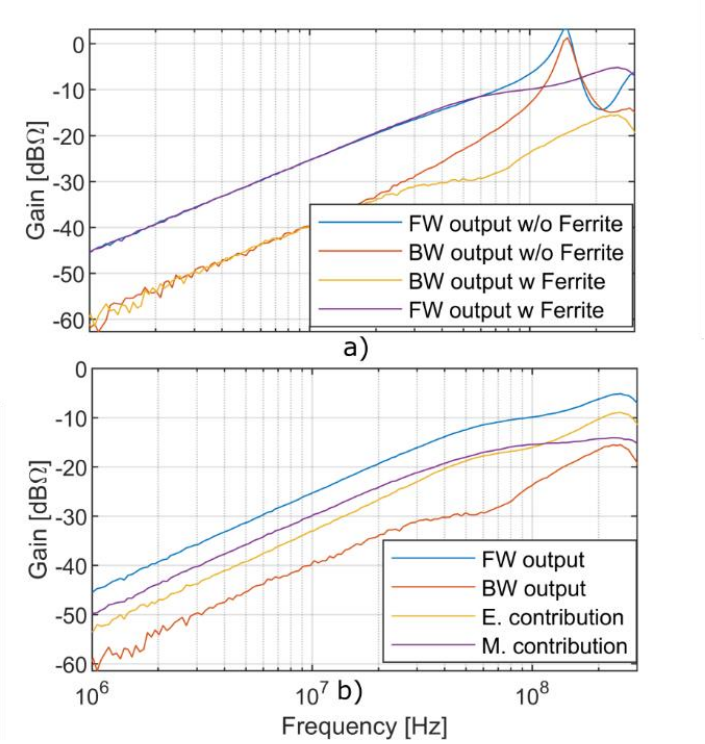

Figure 4.15. a) Forward and backward output frequency response with and without ferrite. b) Forward and backward outputs' frequency response with ferrite choke, and calculated magnetic and electric contributions, [80].

4.3.4. Testbench Experiments

The directivity and charge estimation of the directional GIS coupler were tested in the TEM testbench, where the input pulse and discontinuities are controllable, providing less uncertainty than a full-scale GIS. Two scenarios were examined: a discontinuity positioned far from the sensors without pulse overlapping and a discontinuity placed close to the sensors with pulse overlapping. The sensors' parameters for the combined sensors in Figure 4.10 and the DGISC are provided in Table 4.3.

Table 4.3. Electric and magnetic sensors' parameters with R=ZGIS=50 Ω.

	Electric parameters	Magnetic parameters	DGISC
k=	$RZ_{GIS}C_1 \approx 0.75$ nΩs	$M \approx 0.6$ nΩs	$M \approx 0.87$ nΩs
ω_1=	$1/C_2R \approx 6.7\text{x}10^8$ rad/s	$R/Ls \approx 3.7\text{x}10^8$ rad/s	NA

When a discontinuity is sufficiently distant from the sensor, the reflected pulse experiences a noticeable delay from the incident pulse. Figure 4.16 illustrates the DGISC's forward and backward measurements when the testbench is open-circuited at 520 cm from the sensors. In plots a) and b), the outputs are filtered with 190 MHz and 98 MHz LPF, resulting in a charge estimation error of 16% and 3%, respectively, as shown in Table 4.4. Improved reflection suppression and charge estimation were achieved with the 98 MHz LPF filter, as the electric and magnetic sensors' transfer functions exhibit more significant similarity at lower frequencies.

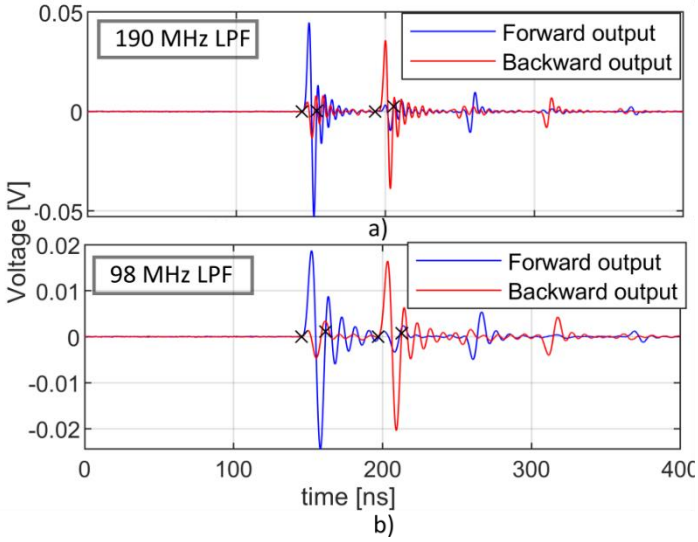

Figure 4.16 Measured incident and reflected pulse with a discontinuity 520 cm away from DGISC a) using a 190 MHz LPF and b) using 98 MHz LPF. The charge estimation zero-crossings are marked with an "x", [80].

When the discontinuity is close to the sensor's location, the incident and reflected pulses overlap, distorting the measured pulse. Figure 4.17 compares pulses without overlapping against those with overlap when the discontinuity is positioned 76 cm away. In 4.17 a), the electric and magnetic couplers' measurements are presented for both matched ("M" in the figure legend) and unmatched ("UM" in the figure legend) conditions. The forward and backward measurements from the software synergy and the DGISC are illustrated in 4.17 b) and c), respectively. The incident pulse is effectively segregated in both sensors, exhibiting a similar shape to the matched measurement. The DGISC, when utilizing the 98 MHz LPF, gave a 0.3% charge estimation error, representing the best estimation. The low errors with the DGISC can be attributed to the zero-time delay difference between the electric and magnetic contribution. In contrast, the software synergy requires the calculation of the time delay between the electric and magnetic sensors.

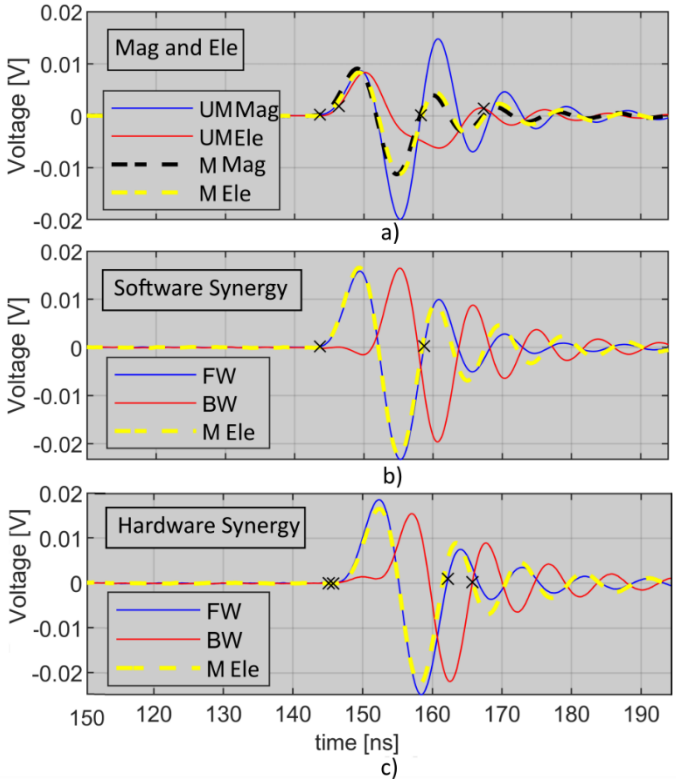

Figure 4.17. Comparison of matched pulses (M) and unmatched pulses (UM), using a) magnetic (Mag) and electric (Ele) sensors, b) software synergy's forward (FW) and backward (BW) components, and c) DGISC forward and backward components. The charge estimation zero-crossings are marked with an X, [80].

Table 4.4 Charge estimation error using software synergy and DGISC with 520 cm and 76 cm discontinuity.

Discontinuity distance	LPF	Software synergy	DGISC
520 cm	190 MHz	13 %	16 %
520 cm	98 MHz	22 %	3 %
76 cm	98 MHz	23 %	0.3 %

4.4. Full-scale GIS Experimentation

The fully matched testbench was employed to characterize the sensors under optimal conditions, free from reflections and subjected only to low-voltage signals. In contrast, a full-scale GIS is designed to withstand HV and comprises multiple sections such as spacers, bushings, circuit breakers, "T-sections", etc. Each of them acting as discontinuities to the propagating PD pulse, leading to the occurrence of multiple reflections.

4.4.1. Test Setup

Figure 4.18 a) illustrates a diagram of the GIS situated in TUDelft's HV lab, with the sensor's mounting holes denoted by an "S" followed by a number. The figure also identifies the discontinuities, with the spacers prevalent in almost every GIS flange. In this thesis, artificial PD defects were induced in test cells, allowing a controlled gas pressure in a confined volume. The figure specifies the two accessible locations of the test cells, where the voltage was generated using an HV source connected to the GIS bushing. A top-view sketch of the GIS

is presented in Figure 4.18 b), and a detailed magnification of both pictures is included in the appendix. This GIS is employed in the experiments conducted in this chapter, as well as in Chapters 5 and 6.

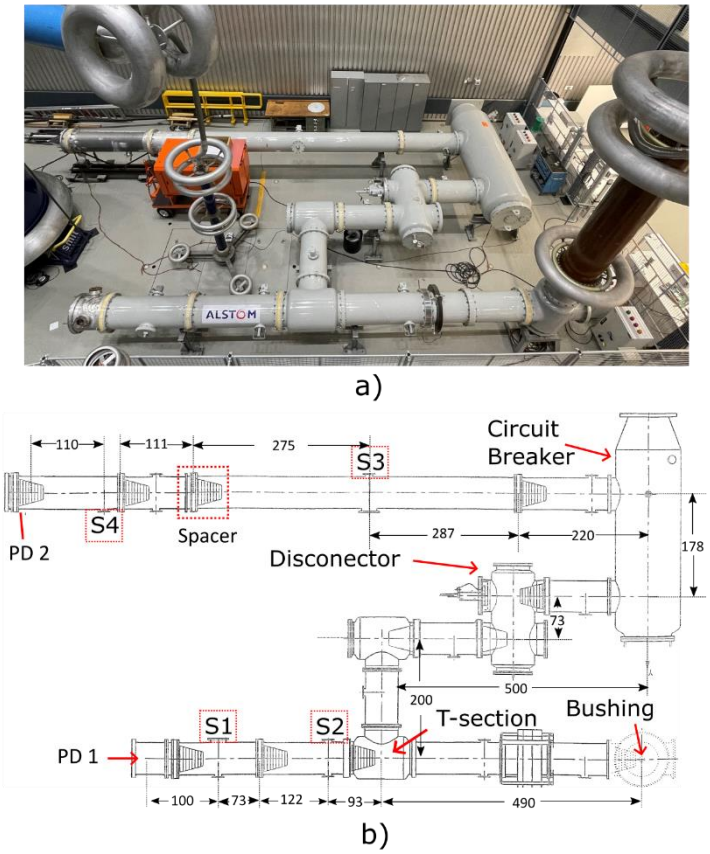

Figure 4.18 Full-scale GIS a) top view picture and b) sketch with positions indicated.

The following section shows the results for the software synergy and the DGISC in a single mounting hole of the full-scale gas-insulated substation shown in Figure 4.18. The PDs were generated in position 1, PD1, and the sensors were installed in S2, 93 cm away from the T-branch. The sensors' estimated charges were compared with a reference measurement. In the grounding connection of the test cell, a broadband (4 kHz-1 GHz) HFCT was coupled, allowing the charge calculation by means of the PD current integration. The defects were a Jumping Particle (JP) PD at 4.5 $bars_{abs}$ and a Surface Discharge (SD) at 3 $bars_{abs}$, and the sensors were connected to a 31.5 dB, 1 GHz voltage amplifier, followed by low-pass filters. For safety reasons, 5 V surge arresters with 100 MHz cut-off frequency were connected in parallel to the oscilloscope input. This test setup is illustrated in Figure 4.19

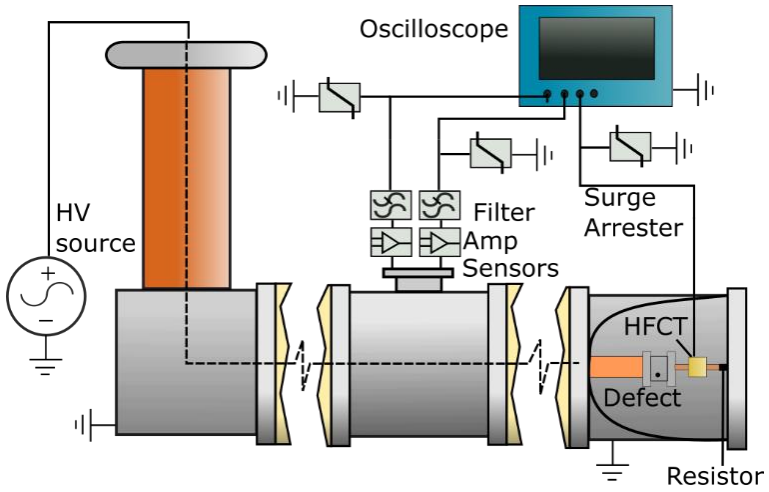

Figure 4.19 Full-scale GIS test setup, [31].

4.4.2. Results and Discussion

Table 4.5 displays the mean and standard deviation errors using different filters and sensors. These errors have a systematic and random component, where the standard deviation comes from the random noise and is more pronounced for lower-magnitude signals. Conversely, the systematic error is attributed to the charge estimation method, the calibration constant estimation (Chapter 5), and the overlapping of reflected pulses, where the last two are exclusive to this test setup.

The impedance change at the T-branch overlaps the incident pulse constructively for the magnetic measurements (overestimation) and destructively for the electric sensor (underestimation). This phenomenon can be seen in Table 4.5: as the filtered frequency decreases, the pulse duration increases, leading to overlapping. The software synergy significantly reduces charge estimation errors by mitigating reflection overlaps. Figure 4.20 compares the reference charge against the couplers and the software synergy filtered at 48 MHz: the magnetic coupler's charges are overestimated, and the electric coupler's ones are underestimated. For the DGISC, the best charge estimation is achieved when filtered at 48 MHz because the electric and magnetic contributions are more similar at lower frequencies. Figure 4.21 compares the reference charge against the DGISC filtered at 48 MHz. As expected, the forward values show a higher magnitude than the backward output, as the former is calculated for the incident pulse and the latter for the attenuated reflected pulse.

Table 4.5 Charge estimation error with different defects, LPFs, and sensors, [80].

Mean±Standard deviation error [%]				
LPF [MHz] @defect	Magnetic sensor	Electric sensor	Software Synergy	DGISC
48 @JP	51±9%	-32±4%	3±5%	9±4%
98 @JP	28±5%	-22±3%	-5±3%	25±8%
190 @JP	21±7%	-20±6%	-9±6%	25±8%
48 @SD	48±25%	-41±6%	-6±12%	-10±13%
98 @SD	-4±7%	-40±3%	-29±5%	-21±5%
190 @SD	-15±4%	-41±3%	-35±4%	-21±7%

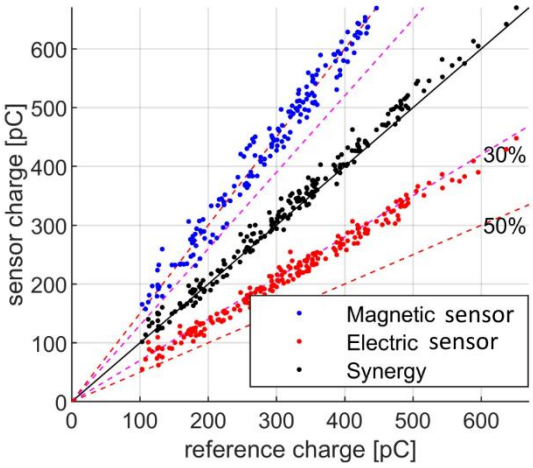

Figure 4.20 Charge estimation of jumping particle PD using magnetic and electric sensors and software synergy filtered at 48 MHz, [80].

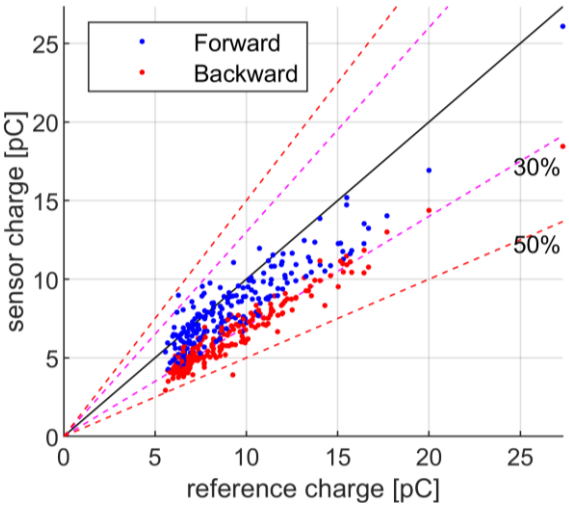

Figure 4.21 DGISC filtered at 48 MHz vs. reference charge for a surface discharge defect, [80].

Figure 4.22 shows the sensor's waveshapes for a jumping particle PD sample. Where a) is the reference measurement with the HFCT, b) is the measurements of the magnetic and electric antennas, and c) is the software synergy forward and backward components. The first backward pulse matches the location of the "T" section, confirming the reflection origin. The T-section is also identified in Figure 4.23, representing a SD measured with the DGISC at 48 MHz.

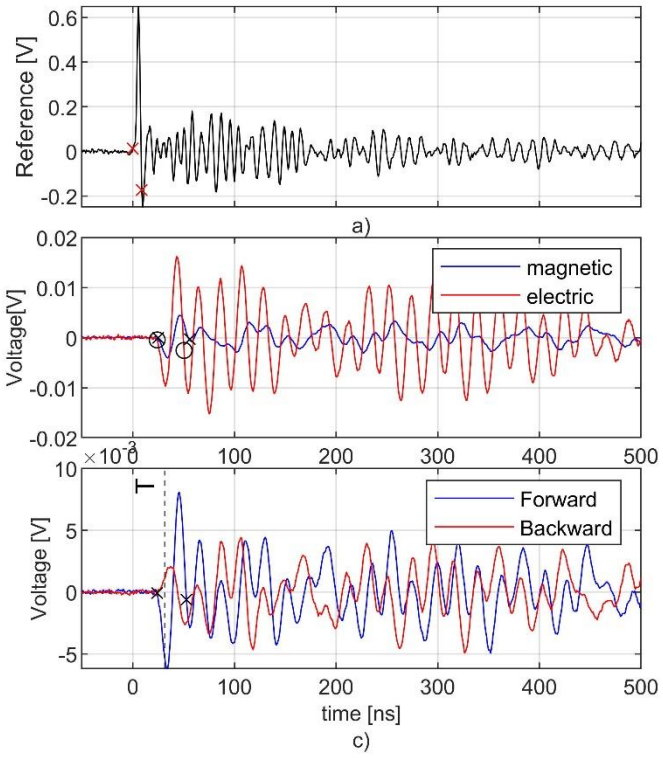

Figure 4.22. Waveshapes of a JP discharge measured with a) an HFCT, b) magnetic and electric sensors, and c) forward and backward components using the software synergy. The zero crossings for the charge estimation methods are marked with an X and a O, [80].

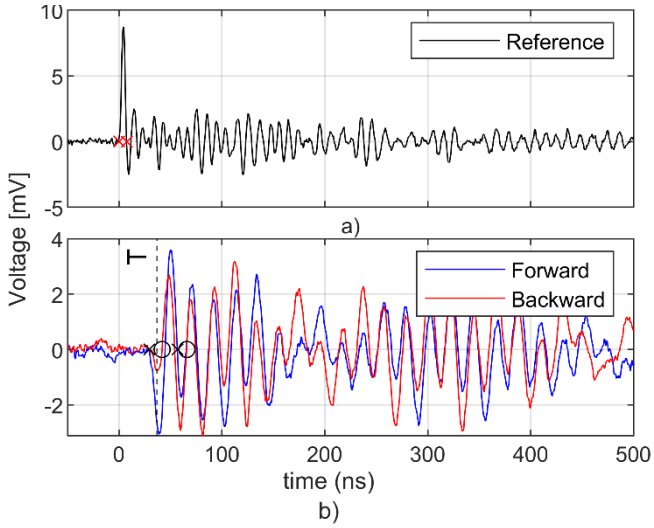

Figure 4.23. Waveshapes of a SD measured with a) an HFCT, b) the forward and backward outputs using the hardware synergy. The zero crossings for the charge estimation methods are marked with an X and a O, [80].

4.5. Chapter Conclusions

In GIS PD measurements, multiple discontinuities distort the waveshape and PD charge estimation. This chapter developed a PD reflection identification and suppression method using electric and magnetic sensors with a software and hardware combination.

The software combination method was approached with two scaling factors, helping to identify the pulse power flow and improve the waveshape and charge estimation. The synergy method was tested in a TEM testbench and the full-scale GIS, showing good charge estimation for different pulses and discontinuities, where the transformation filter approach showed a better reflection suppression than the peaks one. The power flow accurately located discontinuities in the GIS and testbench, even for overlapped pulses.

In most cases, the GIS mounting holes are already used for different purposes, making it convenient to place the PD sensors in a single one. The second part of the chapter addressed the challenges of electric and magnetic couplers sharing the same mounting hole, creating a high-voltage electric and magnetic sensor. The interactions between the electric and the magnetic couplers were addressed using a carbon-black-epoxy disk in the electric coupler. Ferrite chokes were used to adjust the electric and magnetic components in the DGISC, yielding satisfactory results distinguishing between PD's forward and backward components up to 100 MHz, improving the PD charge estimation. In the full-scale GIS, the DGISC showed better results than the software synergy at 50 MHz low pass filtered. However, the best results were obtained with the software synergy at a higher frequency, so this is the one used for the calibration process in the following chapter.

5

"When you can measure what you are speaking about, and express it in numbers, you know something about it".

- Lord Kelvin

5. Measuring System Charge Calibration*

The apparent charge calibration process establishes the specifications of a PD measurement system along with a procedure, facilitating the comparison of measurement results with standard values [81]. The severity of insulation degradation is assessed by the PD apparent charge, which harmonizes readings from various sensors. Calibrated PD measurements adhere to the IEC 60270 standard; however, this standard is limited to lumped element devices. Electrically extensive equipment, such as cables and gas-insulated systems, introduce significant resonances, attenuations, and reflections, rendering IEC 60270 insufficient for calibration. Nevertheless, unconventional sensors designed for conducted signals within a specific frequency range can be calibrated to determine charge magnitudes.

Previous chapters evaluated the measuring system's efficiency by comparing the charge of a reference source with the charge estimated using the proposed sensors. A calibration involves determining a calibration constant through comparison with a known parameter. This chapter first delves into the calibration procedure for both the testbench and the full-scale GIS. Subsequently, the calibration method is assessed in a LV testbench characterized by a low level of uncertainty and in an HV full-scale GIS, where numerous sources of uncertainty are present. Additionally, the measuring system's interoperability is

* This chapter is based on the following publications:

- C. Mier, A. Rodrigo Mor, L. Castro, and P. Vaessen, "Magnetic and electric antennas calibration for partial discharge charge estimation in gas-insulated substations," International Journal of Electric Power Energy Systems, vol. 141, no. January, p. 108226, 2022, doi: 10.1016/j.ijepes.2022.108226.
- C. Mier et al., "Methods for Partial Discharge Calibration in Gas-Insulated Substations for HVDC Power Grids and Charge Evaluation Uncertainty," IEEE Sensors Journal, vol. 23, no. 19, pp. 23486–23493, 2023, doi: 10.1109/JSEN.2023.3302871.

tested across three different laboratories within the framework of the EMPIR FutureEnergy project [22].

5.1. Calibration Method

5.1.1. The calibration Constant

Reference [56] demonstrates a method for calculating the PD charge with narrowband HFCT. The magnetic sensor presented in previous chapters works with the same principles as the HFCT but with lower inductive couplings. The equation (5.1) for the magnetic sensor was derived in section 3.2.1. If this equation is integrated twice, it results in (5.2). Now, considering that i_{pd} is a pulse of limited duration, v_o will tend to zero once the PD current vanishes, so the first term in the right hand of (5.2) converges to zero. The second term also disappears after some time since the integral of the output of a derivative sensor is zero. Therefore, the charge estimation can be simplified to the double integral of the output voltage divided by the magnetic coupling, as shown in (5.3). Reference [56] recommends integrating the signal to the second zero crossing of the signal to avoid noise accumulation. However, further investigation is needed to determine how this simplification is affected by filters.

$$\frac{di_{pd}(t)}{dt} = \frac{LC}{M}\frac{d^2v_o(t)}{dt^2} + \frac{L}{RM}\frac{dv_o(t)}{dt} + \frac{v_o(t)}{M} \tag{5.1}$$

$$q(t) = \frac{L_sC}{M}v_o(t) + \frac{L_s}{RM}\int_0^t v_o(t)dt + \frac{1}{M}\int_0^t\int_0^t v_o(t)dt^2 \tag{5.2}$$

$$Q \approx \frac{1}{M}\int_0^{t0}\int_0^{t0} v_o(t)dt^2 \tag{5.3}$$

A similar result is obtained in the electric sensor by deriving the electric circuit in section 3.3, resulting in (5.4). If this equation is integrated one time and is divided by the local characteristic impedance of the GIS (Z_0), it results in (5.5). With the same assumptions from the magnetic sensor, (5.5) can be simplified into (5.6).

$$v_{pd}(t) \approx \frac{LC_2}{RC_1}\frac{v_o(t)}{dt} + \frac{C_2}{C_1}v_o(t) + \frac{1}{C_1R}\int_0^t v_o(t)dt \tag{5.4}$$

$$q(t) \approx \frac{LC_2}{RC_1Z_0}v_o(t) + \frac{C_2}{C_1Z_0}\int_0^t v_o(t)dt + \frac{1}{C_1Z_0R}\int_0^t\int_0^t v_o(t)dt \tag{5.5}$$

$$Q \approx \frac{1}{C_1Z_0R}\int_0^{t0}\int_0^{t0} v_o(t)dt^2 \tag{5.6}$$

The coupling element (C_1 or M) in both sensors is inversely proportional to the charge. Additionally, the electric sensor also depends on the resistive load and the characteristic impedance of the PD propagation medium. If there are no GIS discontinuities (change of impedance) close to the sensor's location, the sensor sees a constant voltage-current propagation ratio. Therefore, the characteristic impedance is a local phenomenon dependent

on the GIS's local geometry and dielectric material, [65], and it is the one to be considered for calibration. These electric parameters inversely proportional to the charge are the ones used for the calibration process and are generalized as the calibration constant *k* (*M* or RC_1Z_0).

Equation (5.7) is the general transfer function for the electric and magnetic sensors, presented in section 3.3. From this equation, the calibration constant, *k*, can be determined by evaluating the function in the frequency domain when the frequency approaches zero, as shown in (5.8).

$$H(s) = \frac{sk}{s^2/{\omega_2}^2 + s/\omega_1 + 1} \tag{5.7}$$

$$k \approx lim \left| \frac{H(\omega)}{\omega} \right|_{\omega \to 0} \quad when\ \omega \neq 0 \tag{5.8}$$

5.1.2. Calibration in the Testbench

The calibration constant is obtained experimentally using the TEM testbench. Since the testbench is matched to 50 Ω, the injected voltage is guaranteed to be the same everywhere in the testbench, including where the sensors are positioned. Low-frequency sinusoidal signals were injected and measured in one of the transition cones and measured at the sensor's output voltage. The sinusoidal signal can be provided by a function generator or a vector network analyser and measured with an oscilloscope or with the same VNA. The VNA results are presented for the testbench and full-scale GIS calibration since it provides a sampled sweep.

Figure 5.1 shows the measured transfer function *H(f)* and, by using (5.8), the calculated calibration constant for the a) electric and b) magnetic sensors. In the same figure, the slope of the TF is shown: ideally, the calibration frequency range is valid before the slope diverges from the TF. At low-frequency, the calibration constant has higher variation caused by the sensors' low signal-to-noise ratio. At a higher frequency, the constant value starts to decay when the transfer function deviates from the slope. The calibration constant results in 1.22 nΩs and 0.95 nΩs for the electric and unbalanced shielded magnetic sensors, respectively.

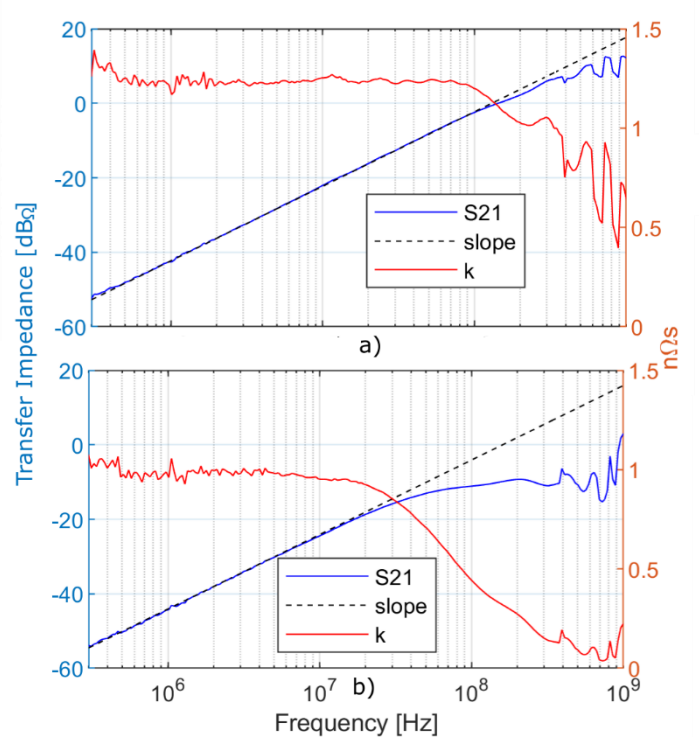

Figure 5.1 Electric (a) and magnetic (b) couplers' frequency response, slope, and calibration constant in the testbench, [82].

Given the calibration constants, the charge can be estimated in the testbench. A fast pulse was injected in one of the transition cones, and the sensor's output and the reference input were measured with a 3 GHz-50 Ω oscilloscope. Since the reference pulse was measured with the oscilloscope and a broadband HFCT sensor, the charge was calculated by means of the current pulse integration (section 2.1.3). Figure 5.2 a) shows the reference pulse, and Figure 5.2 b) illustrates the measured pulses using a 190 MHz-8th order LPFs. The electric sensor's oscillating response originates from the not-flat response and the band-pass filter response behaviour of the sensor. Table 5.1 gives the estimated charges and the error percentage compared to the reference charge. Part of the error is caused by the voltage-double-integration approximation when the integration time is reduced.

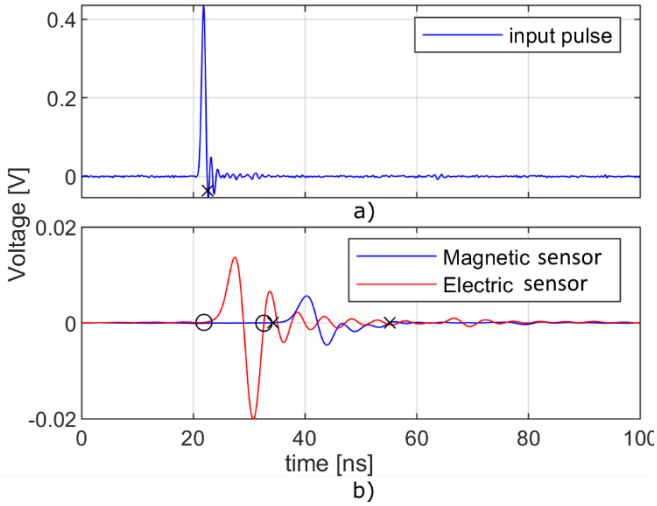

Figure 5.2 a) Injected pulse, and b) magnetic and electric sensors' measurement with the corresponding integration time limits (black crosses and circles), [82].

Table 5.1. Calculated charge and error estimation for the magnetic and electric sensors in the testbench.

	Charge [pC]	Error [%]
Reference	6.9	
Magnetic	6.3	-8.6
Electric	7.3	6.2

5.1.3. Calibration in a Full-Scale GIS

As shown in the previous chapter, the charge calibration constants for both sensors can be evaluated by determining the slope of the transfer function in the derivative response region. The following section explains the setup, results, frequency range limitation, and recommendations for the charge calibration procedure in full-scale GIS.

Because of the unmatched setup of the full-scale GIS, the calibration process differs from the one of the matched testbench. To calibrate using a VNA, it is necessary to have access to the output (B) port and reference (R) and test (TA) input ports, as shown in Figure 5.3 a) using the Anritzu MS4630B VNA. The magnetic sensor is calibrated in the following way (Figure 5.3 b): from the VNA's output port B (or function generator), the signal is injected into the GIS; at the GIS input, a HFCT is coupled, where its output is connected at the VNA reference port (or oscilloscope); and the sensor's output is connected through an amplifier to the VNA's TA output (or oscilloscope). A pre-calibration procedure in the VNA is needed to relate the sensor's output and the HFCT input current (V_o/I_i). The output port is connected with a single cable to the test port, where the HFCT is coupled, and the HFCT's output is connected to the reference port (Figure 5.3 a).

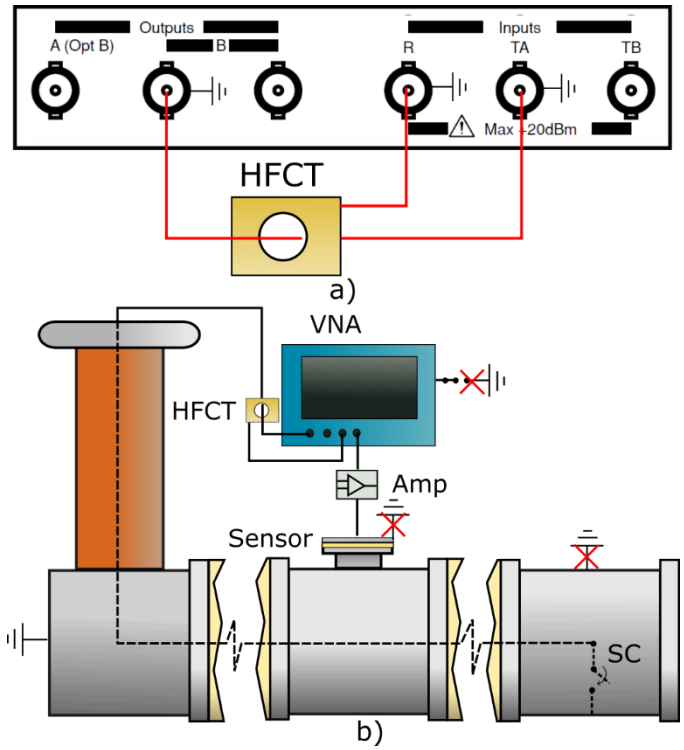

Figure 5.3 a) VNA ports and magnetic sensor pre-calibration. b) Magnetic coupler calibration setup in a full-scale GIS, [29].

The electric coupler is calibrated differently: a sinusoidal signal is injected from the VNA's B output (or function generator) to the GIS in parallel with the VNA's 1 MΩ loaded reference port (or oscilloscope). Then, the sensor's output signal goes to the VNA's TA input port (or oscilloscope) through an amplifier, as illustrated in Figure 5.4. A higher calibration sensitivity is obtained by open-circuiting and short-circuiting the GIS for the electric and magnetic sensors, respectively.

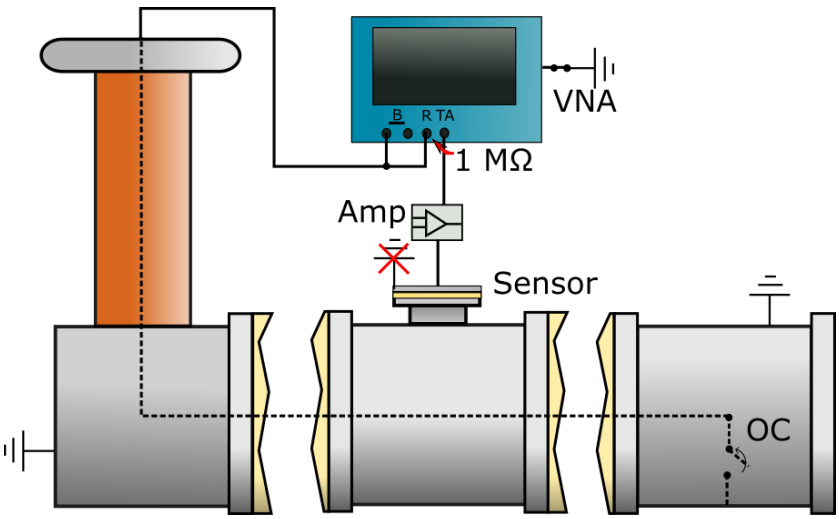

Figure 5.4 Electric sensor calibration setup in a full-scale GIS, [29].

Figure 5.5 shows the frequency response and calibration constants for the electric and magnetic sensors in the TU Delft GIS shown in Figure 4.18. The magnetic coupler's calibration

constant is obtained directly. In the case of the electric sensor, the obtained value must be multiplied by the local characteristic impedance of the GIS. Please note that the calibration is only valid for the specific sensor and location; the transverse geometry of the GIS and mounting hole dimensions might change for each section.

The measurements revealed that although the GIS geometry differs from the testbench, the calibration constants did not change significantly, resulting in 0.9 nΩs and 1.1 nΩs for the magnetic and electric sensor, respectively, when a GIS characteristic impedance of 70 Ω was used. Figure 5.5 shows that the calibration constant can only be obtained in a specific frequency range: the reason behind this limitation and the explanation of the deviations for the low and high-frequency range are explained in the following paragraphs.

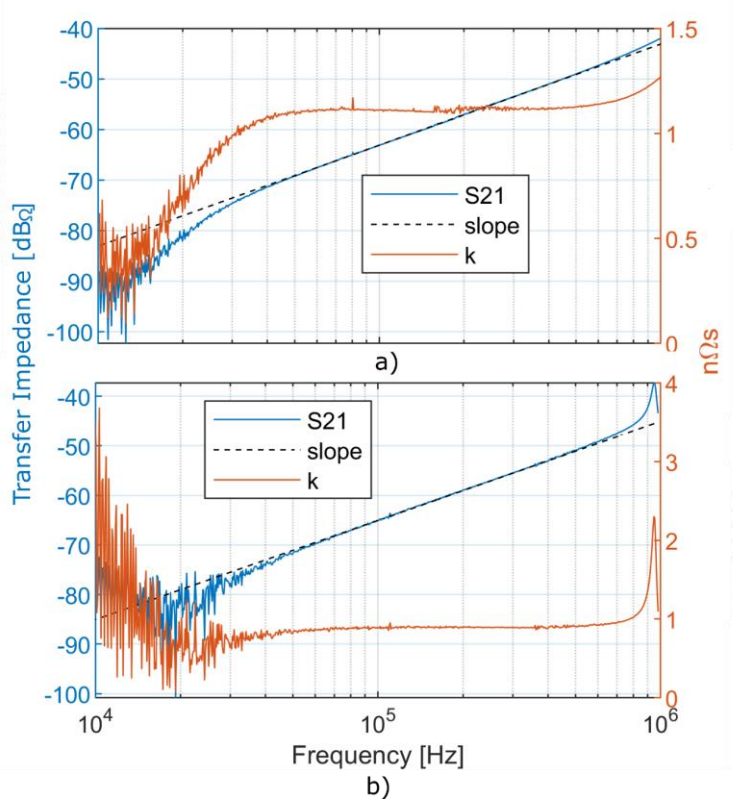

Figure 5.5 Frequency response, slope and calibration constant in a full-scale GIS for the a) electric and b) magnetic sensors [82].

High-frequency limit

The characteristic impedance of a full-scale GIS is not fully matched, creating reflections that modify the voltage and current through the GIS. Using TUDelft GIS dimensions (Z_0≈70 Ω, and a total length of around 28 m), a simulation of how the propagated signal changes at the sensor's location relative to the injection point ($V_0/V_i=I_0/I_i=\phi$) was performed in Figure 5.6. Figure 5.6 b) shows how ϕ is affected by frequency and with three different sensor positions relative to the injection point, where S=1 m is next to the injection point), S=14 m is in the middle of the total GIS length, and S=27 m is in the opposite end of the GIS. The measurements in Figure 5.5 show a similar tendency to the simulation when S=1 m, having a resonance near 1 MHz.

Assuming the worst case where the sensor is installed opposite to the injection point (S=l=28 m), the voltage can be obtained using (5.9), where z is the distance measured from the sensor location, β is the propagation constant and is the angular frequency (ω) over the phase velocity (v_p), and Γ is the reflection coefficient at the sensor's location. Evaluating (5.9) for $\boldsymbol{V}(-l) = \boldsymbol{V}_i$ and $\boldsymbol{V}(0) = \boldsymbol{V}_0$ results in (5.10).

$$\boldsymbol{V}(z) = \boldsymbol{V}_0{}^{+}\left[e^{-j\beta z} + \Gamma e^{j\beta z}\right] \tag{5.9}$$

$$\frac{\boldsymbol{V}_0}{\boldsymbol{V}_i} = \phi = \frac{1+\Gamma}{e^{j\beta l} + \Gamma e^{-j\beta l}} \tag{5.10}$$

By using (5.10) when the GIS is open-circuited (Γ=1), the maximum frequency (f_m), at which the signal variation is equal or less to ϕ, can be obtained as a function of the GIS length resulting in (5.11). The current ratio (I_0/I_i) evaluation also results in (5.10) and (5.11).

$$f_m(l) = -jln\left(\frac{1-\sqrt{1-\phi^2}}{\phi}\right)\frac{V_p}{2\pi l} \tag{5.11}$$

Using (5.11), Figure 5.6 c) shows the frequency limit for different GIS lengths and signal variations (ϕ=1.01, 1.03, 1.05). Previous equations are just an approximation: a real GIS has multiple discontinuities with different characteristic impedances and lumped inductance and capacitance in the short and open circuits.

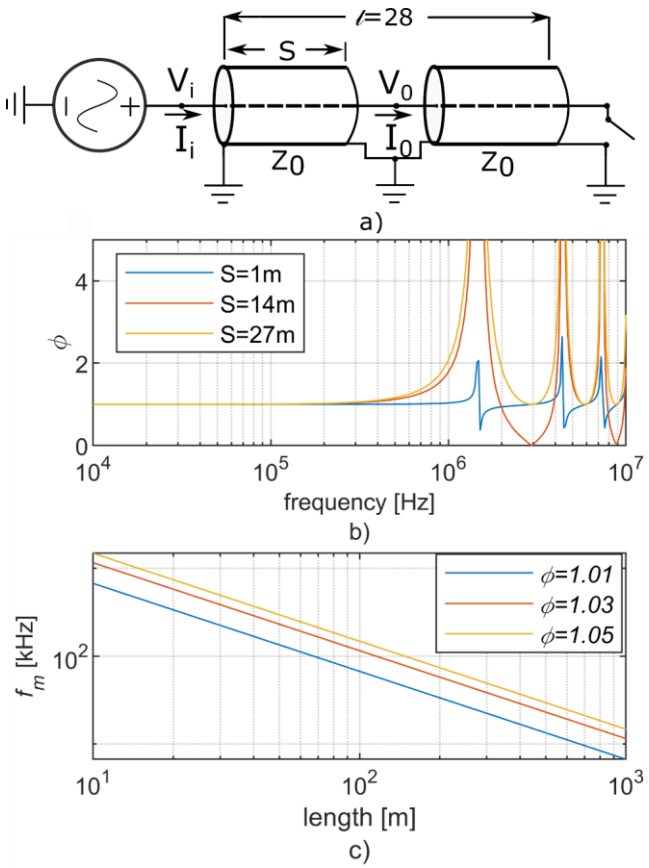

Figure 5.6 a) GIS electric circuit representation. b) Signal ratio for different sensor positions. c) Frequency limit as a function of GIS length for 1%, 3%, and 5% of signal variation, [29].

Low-frequency limit

In the low-frequency range, the noise can be attributed to the following reasons (ordered by higher contribution):

- **Sensor's sensitivity:** the sensors' sensitivity is proportional to the frequency.
- **Common-mode currents:** not all the current returns through the GIS' enclosure; a small percentage flows as a common-mode through the sensor's coaxial cable feeder, inducing noise in the measurements. This noise was already observed at the tens of kHz range, eclipsing the calibration constant value.
- **Ground paths:** the magnetic loop couples the current in the GIS' enclosure, so any fraction of current flowing in another path affects the calibration constant value. The influence of the ground paths in the measurements was relevant below 3 kHz.

Recommendations

In practice, using instruments with frequency sweep capabilities might not be feasible because of cost, weight, or equipment availability. In that case, only a single-frequency signal might be available, and calibration can be performed using one or multiple single-frequency measurements to calculate the slope. To that end, some recommendations are given for a proper calibration frequency selection:

- The GIS length can be shortened by opening a disconnector (electric calibration) or closing a ground switch (magnetic calibration) close to the sensor, increasing the calibration frequency range.
- The frequency limit is increased by injecting the signal near the sensor's location.
- Even though (5.11) is an approximation, it can be used as a reference for choosing the maximum frequency at which the calibration constant can be obtained. A minimum voltage variation tolerance is recommended since, as shown in Figure 5.6 c), the frequency limit increases logarithmically with φ, but the calibration constant error rises linearly.
- The common-mode current is reduced by insulating the sensors from the GIS during the calibration.
- If the calibration is performed in the range below 3 kHz, it is recommended that the source and any path that bypasses the magnetic sensor's mounting hole are floated during the calibration process (indicated with red crosses in Figure 5.3 b).
- Ideally, for a given GIS and sensor, the calibration constants could be determined using a built-on-purpose testbench.

5.1.4. Calibration for the Synergy Methods

Software combination calibration constant

The previous chapter demonstrated two methods for reflection suppression by combining electric and magnetic sensors. The resultant pulse charge is also affected since both methods superimpose the voltage and current measurements. Equation (5.12) is an extension when multiple sensors' outputs are superimposed, where V_{em} is the addition of both sensors.

$$\iint_0^{t0} (v_e(t) + v_m(t))dt \approx Q(k_e + k_m) \rightarrow Q \approx \frac{1}{k_e + k_m} \iint_0^{t0} v_{em}(t)dt \tag{5.12}$$

In the transformation filter method applied to the magnetic sensor, the magnetic calibration constant results equal to the electric one (5.13). Hence, the v_{em} charge estimation results in Q_{tf}, given by (5.14) (the same conclusion is obtained when transforming the electric output). The peaks method similarly changes the charge: when the sensor's output in (5.12) is scaled by the peaks factor (C_{pk}), the calibration constant is affected by the same factor, resulting in the approximated charge Q_{pk} shown in (5.15). If both sensors have the same cut-off frequency, $k_m C_{pk} = k_e$, the charge is estimated as in (5.14).

$$k_m \approx lim \left| \frac{G_m(\omega) H_{e/m}(\omega)}{\omega} \right|_{\omega \rightarrow 0} \approx k_e \tag{5.13}$$

$$Q_{tf} \approx \frac{1}{2k_e}\iint_0^{t0} v_{em}(t)dt \tag{5.14}$$

$$\iint_0^{t0}\left(v_e(t) + v_m(t)C_{pk}\right)dt \approx Q(k_e + k_m C_{pk}) \rightarrow Q_{pk} \approx \frac{1}{k_e + k_m C_{pk}}\iint_0^{t0} v_{em}(t)dt \tag{5.15}$$

Hardware combination calibration constant

The PD charge for the directional GIS coupler can be obtained using the principle of superposition, where the charge estimation (Q_{DGISC}) is proportional to the addition of electric and magnetic constants, resulting in (5.16). These calibration constants can be obtained by measuring frequency response.

$$Q_{DGIS} \approx \frac{1}{k_e + k_m}\iint_0^{t0} v_0(t)dt \tag{5.16}$$

Figure 5.7 depicts the calibration constant of the DGISC with its electric and magnetic contributions. The electric component (red) is obtained with an opened-circuited testbench, the magnetic one (yellow) with a short-circuited testbench, and the DGISC in the matched testbench (blue). In the 1-10 MHz range, the calibration constant is 0.35 nΩs and 0.52 nΩs for the electric and magnetic contributions, respectively. Adding both components yields the same value as the DGISC's matched measurement of 0.87 nΩs. These results demonstrate that the calibration constant of the DGISC is equal to its electric and magnetic components' superposition.

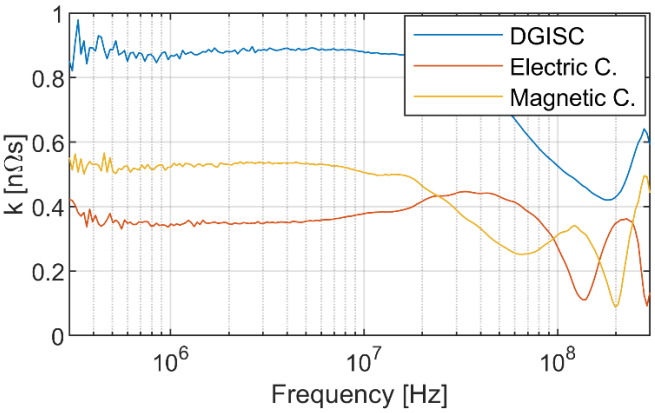

Figure 5.7 Calibration constant of the DGISC and electric and magnetic contributions, [80].

While these measurements were conducted on the TEM testbench, determining the DGISC calibration constant directly in a full-scale GIS is challenging due to multiple discontinuities. The same approach from the individual couplers can be applied to the DGISC, but it requires short-circuiting the GIS for the magnetic contribution and open-circuiting it for the electric one.

5.2. Measuring System Evaluation Intercomparison

As part of the 19ENG02 FutureEnergy, the interoperability of the calibration method is evaluated in three different laboratories. The uncertainty is estimated in a low-voltage testbench free of reflections and in a full-scale GIS, where the measuring system repeatability was tested in 3 laboratories: TUDelft in Delft, Netherlands; Laboratorio Central Oficial de Electrotecnia (LCOE) in Madrid, Spain; and SuperGrid Institute (SGI) in Lyon, France. The sensors' linearity, pulse width, and noise were evaluated in the LV testbench for the first two laboratories, and real PDs from different defects were considered for the three laboratories' full-scale GIS. All laboratories used the V2I and the software synergy methods, using the available software [83] created during this thesis and project.

The noise, the integration time limit, and pulse overlapping increase the charge estimation error. The measurement error quantifies the uncertainty of a measuring system. This error is composed of a random component and a systematic component. Random errors arise from stochastic variations on influence quantities, and systematic error comes from a recognized effect of an influence quantity. The random error can be corrected by averaging an infinite number of measurements of the same measurand carried out under repeatability conditions ([24], [81]). White noise is critical in the calibration method, and PD measurements cannot be averaged since every sample is different with no repeatable conditions. The influence of these errors in the measuring system is evaluated with uncertainty.

This section first explains each laboratory's test setups and sensors. Then, the methods used to calibrate and characterize the sensors are presented, and in the last part, the results are shown and discussed.

5.2.1. Test Setups and Calibration Methodology

The calibration method uncertainty was assessed with a calibrated reference in a LV test setup. Furthermore, a full-scale GIS with real PD was used to evaluate the measuring system in real operation.

The LV tests were conducted in testbenches using calibrated PD pulses as a reference. TUDelft and LCOE used a GIS section adapted to impedance-matching cones to reduce reflections [84]. From this LV characterization, calibration constants for the VHF sensors were obtained. PD charge linearity, pulse width, and noise level tests were analysed, considering that these factors depend not only on the sensor but also on the signal processing (software) and the signal conditioning (hardware). The measurements were carried out with calibrated oscilloscopes, where the uncertainty of these oscilloscopes is negligible compared to the evaluated measuring system.

Once the sensors' characterization was performed, HV tests were carried out in the three laboratories using representative defects in GIS. Each laboratory used different HV voltage sources, PD defects, and reference sensors.

Low-voltage test setup

TUDelft and LCOE participated with the LV testbenches, explained as follows.

TUDelft used the testbench presented in section 3.1. For the uncertainty tests, the calibrator and the noise were injected at the input port and measured with an oscilloscope at the output cone. The electric and magnetic sensors were mounted and connected to the oscilloscope through Mini-Circuits ZFL-500LN+ amplifiers. The linearity test was performed with an “LDC-5/UHF” calibrator injecting 5 pC (minimum allowed charge according to [85]) to 500 pC. The noise test was performed with the same calibrator injecting a constant 26 pC pulse in parallel with a 200 MHz white noise from 100 mV up to 1 V. Reference [47] demonstrates that an SF_6 PD has a duration below 1 ns, which is not the case for new alternative gases, having slower pulses, as shown in section 2.1.2 and [48]. Therefore, pulses from 11 to 400 ns were injected using a wave generator.

LCOE used the testbench shown in Figure 5.8. This comprises a 7 m-long full-scale GIS with a 50 Ω characteristic impedance. At 1.8 m from the injection point, the sensors were installed and connected directly to the high-bandwidth digital oscilloscope (without amplifiers). Then, the GIS was terminated with a 30 kV, 20 m long cable. The linearity test was carried out with an "LDC-5/UHF" calibrator, injecting pulses from 5 pC up to 500 pC. The noise test was also performed with the same calibrator, injecting a constant 50 pC pulse in parallel with a BK wave generator, providing a 100 MHz bandwidth Gaussian noise of 100 mV to 1 V amplitude. Finally, using the same generator, the frequency dependence test was performed by injecting pulses with a duration from 2.4 to 15 ns (the largest possible pulse width due to reflection in the GIS).

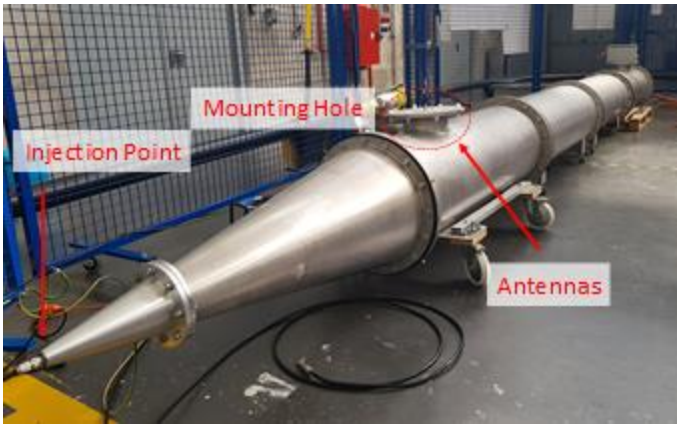

Figure 5.8 LCOE LV setup, [32].

High-voltage test setup

TUDelft, LCOE, and SGI participated using the following test setups.

Figure 5.9 presents the HV test setup used by TUDelft, indicating the sensors and references’ connections. The IEC 60270 method and a HFCT were used as the reference measurement. On one hand, the conventional method provides a measurement with a high signal-to-noise ratio but inaccuracy for high repetition discharges. On the other hand, the

HFCT's current integration method is more affected by noise but not by the repetition rate. Both reference methods were triggered simultaneously and compared in the oscilloscope.

The defects, generated with AC and DC+/- HV sources, consisted of 4 bar_{rel} SF_6-filled test cells with a protrusion (Cor), a surface defect, a jumping particle, and a 2 bar_{abs} Floating Electrode (FE). Due to the protrusion and surface defects low magnitudes, the ZFL-500LN+ amplifier was used for these defects. Additionally, the signals were filtered with a 190 MHz 8^{th}-order LPF. The floating electrode has a low repetition rate for DC voltages. Therefore, the FE discharge was accelerated by pre-discharging it with a protrusion, similar to what was done in [86]. The sensors were located in S1 and S2, as indicated in the GIS sketch in the appendix. The HV coupling capacitor was connected between the HV source and the bushing.

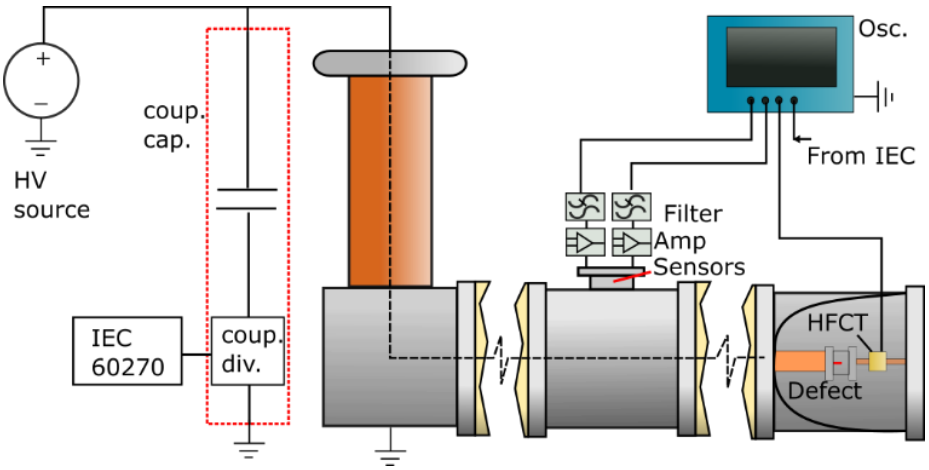

Figure 5.9 TUDelft HV test setup, [32].

LCOE used the same GIS from Figure 5.8 but with an HV configuration. Figure 5.10 shows the sensors, the test cells, and the coupling capacitor, which was used as the reference. The SF_6 test cells were installed 1 m from the sensors. The pulses were generated in the test cells with an AC and a DC+/- source and were measured according to the IEC 60270 method. The signals from the measuring impedance and the VHF sensors were recorded simultaneously with the oscilloscope. Due to the low amplitudes of the protrusion and surface defects, both couplers were connected to the oscilloscope through Mini-Circuits ZFL-500LN+ amplifiers.

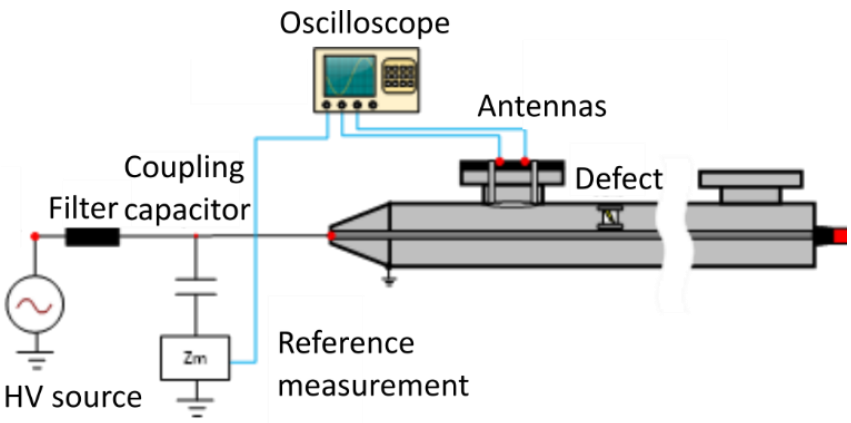

Figure 5.10 Schematic of the LCOE HV test setup, [32]**.**

SuperGrid Institute used the GIS presented in Figure 5.11. This HV test setup used a DC negative power supply connected with a full-size GIS through a coaxial HV cable. The setup comprised an HV protecting resistor, a coupling capacitor for conventional measurements, and a test compartment filled with 6.5 bar_{abs} SF_6. In this compartment, the defects (either a protrusion or a jumping particle held by a wire) and the sensors were placed, including a measurement electrode connecting the defect to ground through the reference sensor. Depending on the test, several sensing systems were acquired in parallel with an oscilloscope, among:

- Conventional apparent charge according to IEC 60270.
- Magnetic sensor with amplifier Femto HCA-400M-5K-C.
- UHF sensor with amplifier R&K LA-120-0S.
- HFCT or current probe on the measurement electrode.

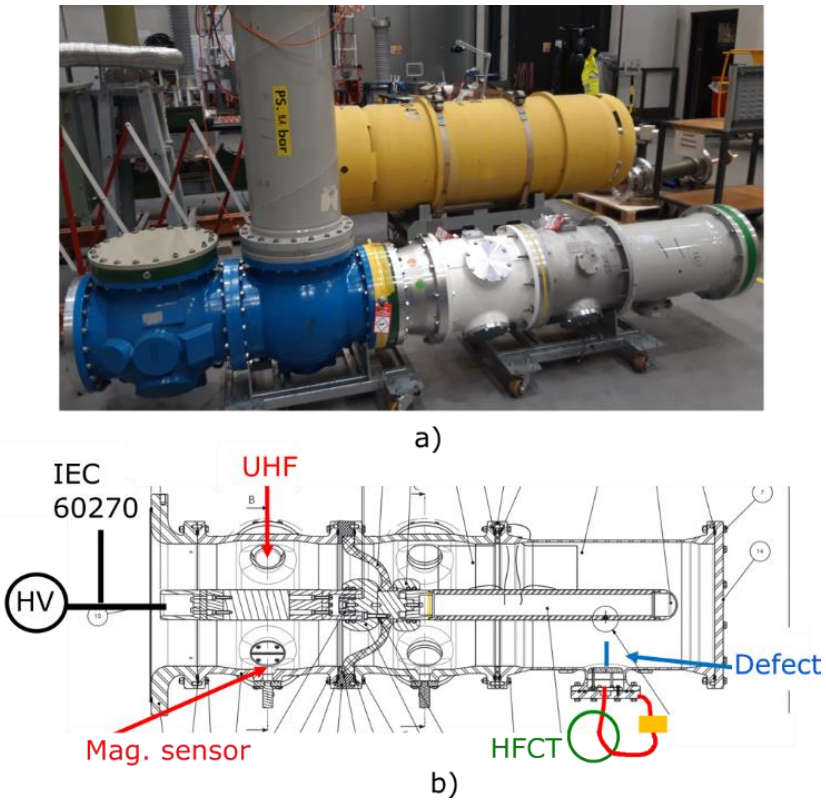

Figure 5.11 Picture of the test setup and b) schematic of the sensor placed in it, [32].

The noise was applied with a function generator placed between the end of the enclosure and the earth of the test platform, so the noise propagated in the enclosure. Two different noises were used: a 10 V sinewave at 20 MHz and a white noise with components up to 20 MHz with an applied amplitude of up to 10 V.

5.2.2. Sensor's Characterization and Calibration

Sensors design for each calibration setup

Each participant laboratory has a unique GIS geometry, resulting in a different magnetic and electric sensor design. Although the sensors differ in dimensions, all sensors' principles are the same. For TUDelft and LCOE, the electric coupler was a handmade disk-type UHF sensor sharing the same mounting hole with the magnetic sensor. On the other hand, SGI used a commercial disk-type UHF installed in a dedicated mounting hole located in the same transversal position as the magnetic loop. Having the sensors in the same transversal position ensures the PD pulse electromagnetic field's simultaneous arrival for both probes. A balanced magnetic loop design was chosen for all laboratories, giving higher common mode noise rejection. Figure 4.10, Figure 5.12 and Figure 5.13 show each laboratory sensor with their respective dimensions. TUDelft used different setups for the HV and LV tests, giving different electric parameters.

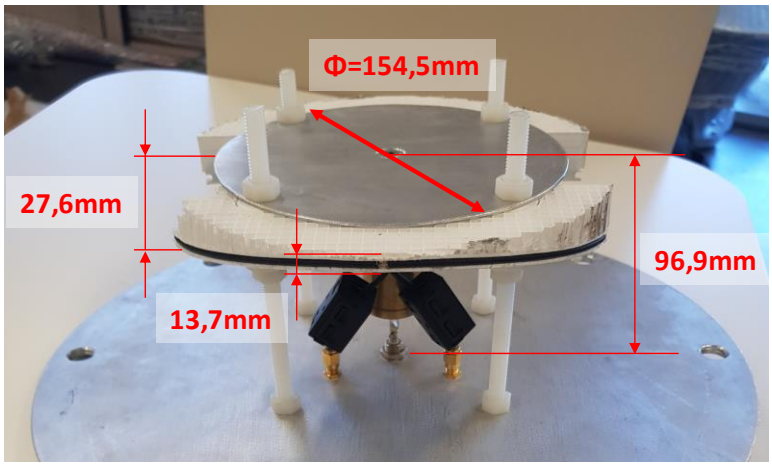

Figure 5.12 LCOE magnetic and electric sensor dimensions, [32].

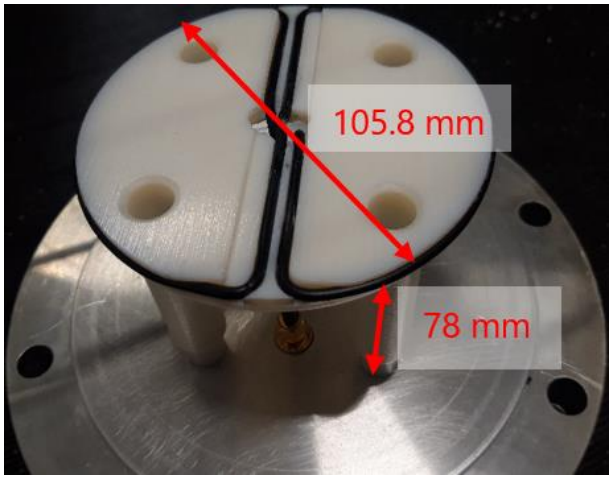

Figure 5.13 SGI magnetic loop dimensions, [32].

Sensors' parameters and calibration constants

The calibration constants for each laboratory were obtained following the frequency-domain calibration procedure explained in the previous section. Taking LCOE calibration as an example, the frequency-domain method and a proposed time-domain method are compared and explained in this section.

For the frequency-domain calibration, LCOE injected 15 V_{pp} sinusoidal signals with frequencies between 10 kHz and 120 MHz in the test setup shown in Figure 5.8. The magnetic loop was characterized by measuring its output voltage and the injected current through an HFCT. For the electric coupler, the voltage at the injection point and its output were measured directly on the oscilloscope. In order to reduce the noise, an average of 5 measurements were performed. Figure 5.14 shows the measured frequency responses (H) and the linear fit, whose slope represents the a) magnetic and b) electric sensors calibration constants (k_m =1.50 nΩs, and k_e=3.16 nΩs). The frequency responses show resonances starting around 10 MHz, generated by the GIS unmatched length. Therefore, the sensor's sensitivity limits the lowest frequency to be considered, whereas the GIS resonance limits the highest frequency in the

calibration constant calculation. Thus, the calibration constants (k_e and k_m) were found in the frequency range between 10-500 kHz.

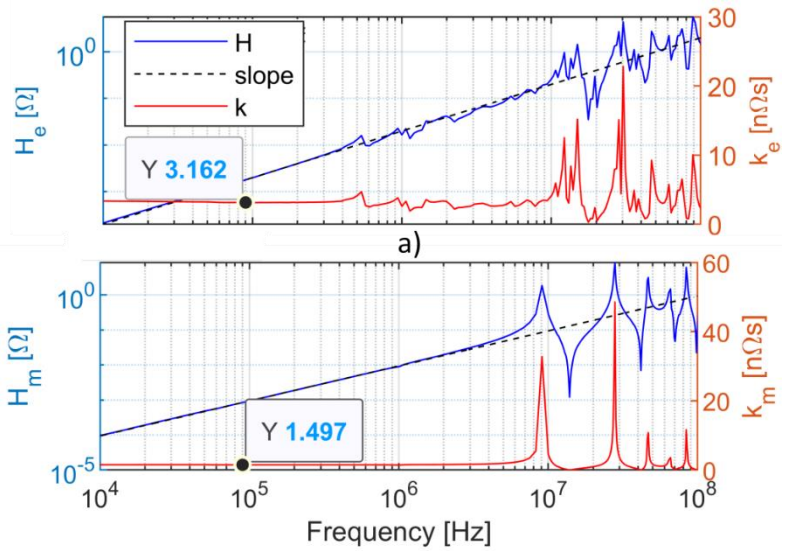

Figure 5.14 LCOE frequency-domain calibration for the a) electric and b) magnetic sensors, where *k* corresponds to the calibration constants, [87].

LCOE proposed a time-domain method to validate the calibration constants where a linearity test was performed using a calibrator. One hundred PD pulses were injected for each charge between 5 pC and 500 pC, where the injected PD pulse and the sensors' output signals were measured simultaneously. The injected PD pulse was measured with a reference HFCT. The injected PD pulse charge (Q_{HFCT}) was calculated by direct integration of the measured PD pulse current, whereas for the VHF sensors, the voltage-double-integration method was applied without considering any calibration constant (Q'_m for the magnetic coupler and Q'_e for the electric one). Considering that in the V2I method, the charge is inversely proportional to the calibration constant, these were calculated by dividing the sensors' estimated charge by the charge measured with the HFTC ($k'_m=Q'_m/Q_{HFCT}$ and $k'_e=Q'_e/Q_{HFCT}$). As shown in Table 5.2, the calibration constants resulting from the time-domain approach (k'_m=1.49 nH and k'_e =3.20 nΩs) were very close to the calculated ones from the frequency response, confirming the obtained values.

Table 5.2. Verification of the calibration constants of the sensors employing a linearity test, [87].

Q_{inj} [pC]	Q'_m [pC]	Q'_e [pC]	k'_m [nΩ·s]	k'_e [nΩ·s]
25	3.62E-08	8.00E-08	1.45	3.20
50	7.45E-08	1.60E-07	1.50	3.22
100	1.49E-07	3.22E-07	1.50	3.22
200	2.97E-07	6.39E-07	1.49	3.21
350	5.24E-07	1.13E-06	1.49	3.22
500	7.50E-07	1.61E-06	1.50	3.22
		Mean	1.49	3.20
		std (%)	0.29%	0.76%

The rest of the electrical parameters were used for the software combination method and were found in different ways by each laboratory. LCOE used an RLC bridge to measure the magnetic sensor's self-inductance (L_s) and the electric sensor's parasitic capacitance (C_2). TUDelft found the values by fitting the model (5.7) with the frequency response measured in the testbench. Also, TUDelft and SGI calculated the parameters using a finite element method simulation. These parameters are presented in Table 5.3.

Table 5.3 Electric and magnetic sensors' parameters for each laboratory, [32].

Sensor parameters	TUDelft – LV/HV	LCOE	SGI
k_m [nΩs]	0.56/0.68	1.50	1.1
L_s [nH]	161	290	186
k_e [nΩs]	0.73/2.05	3.24	1.2
C_2 [pF]	33/35	14.3	6.5
R [Ω]	50	50	50
Z_0 [Ω]	50/65	50	85

5.2.3. Results and Discussions

This section presents the calibration method's uncertainty in the different laboratories' LV and HV test setups.

LV test results

TUDelft

Figure 5.15 to Figure 5.17 show the average and standard deviation error of 100 samples for each test. Figure 5.15 shows the uncertainty for different charge values. As expected, the average does not change with the PD magnitude; however, at high charge values, the mean error rises due to the amplifier's dynamic range. The amplifier saturates with the pulse high magnitude. Conversely, the standard deviation decreases with the charge magnitude, attributed to the higher signal-to-noise ratio. Figure 5.16 shows the uncertainty for different pulse widths. In the case of the magnetic loop, the average error is maintained almost constant for longer pulses, which is not the case for the electric coupler. This is attributed to the pulses' bandwidth and the carbon-black-epoxy non-frequency linearity. For the standard deviation trend, it increases with the pulse width because of the reduction of the SNR. In conclusion, the noise mainly affects the magnitude linearity and pulse widths.

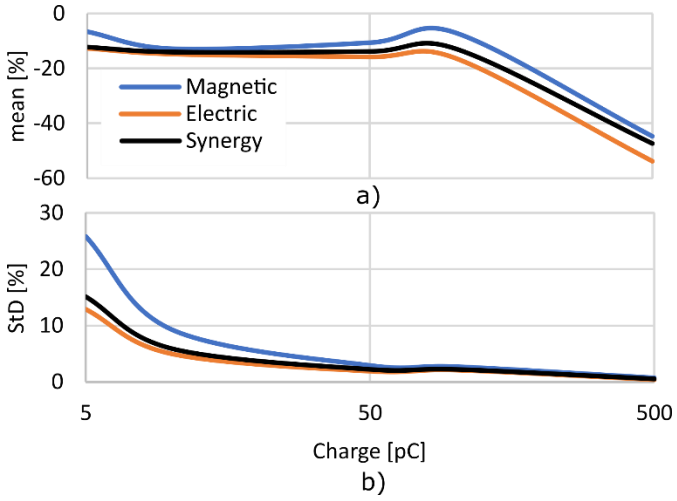

Figure 5.15 TUDelft linearity test's a) mean error and b) standard deviation, [87].

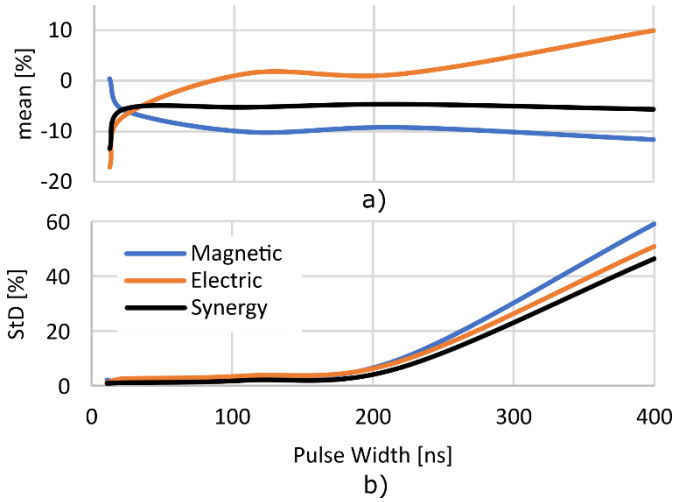

Figure 5.16 TUDelft pulse width test's a) mean error and b) standard deviation, [87].

Figure 5.17 shows the uncertainty for different noise levels, represented as the RMS-Noise-to-signal-Peak Ratio (NPR). The white noise is a random error, and it is expected that the mean error is not affected in a large batch, which was not observed in the results. A random noise has the same probability of increasing or decreasing the signal integration time. However, the output charge depends quadratically on the integration time, over-estimating the charge. The standard deviation increases with noise, showing the same trend as the other tests.

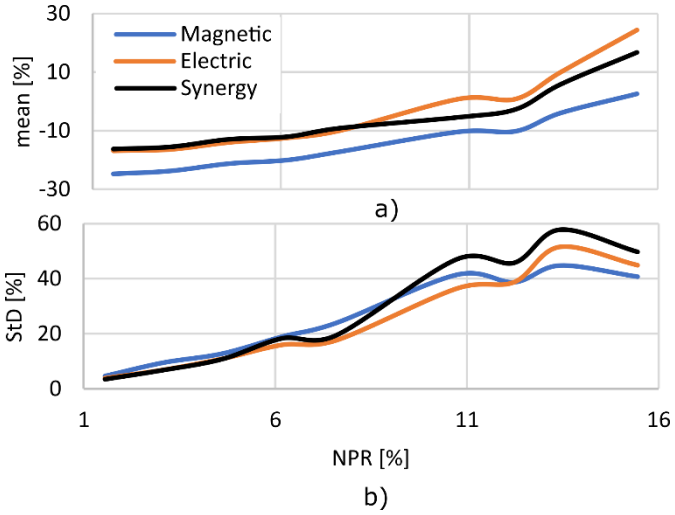

Figure 5.17 TUDelft noise level test's a) mean error and b) standard deviation, [87].

LCOE

For the linearity test, 100 reference pulses were injected into the GIS using the calibrator. Figure 5.18 shows the mean and standard deviation errors between the injected PD charge and the sensors. Due to the magnetic loop's lower sensitivity and the non-use of amplifiers, the mean error at low charges (≤10 pC) was significant; nevertheless, the mean error was below 0.5 % for higher charges. For the electric coupler, due to its higher sensitivity, the mean error remained almost constant for all injected PD charges, between 1% and 3.6%. The standard deviation decreases as the PD charge increases due to the higher signal-to-noise ratio.

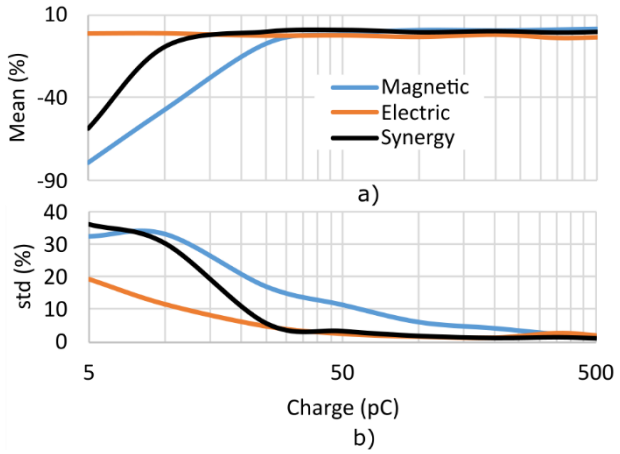

Figure 5.18 LCOE linearity test's a) mean error and b) standard deviation, [87].

The pulse width influence was determined by injecting 100 pulses with different durations. Figure 5.19 shows the magnetic and electric sensors and synergy's mean errors and standard deviation. The longer time of the pulses reduces the SNR of all sensors, especially the magnetic coupler, which has a lower sensitivity than the electric one. In the TUDelft tests, amplifiers were used to increase the sensitivity, and the gain difference between sensors was lower (see Table 5.3).

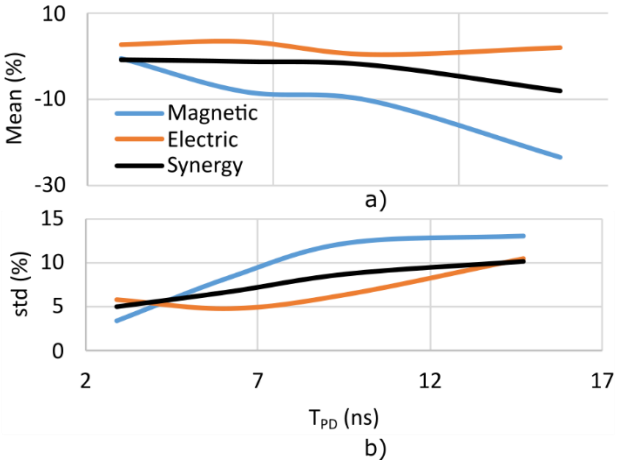

Figure 5.19 LCOE pulse width test's a) mean error and b) standard deviation, [87].

For the noise influence, superimposed Gaussian noise was injected between the GIS enclosure and the ground. One hundred PD pulses of 50 pC were injected and measured for each noise level. Figure 5.20 shows the obtained mean errors and standard deviation for different noises. The measurement of the electric sensor was more affected by the noise, showing an increasing error with the noise level, whereas the magnetic loop's absolute errors remained below 5%. The same behaviour occurred for the standard deviation.

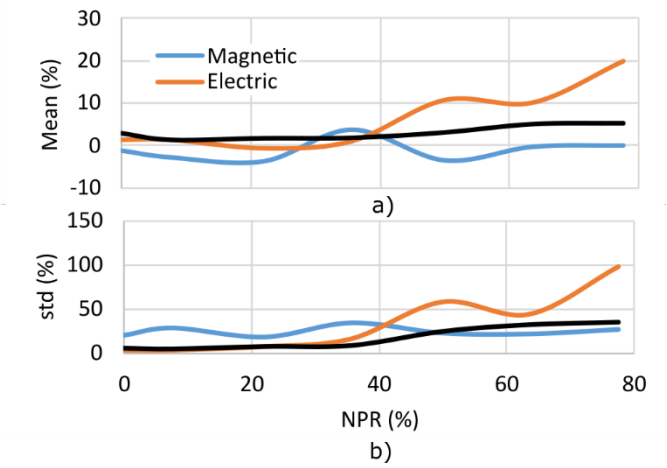

Figure 5.20 LCOE noise level a) mean error and b) standard deviation, [87].

The main uncertainty source for both laboratories is noise, affecting the magnitude and frequency linearity. Also, the V2I method loses accuracy when the pulse is not integrated to infinite. In the LV test, where there are no discontinuities, the synergy method gives an intermediate result from both sensors.

HV test results

The LV tests showed that the PD charge estimation error is mainly attributed to the noise and the V2I integration time. In the HV test, the full-scale GIS introduces more error sources, such as wave reflections, resonances, and calibration constant estimation, which are determined by the GIS size. In the following sections, the results for the three laboratories are

tabulated, representing the magnetic loop, the electric coupler, and their combination as MS, ES, and Syn, respectively.

TUDelft

The mean and standard deviation errors are presented in Table 5.4. On the other hand, the magnitude of PD defects affects the SNR and, hence, the charge estimation. The IEC method shows a high error for the protrusion and the DC floating electrode. This error is attributed to the corona's high repetition and IEC's low time resolution, resulting in overlapped pulses. This IEC low-resolution error is known from literature [88] and can be seen in Figure 5.21, where three pulses are generated in less than 4 μs, resulting in an IEC overlapped measurement.

Overall, the sensors show an average error of around 30% for the high magnitude PD and about 1 pC difference in the low charge PD defects. The corona and SD low magnitude increase the measurement error; however, the IEC ±1 pC requirement keeps the measurement inside the tolerance. When the two sensors are combined, the measured reflections decrease, and the uncertainty improves, especially in the S2 location, where the sensors are affected by the T-section discontinuity.

Table 5.4 Uncertainty results for TUDelft full-scale GIS, [87].

			IEC/HFCT		MS/HFCT		ES/HFCT		Syn/HFCT	
			μ [%]	σ [%]	μ [%]	σ [%]	μ [%]	σ [%]	μ [%]	σ [%]
Jumping Particle	AC	S2	13	2	-42	3	-19	3	-27	2
		S1	12	6	-35	8	-45	3	-34	5
	DC+	S2	2	3	-25	2	-14	3	-12	2
		S1	4	3	-18	2	-25	2	-13	2
	DC-	S2	3	3	-30	2	-12	2	-13	2
		S1	0	3	-16	2	-24	2	-10	2
FE	AC	S2	29	8	-25	4	-9	4	-8	4
		S1	20	27	-22	5	-24	5	-20	5
	DC-	S2	328	356	-46	23	-36	27	-35	28
		S1	240	336	-32	20	-39	18	-29	20
Corona	AC	S2	72	39	-14	55	-6	15	-19	31
		S1	86	49	-27	24	-38	13	-27	18
	DC+	S2	144	64	-16	52	-17	16	-21	29
		S1	164	83	9	86	-42	17	-32	37
	DC-	S2	81	61	9	94	-17	21	-29	28
		S1	71	36	-24	31	-34	12	-28	19
SD	AC	S2	-2	33	-34	22	-29	13	-31	14
		S1	-11	27	-43	15	-38	11	-37	13

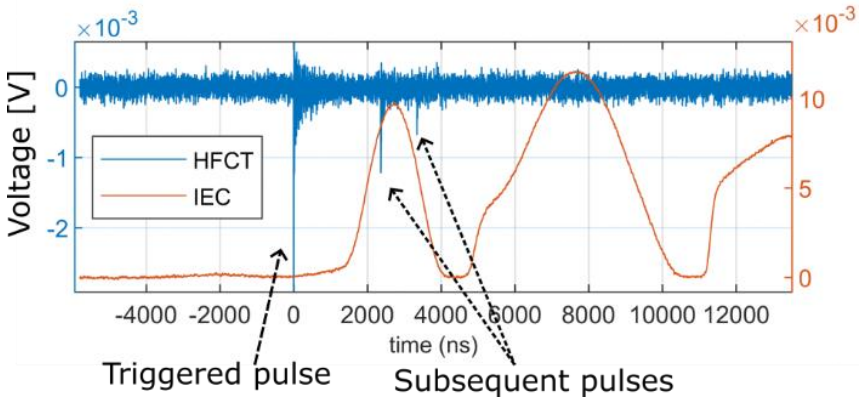

Figure 5.21 Corona discharge waveshapes for the HFCT and the IEC method, [87].

LCOE

Table 5.5 shows the HV test results performed in the LCOE high-voltage setup, where 200 pulses of each defect were recorded and analysed. Both sensors show an error below 30%, except for the protrusion defect, where the electric coupler's error was higher than the other defects. This is associated with the nonlinearity of the amplifiers when the charge is too low and the sensor's high capacitance input. In general, the errors were lower when the sensors were combined.

Table 5.5 Uncertainty results for LCOE full-scale GIS, [87].

		MS/IEC		ES/IEC		Syn/IEC	
		μ (%)	σ (%)	μ (%)	σ (%)	μ (%)	σ (%)
SD	AC	-32	9	-10	10	6	12
FE	AC	-15	5	20	6	-1	5
	DC+	18	5	23	4	-5	4
	DC-	15	8	15	5	-8	5
JP	AC	-28	22	-12	38	-7	31
	DC+	-15	21	2	25	-25	33
	DC-	-18	26	5	27	14	47
Cor	AC	-19	17	-76	8	-19	16

SGI

The tests performed at SuperGrid Institute gave the results presented in Table 5.6. First, tests were performed with a protrusion under DC- and without noise. Second, the JP tests were performed under DC- without and with two different noises, where N1 is the sinewave noise, and N2 is the white noise. Four thousand pulses were recorded for each configuration to have several amplitudes of discharges and for statistical analysis. The reference signal to evaluate the calibration was the HFCT or the conventional IEC system. Similar results to the other laboratories were obtained.

Table 5.6 Uncertainty results for SGI full-scale GIS, [87].

				MS		ES	
Defect	Source	Ref.	Noise	μ (%)	σ (%)	μ (%)	σ (%)
Corona	DC-	HFCT	No Noise	-20	23	-8	19
JP	DC-	IEC	No Noise	6	69	-7	31
JP	DC-	IEC	N1	17	23	-10	28
JP	DC-	IEC	N2	18	23	-1	27

5.3. Chapter Conclusions

GIS maintenance and installation costs demand reliable online electric insulation monitoring. Present PD measuring systems sense the PD without measuring a calibrated charge that can assess the defect severity. The presented chapter proposed a calibration procedure for PD charge estimation using the voltage-double-integration method. It is shown that the calibration constants can be found in a full-scale GIS by applying sinusoidal signals in the low-medium frequency range (50-500 kHz). The method is extended to derivative electromagnetic sensors, namely magnetic and electric couplers.

The calibration process can estimate the PD charge in GIS with a reasonable error. The method's uncertainty evaluated in the low-voltage testbench gave slightly different values in the linearity, SNR, and pulse width test, with a mean error of around 10%. The proposed method was also tested in three full-scale GIS laboratory setups, having an average error of about 30%. These errors are above IEC PD tolerances. However, no other online method currently can estimate PD charges in GIS. The main uncertainty of the proposed system originates from the background noise. Therefore, noise reduction techniques must be investigated in order to improve the system's performance.

With further investigation, this system is expected to compare online measurements with IEC 60270 laboratory tests. The result of this study opens the possibility of measuring PD charge magnitudes with unconventional electric methods, enabling better GIS insulation monitoring and normalizing a value for different measuring systems.

6

"If someone separated the art of counting and measuring and weighing from all the other arts, what was left of each (of the others) would be, so to speak, insignificant".

- Plato

6. Interference Discrimination*

The correct identification of partial discharges is instrumental for the maintenance plan in gas-insulated systems. However, onsite PD measurements are complicated, especially in HVDC systems, where partial discharges can be identified as interference. This chapter proposes a method for discerning PDs from interferences by calculating the GIS characteristic impedance using the combination of electric and magnetic sensors.

The characteristic impedance is calculated using four approaches based on the PD charge magnitude, peak value, peak-to-peak value, and frequency spectrum. The method is first tested with a PD calibrator in a matched and open-circuited GIS testbench. Then, the identification of PDs and interference is tested in a full-scale GIS, where the measurements are subjected to pulse overlapping and noise. Five types of interference and PDs were injected into the GIS at two positions and measured in multiple mounting holes. The results show that all four approaches can precisely calculate the characteristic impedance in a matched testbench. In the full-scale GIS, these approaches show more deviation, with the peak-based approach being the most accurate.

The preceding approaches proved to work, but they all required the previous estimation of sensors' parameters. In practice, it is difficult to obtain these values, especially

* This chapter is based on the following publications:

- C. Mier Escurra, A. Rodrigo Mor, T. Luo, and P. Vaessen, "Partial Discharge and Interference Discrimination in Gas-Insulated Systems using Electric and Magnetic Sensors," International Journal of Electrical Power & Energy Systems, vol. 158, no. January, p. 109911, 2024, doi: 10.1016/j.ijepes.2024.109911.
- [Accepted], C. Mier Escurra, A. Rodrigo Mor, and P. Vaessen, "PARTIAL DISCHARGE POWER FLOW IN GAS-INSULATED SUBSTATIONS USING MAGNETIC AND ELECTRIC ANTENNAS," in International Symposium on High Voltage Engineering, 2023

when measuring at high frequencies. Therefore, a pragmatic application of the method is demonstrated using a calibrator in the full-scale GIS.

The proposed methods contribute to a more reliable PD monitoring system for HVDC/AC GIS and allow better maintenance planning, reducing unnecessary costs, notably for offshore substations.

6.1. PD and Interference Propagation in Gas-Insulated Systems

Partial discharge measurements are complex in onsite substations where external noise (interference) is coupled. That is one of the reasons that [11] proposes unconventional PD measurement methods, with UHF antennas offering high noise rejection due to their operational frequency. However, interferences are coupled even at this frequency range, leading to false positive PD identification [25]. Therefore, discrimination of interference in online PD measurements is of interest and is critical for maintenance programs in remote places, such as offshore gas-insulated systems. For instance, a false positive PD in offshore GIS leads to unnecessary and costly maintenance operations that could be avoided with better discrimination of real PDs and noise.

Partial discharges can be identified from interferences by software and hardware methods. Machine learning is a software method that has been gaining popularity recently. Machine learning uses clusters based on the PD characteristics [89], [45], [46], making it a powerful tool for not only filtering PDs from interference but also for classifying them. However, machine learning requires a massive database from previous discharges and many samples to correlate them with this database. On the other hand, hardware methods do not require a pre-learning condition. The most recognized hardware method is the phase-resolve partial discharge method [43]. This method has proved very effective but requires an experienced technician and only applies to AC systems. Another hardware method in GIS is the discrimination of interference by an external antenna [90], with the inconvenience of encompassing a short GIS length with multiple antennas. For these reasons, a proposal for PD and noise discrimination is presented in this thesis, based on the calculation of a physical parameter, the GIS characteristic impedance.

6.1.1. Magnetic and Electric Sensors Relation in the TEM Mode

As explained in section 2.2.1, when PDs occur in a single-phase GIS, electromagnetic energy propagates as a coaxial waveguide in 3 modes, depending on the frequency and the GIS geometry. The transverse electric and transverse magnetic modes only exist above certain cut-off frequencies, usually above the VHF range for GIS geometries. On the other hand, the transverse electromagnetic mode propagates in all the frequency spectrum.

Figure 6.1 shows a representation of the TEM propagation in a GIS, where the top half is represented by wave parameters and the bottom by voltage and current. The electric and

magnetic fields in the TEM mode in a lossless media are related by the wave impedance $\eta = \sqrt{\mu/\varepsilon}$, as shown in (6.1), where μ and ε are the permeability and permittivity of the medium, $\boldsymbol{E}_\rho$ is the electric field in the radial direction, and $\boldsymbol{H}_\varphi$ is the magnetic field in the angular direction. The voltage ($\boldsymbol{V}$) and current ($\boldsymbol{I}$) can be found from the wave parameters using (6.2), where a and b are the GIS inner and outer conductor radii, r is the radial dimension, and l is the coaxial contour. Both the voltage and current ratio equal the characteristic impedance (Z_0), which is a physical constant that depends on the medium materials and geometry (6.3). Therefore, the characteristic impedance can be estimated by measuring the voltage and current with the corresponding sensors.

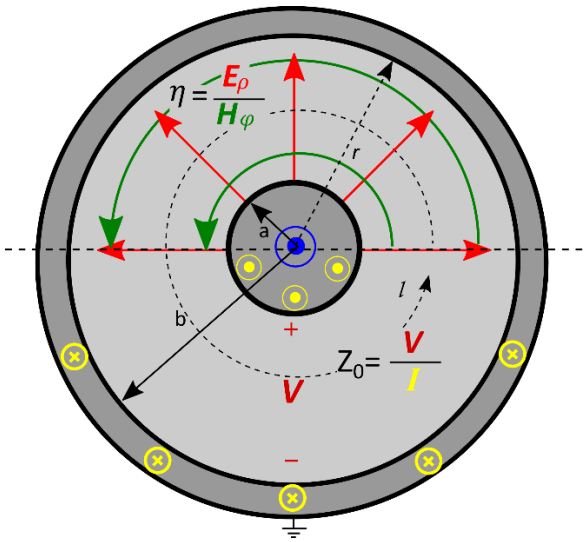

Figure 6.1 TEM propagation in a GIS represented by wave parameters in the top half, and circuit parameters in the bottom half. The red arrows represent the electric field, the green arrows are the magnetic fields, the blue dot is the direction of propagation, and the yellow dots and crosses are current, [34].

$$\frac{\boldsymbol{E}_\rho}{\boldsymbol{H}_\varphi} = \eta \tag{6.1}$$

$$\boldsymbol{V} = \int_a^b \boldsymbol{E}_\rho(r)dr \;\; and \;\; \boldsymbol{I} = \oint_0^{2\pi r} \boldsymbol{H}_\varphi(r)dl \tag{6.2}$$

$$\frac{\boldsymbol{V}}{\boldsymbol{I}} = Z_0 = \frac{\eta}{2\pi} ln(b/a) \tag{6.3}$$

Section 4.2.2 showed the transformation filter for the electric and magnetic sensors, relating the output voltage with the input PD current. Instead, if the electric transfer function relates the output voltage with the PD voltage, the function $\alpha'_{e/m}$ results in (6.4). Since the electric sensor measures the PD voltage and the magnetic sensor the PD current, the electric and scaled magnetic sensor outputs' quotient results in the GIS "local" characteristic impedance, as shown in (6.5). A GIS comprises multiple sections with different characteristic impedances, so the "local" Z_0 corresponds to the characteristic impedance at the sensors' location. Equation (6.5) demonstrates that the estimated ratio of TEM coaxial waves equals

Z_0, and any other signal measured out of this mode gives a different value. This fact, based on the physics of the propagation of a pulse in a coaxial structure, paves the way for PD and external interference recognition.

$$\boldsymbol{\alpha'}_{e/m}(s) = \frac{\boldsymbol{V}_{oe}(s)/\boldsymbol{V}_{pd}(s)}{\boldsymbol{V}_{om}(s)/\boldsymbol{I}_{pd}(s)} = \frac{\boldsymbol{H}_e(s)}{\boldsymbol{H}_m(s)} = \frac{C_1 R\left({}^{sL}/_{R} + 1\right)}{M(sRC_2 + 1)} \tag{6.4}$$

$$Z_0 = \frac{\boldsymbol{V}_{pd}(s)}{\boldsymbol{I}_{pd}(s)} = \frac{\boldsymbol{V}_{eo}(s)/\boldsymbol{H}_e(s)}{\boldsymbol{V}_{mo}(s)/\boldsymbol{H}_m(s)} = \frac{\boldsymbol{V}_{eo}(s)}{\boldsymbol{V}_{mo}(s)\boldsymbol{\alpha'}_{e/m}(s)} \tag{6.5}$$

6.1.2. Interference in a GIS

GIS are subjected to numerous transients and external interference. This interference can be classified by the frequency content and duration [91]. The low-frequency transients are far from the PD sensors' bandwidth and are merely seen as a DC offset with a typical PD acquisition time in the range of microseconds. On the other hand, higher-frequency impulse transients can be misidentified with partial discharges. The influence of these interferences on PD monitoring depends on the measuring system bandwidth and the relative magnitude of the PD and interference.

In this chapter, the interferences are classified as conducted and external radiated interferences. The first ones originate in the power line and enter the GIS in the TEM mode. These interferences include the ones created by converters switching, corona discharges in the line, load switching, etc. The conducted interferences can be recognized by their propagation direction towards the GIS [25], [92], as shown in Figure 6.2. However, in the case of external radiated interference, the signal can arrive from any direction. Therefore, our focus is on externally coupled interferences, such as the ones produced by radio communication, external electrostatic discharges, EM fields induced by near circuits, etc. Some examples of both interference channels are shown in Figure 6.2.

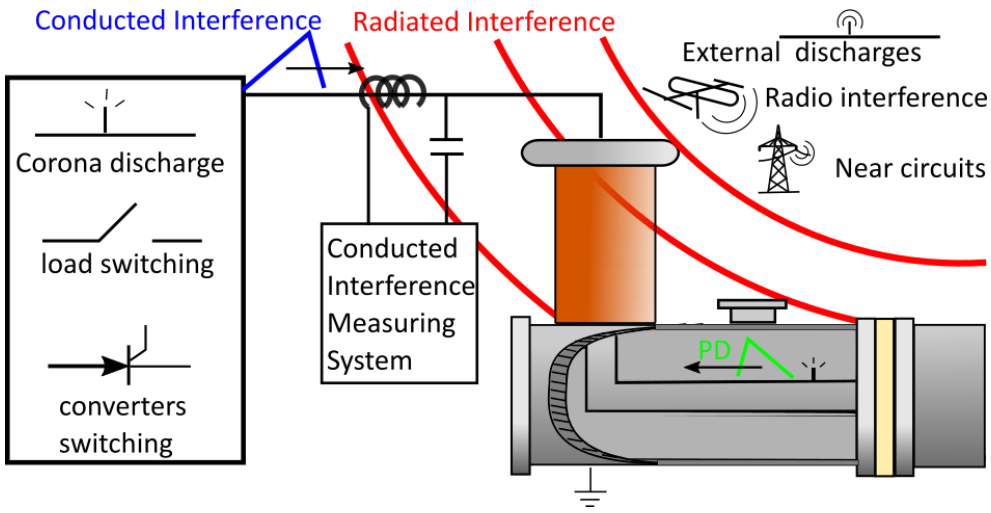

Figure 6.2 Propagation of partial discharges and conducted and external interferences, [34].

The sensors' transfer functions ratio in (6.4) is unique to the TEM mode. External interferences are not coupled to the GIS as a coaxial waveguide, resulting in different TFs for the sensors. Hence, the electric and magnetic ratio of external interference differs from those sensed in the coaxial TEM. The characteristic impedance calculated with the interference measurement leads to a value different from that of the GIS. Thus, it can be filtered out.

6.2. The Characteristic Impedance Method

6.2.1. Characteristic Impedance Calculation

The characteristic impedance is calculated using the ratio of the electric and magnetic sensors' measurements. Since the characteristic impedance is a division of the electric component over the magnetic one, the quotient is not altered if the numerator and denominator are equally manipulated. The characteristic impedance is calculated using the following approaches: charge approach, peak approach, peak-peak approach and frequency approach. This thesis is confined to these four approaches, but any other electrical parameter can be used to calculate this quotient.

Charge approach

The charge is an electrical parameter of a pulse that is not attenuated with frequency, rendering it a good candidate for calculating the GIS characteristic impedance and thus identifying PDs from interference. Section 5.1.1 showed that the charge can be estimated using the voltage-double-integration method (6.6). By examining (6.6), it is noted that the coupling constant links the output voltage with the derivative of the PD current. This is the case of the magnetic sensor, where k equals $M\ [\Omega s]$. On the contrary, the electric sensor's coupling constant associates the output voltage with the PD voltage derivative. Therefore, to estimate the PD charge using the electric sensor, the PD current is found by multiplying the coupling constant times the characteristic impedance, as shown in (3.27), section 3.3, resulting in k equal to $C_1 \cdot R \cdot Z_0$. Thus, the characteristic impedance results from dividing the electric and magnetic sensors' V2I method, as shown in (6.7).

$$Q \approx \frac{1}{k} \int_0^{t_0} \int_0^{t_0} V_o(t) dt dt \tag{6.6}$$

$$\frac{M \int_0^{t_0} \int_0^{t_0} V_{eo}(t) dt dt}{C_1 R \int_0^{t_0} \int_0^{t_0} V_{mo}(t) dt dt} \approx \frac{Q_e Z_0}{Q_m} \approx Z_0 \tag{6.7}$$

This approach only requires the sensors' coupling constants and load (R) and does not rely on other electric parameters and the accuracy of the sensors' models. Nevertheless, this method is susceptible to noise and offset. Although the white noise should converge to zero as the pulse is integrated, the shift of the integration limits affects the measurements. The offset noise is the most critical since it is accumulated quadratically by the double integral.

The long integration time also affects the charge estimation due to the overlap of pulse reflections.

Peak approach

Another approach is calculating the characteristic impedance with the electric and magnetic sensors' peak ratio. If a Dirac delta pulse with *Q* charge is measured with the sensors with a 1st-order LPF, then the time-domain output voltage results in (6.8), where β equals Z_0 for the electric sensor and 1 for the magnetic sensor. By evaluating (6.8) for the magnetic and electric sensors' peak voltage, the ratio results in (6.9). If the electric and magnetic sensors have the same parameters by scaling with (6.4), then the ratio effectively equals the characteristic impedance (6.10). Unlike the charge method, the peaks depend on the self-inductance, the ground capacitance, and other high-frequency parasitic elements. Therefore, the measurement output must be processed with a high-order LPF to avoid additional errors due to the disparity of the sensors.

$$V_o(t) = \frac{Q\beta k\omega_0\omega_f}{\omega_0 - \omega_f}\left(\omega_0 e^{-\omega_0 t} - \omega_f e^{-\omega_f t}\right) \tag{6.8}$$

$$\frac{V_{e-peak}}{V_{m-peak}} = \frac{Z_0 C_1 L}{MRC_2} \tag{6.9}$$

$$\frac{V_{e-peak}}{\alpha'_{e/m} V_{m-peak}} = Z_0 \tag{6.10}$$

In addition to the sensors' high-frequency variation, the pulse peak is sensitive to the instrument's resolution and offset. The measured peak value of a pulse changes when the time resolution is not big enough. Therefore, data acquisition must have the highest sampling rate, which adds additional cost to the equipment. The quantization error becomes important for low-resolution equipment. Equation (6.11) shows the quantization error, ε, where *a* is the ratio between the measurement vertical scale and the measured pulse peak, and *n* is the number of bits. The number 2 at the numerator corresponds to the worst case when one sensor rounds up and the other rounds down the quantization level. PD magnitude variation leads to overscaling the vertical scale to avoid clipping. So, with a peak value four times smaller than the vertical scale and with an 8-bit resolution, the error can be as high as 1.6%. A more significant error source is the offset that can shift the peak value.

$$\varepsilon \leq \frac{2}{a2^{n+1}} \tag{6.11}$$

Peak-Peak approach

The narrow-band response of the sensors results in a pulse with a huge undershoot [56]. This peak-to-peak value eliminates the measured offset and is less affected by noise, since it has a larger signal-to-noise ratio. However, the undershoots peak requires more measuring time, where a reflection may overlap. Like the incident peak method, the peak-to-

peak depends on all the sensors' parameters. Since this method requires two quantities for each sensor, the vertical resolution quantization error can be twice that of the previous approach.

Frequency approach

Another way to find the characteristic impedance is by evaluating the sensors' frequency response ratio in (6.5). The evaluation of a single frequency becomes too sensitive to noise, so we propose integrating the absolute value in a frequency range (f_1 to f_2), resulting in (6.12). The white noise has a normal distribution, meaning that its integration in the time or frequency domain approximates zero. Additionally, the low-frequency noises, responsible for the offset error, can be rejected by increasing the lower-integration limit. This method shows the highest noise immunity; however, the estimation of the characteristic impedance depends on the sensor's scalation and the frequency range.

$$\frac{\int_{f_1}^{f_2} |\boldsymbol{V}_{eo}(2\pi f)| df}{\int_{f_1}^{f_2} \left|\boldsymbol{\alpha}'_{e/m}(2\pi f)\boldsymbol{V}_{mo}(2\pi f)\right| df} = Z_0 \tag{6.12}$$

When a noiseless GIS is matched, (6.12) gives the characteristic impedance irrespective of the integration limits. Nevertheless, a discontinuity near the observation point affects this calculation. The voltage and current in a GIS can be modelled with the transmission line equations (6.13) and (6.14), where z is the distance of the observation point to a discontinuity, $\boldsymbol{V}^+$ is the voltage forward propagation, and c is the speed of light. Assuming that the discontinuity is a bushing with a high impedance, the measured voltage and current with the electric and magnetic sensors can be simplified as (6.15) and (6.16), respectively. Therefore, substituting (6.15) and (6.16) into (6.12) results in Figure 6.3, where φ is the ratio of the transmission line length and the wavelength ($\varphi = 2\pi fz/c$), and $Z(\varphi)$ is the estimated characteristic impedance. Two conclusions can be extracted from this result:

- The wider the integration limits are, the better $Z(\varphi)$ approaches Z_0.
- If the discontinuity is too close to the measuring point, $Z(\varphi)$ takes longer to converge.

Hence, the best results are obtained by covering a wide frequency range. Nevertheless, at a higher frequency, the electric and magnetic sensors' models deviate.

$$\boldsymbol{V} = \boldsymbol{V}^+\left(e^{-\frac{j2\pi fz}{c}} + \tau e^{\frac{j2\pi fz}{c}}\right) \tag{6.13}$$

$$\boldsymbol{I} = \frac{\boldsymbol{V}^+}{Z_0}\left(e^{-\frac{j2\pi fz}{c}} - \tau e^{\frac{j2\pi fz}{c}}\right) \tag{6.14}$$

$$\boldsymbol{V}_{eo} = 2\boldsymbol{H}_e\boldsymbol{V}^+\cos\left(\frac{2\pi fz}{c}\right) \tag{6.15}$$

$$\boldsymbol{V}_{mo} = \frac{-j2\boldsymbol{H}_m\boldsymbol{V}^+}{Z_0} sin\left(\frac{2\pi f z}{c}\right) \tag{6.16}$$

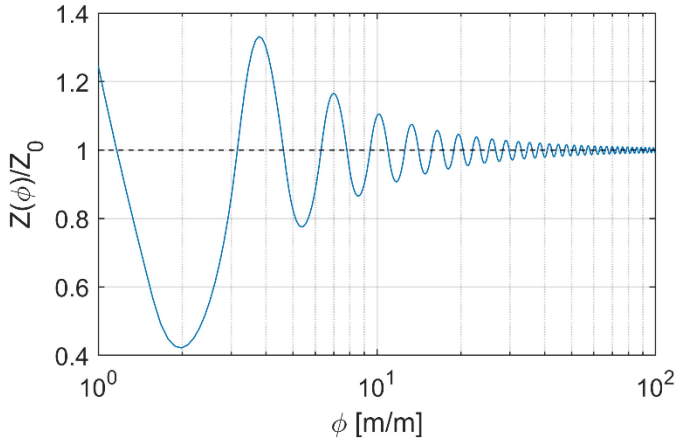

Figure 6.3. Characteristic impedance approximation as the discontinuity distance and wavelength ratio increases, [34].

Summary

Four approaches to calculate the local characteristic impedance were presented. Each one uses a different parameter of the measured pulse, leading to the advantages (green) and disadvantages (red) shown in Table 6.1. The error sources mainly depend on the signal-to-noise ratio, the relative distance of the sensors to the discontinuities, and the deviation of the sensors' models. Figure 6.4 exemplifies the different pulse times required for each method, which affect the result due to the pulse overlapping.

Table 6.1. Advantages and disadvantages of the four approaches to calculate the characteristic impedance.

	Charge	Peak	Peak-peak	Frequency
Sensors' parameters	Calibration constant	All parameters	All parameters	All parameters
White noise	Heavily affected	StdDev affected	StdDev affected	Less affected
Offset noise	Heavily affected	Affected linearly	Not affected	Slightly affected
Reflections	Heavily affected	Less affected	Affected	Heavily affected
Resolution	Slightly affected	More affected	More affected	Less affected
Frequency content	Not affected	Affected	Affected	Highly affected

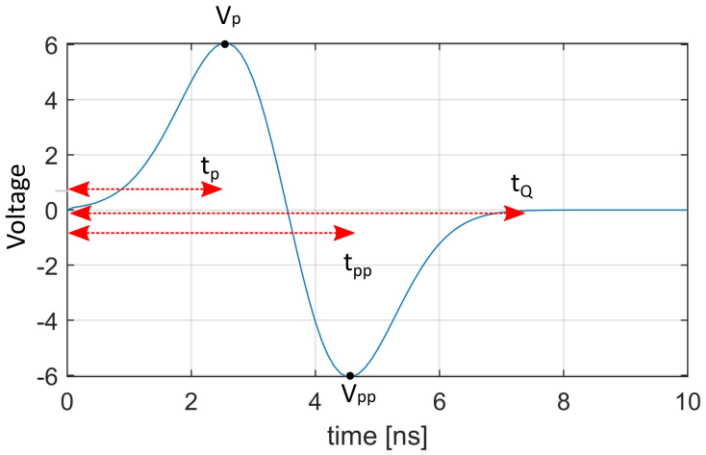

Figure 6.4. Pulse times required for the peak method (t_p), peak-peak method (t_{pp}), and charge method (t_Q) , [34].

6.2.2. Test setups

The proposed methods are investigated using the matched testbench and the full-scale GIS. On the one hand, the matched testbench evaluates an ideal situation with low noise and without reflections. On the other hand, the full-scale GIS setup is subjected to multiple discontinuities and noise, giving different errors for each discrimination method. In both test setups, the electric and magnetic sensors share a common mounting hole.

The sensor

The electromagnetic field can be measured by placing both sensors in the same transversal position, either by different mounting holes or sharing the same one. The last option has the advantage that only one mounting hole is required. Still, in these experiments, the reason for choosing a single hole is to demonstrate that the interference is induced differently in the electric and magnetic couplers, even when placed in the same location. Therefore, the sensor used is the one presented in Figure 4.10, where each sensor has its output and can be combined with the software synergy method.

Matched testbench

To prove that the electric and magnetic sensors' ratio is the characteristic impedance, the testbench in section 3.1. was used. The characteristic impedance estimation approaches were tested in a fully-matched 50 Ω setup and then with an open termination. In the open-circuit case, the pulse is reflected, affecting the measured characteristic impedance.

Full-scale GIS

The discrimination between PD pulses and interference is tested in the full-scale GIS illustrated in the appendix.

Unlike the TEM chamber, the full-scale GIS comprises multiple discontinuities, such as spacers, disconnectors, T-sections, bushings, etc., which cause reflections. In addition to the reflections, the small PD magnitude results in measurements with lower SNR. In this test, the PDs and the interferences were measured in two locations in the GIS. In position 2, the sensors were located next to a T-section, where 1/3 of the propagated wave is reflected. In position 3,

the sensors are distanced from any discontinuity, assimilating a gas-insulated line. The defects were also introduced in the two PD locations with different propagation paths to the sensors.

The PD defects used in this research were a floating electrode, jumping/moving particle, Cavity discharge (Ca), surface discharge and protrusion, each having a different discharge mechanism. In addition to the defects, a Fast-Pulse calibrator (FP) was also used. These defects were placed in both positions for each sensor's locations to measure both PD directions. The corona and surface discharges were omitted for the defect opposite the sensors because the signal is lost with the attenuation along the GIS. For both sensors' locations, different interferences were injected.

Five interferences were coupled to the GIS and measured with the sensors. A current loop between the laboratory ground mesh and the GIS enclosure was injected with a fast-pulse calibrator (E2Gn), inducing a magnetic field and a potential difference in the sensors' mounting hole. Electromagnetic fields were generated with a log-periodic antenna fed with a Haefely USG 40 generator (TV) and a floating electrode discharged in the laboratory ground mesh (FEEM), inducing noise in the sensors' coaxial cables connected to the GIS structure [93]. Another interference source was an external floating electrode discharged in the enclosure of the GIS (FEE). The last interference was an external magnetic field produced by a nearby motor fed with a variable frequency driver (motor). Since none of these interferences are coupled to the sensors in the coaxial TEM mode, the ratio is expected to result in a distinct value from the GIS characteristic impedance.

Measuring system

Figure 6.5 illustrates the measuring system used for the testbench and the full-scale GIS. The sensors' outputs were connected to amplifiers depending on the signal intensity. For the corona discharge, surface discharge, the calibrator pulse and all interferences, the electric and magnetic sensors were connected to 25 dB and 28.8 dB ZFL-500-1 GHz Mini-Circuits amplifiers, respectively. In the case of the testbench, 30 dB-1 GHz amplifiers were used for both sensors. Then, at the oscilloscope's input, the signal was filtered with 200 MHz and 100 MHz 8th-order LPFs for the testbench and 200 MHz and 50 MHz for the full-scale GIS. In parallel with the filters and the oscilloscope, surge arresters with a 100 MHz LPF response were used in the full-scale GIS scenario. The oscilloscope consisted of a Tektronix MSO58 with 2 GHz bandwidth and a sample rate of 6.25 GS/s.

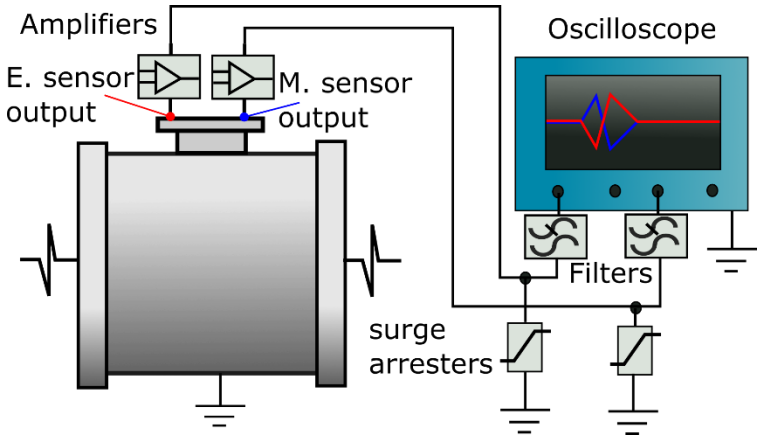

Figure 6.5. Measuring system used for the testbench and the full-scale GIS. The surge arresters were not used in the testbench, [34].

6.2.3. Results and Discussions

Matched testbench

Table 6.2 shows the testbench's calculated characteristic impedances when matched (Mat.) and open-circuited (OC). In the matched case, the results are very close to the characteristic impedance of 50 Ω. The peak, peak-peak, and frequency method results are improved with the 100 MHz filter because the sensors' parameters are better approximated at low frequencies. In the case of the charge method without discontinuities, the filter does not affect the result.

The characteristic impedance is accurately calculated if the waveguide has no discontinuities close enough to the sensors that could lead to an overlapped measurement. Different characteristic impedances are obtained for each method when the testbench is open-circuited because the overlapping increases with the pulse progression. For instance, the peak method at 200 MHz is less affected because the reflection does not reach the incident pulse peak. When the sensors are filtered with 100 MHz, the pulse is slower, and the reflection overlaps with the incident pulse peak. This extreme case of discontinuity shows its effect on the characteristic impedance calculation.

Table 6.2. Calculated characteristic impedance for a matched (Mat) and open-circuited (OC) testbench [94].

	Charge	Peak	Peak-Peak	Frequency
Mat. @200MHz	49.0 Ω	52.4 Ω	52.7 Ω	51.9 Ω
Mat. @100MHz	48.9 Ω	50.5 Ω	50.3 Ω	49.4 Ω
OC @200MHz	61.7 Ω	52.6 Ω	22.4 Ω	35.2 Ω
OC @100MHz	46.1 Ω	60.2 Ω	33.9 Ω	33.1 Ω

Full-scale GIS

In the previous test setup, the characteristic impedance was calculated to show the testbench's 50 Ω. In the full-scale GIS, the geometry changes in every section, giving a different local characteristic impedance. Hence, it is more convenient to normalize the sensors' ratio. For that, the electric sensor's coupling factor must be multiplied by the local characteristic

impedance, which is known in advance with the GIS geometry (6.3). With this normalization, the sensors' ratios of TEM signals are expected to approximate to one.

Figure 6.6 shows the cluster of 1700 samples of the magnetic and electric outputs, including all types of PDs and interferences. The cluster corresponds to the peak's approach when the sensors are in location 3 with the 200 MHz LPF and the defect at location 2. In this result, the PDs are close to the unit slope, and the interferences give a different ratio. When the SNR decreases, the results have more dispersion for each type of signal. As the signal magnitude decreases in Figure 6.6, the electric and magnetic measurements lose the linearity between them. This clear clustering is not obtained in every sensor position, discrimination method, and filtering, as shown in Figure 6.7 to Figure 6.10 and Table 6.3 to Table 6.6.

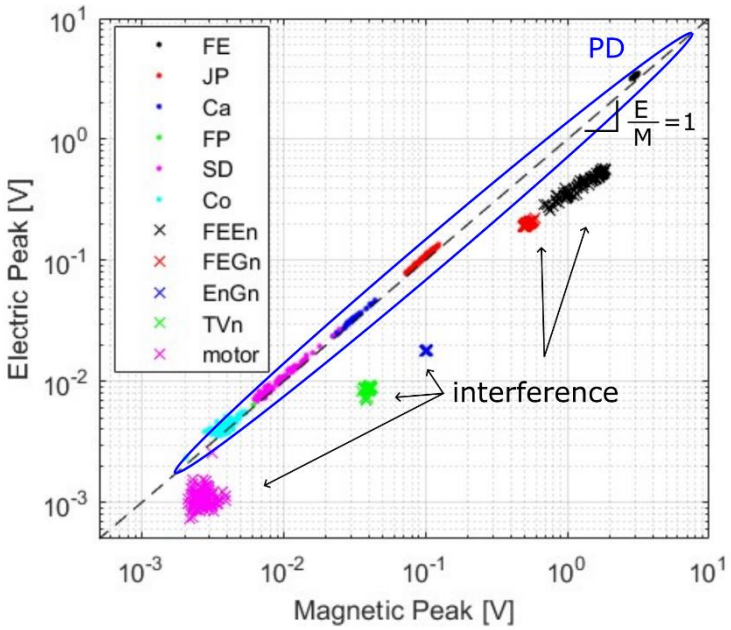

Figure 6.6. Cluster of the PDs and interferences using the peak approach in the sensors' position 3 with a 200 MHz LPF, [94].

The results are presented in four scenarios: 1) at location S2 and filtered at 200 MHz, 2) at location S2 and filtered at 50 MHz, 3) at location S3 and filtered at 200 MHz, 4) at location S3 and filtered at 50 MHz. In each situation, all the interferences ratios are compared with the PD sources in the two positions, displayed as a bar plot. The results of each approach are presented in a confusion matrix where the ratios inside the 0.8-1.2 range are considered PDs, and everything outside this range is considered interference. In this matrix, the true positives are the correct PDs, the true negatives are the correct interferences, the false negatives are incorrect PDs, and the false positives are incorrect interferences. These tables evaluate two standard deviations of each defect and interference above 5 pC (omitting corona discharge and motor interference). This 5 pC value is based on the CIGRE recommendation of the maximum allowed charge for GIS [85].

Figure 6.7 and Figure 6.8 show the results for sensors' location 2. In this position, close to a discontinuity, the incident pulse length is critical, which depends on the filter used. The PDs and interferences ratios overlap, giving a high proportion of false positives and negatives, as shown in Table 6.3 and Table 6.4. The high error is attributed to the T-section discontinuity that affects the slow pulses. The 50 MHz LPF gives longer pulses with lower magnitude, showing a worse result. Considering that it is more important to find true PDs than interferences, the Peaks' ratio gave the best results with 99% accuracy for signals above 5 pC.

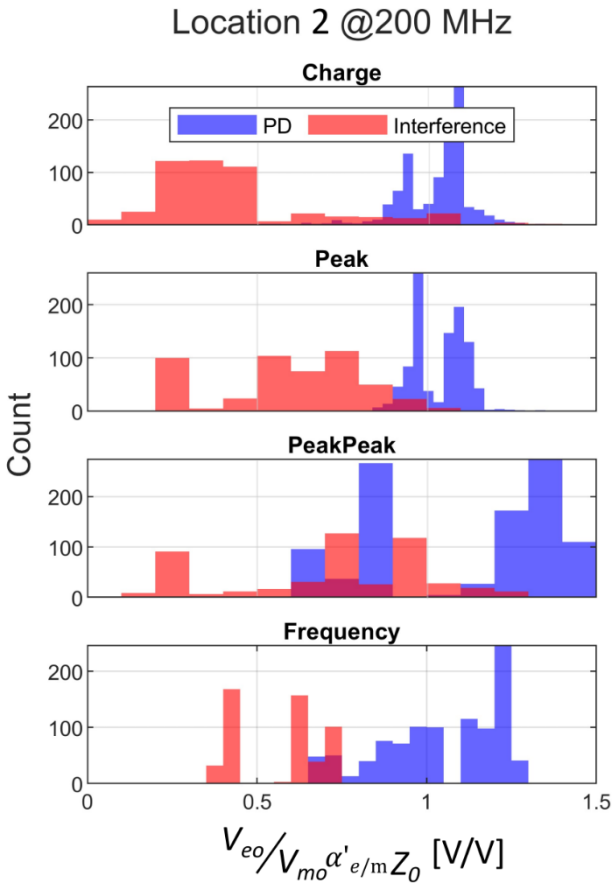

Figure 6.7. Ratios count for each approach for sensor position S2 using 200 MHz filters [94].

Table 6.3. Confusion matrix with a 0.8-1.2 threshold for the four approaches in position S2 using 200 MHz filters [94].

Loc.2 @200 MHz	Charge	Peak	Peak-peak	Frequency
True positive	95%	99%	30%	60%
False negative	5%	1%	70%	40%
True negative	90%	85%	61%	100%
False positive	10%	15%	39%	0%

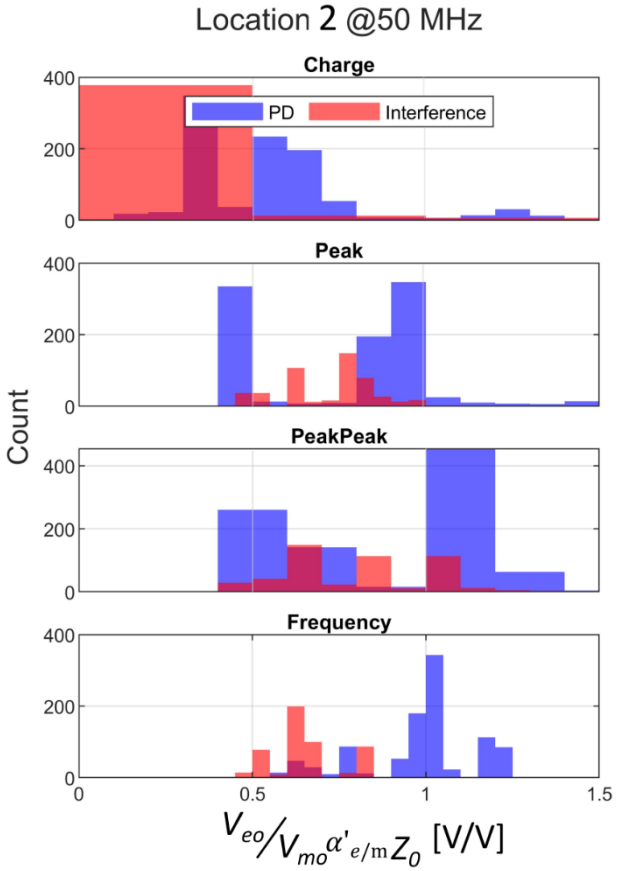

Figure 6.8. Ratios count for each approach for sensor position S2 and 50 MHz filter [94].

Table 6.4. Confusion matrix with a 0.8-1.2 threshold for the four approaches in position S2 using 50 MHz filters [94].

Loc.2 @50 MHz	Charge	Peak	Peak-peak	Frequency
True positive	3%	58%	47%	72%
False negative	97%	42%	53%	28%
True negative	99%	72%	49%	82%
False positive	1%	28%	51%	18%

The results are improved for location S3 with no discontinuities in both propagation directions, as shown in Figure 6.9, Figure 6.10, Table 6.5, and Table 6.6. In the case of the 200 MHz filter, PDs and interferences for all methods have no overlap. However, due to the short range for the PD threshold, only the Peak method is above 98%. When the 50 MHz filter is used, accuracy is lost because of the decrease in signal-to-noise ratio. According to the results, increasing the PD threshold in a GIS without discontinuities is more convenient. Still, when the sensor is close to a discontinuity, the high dispersion of PDs and interference narrows the threshold to avoid false positives.

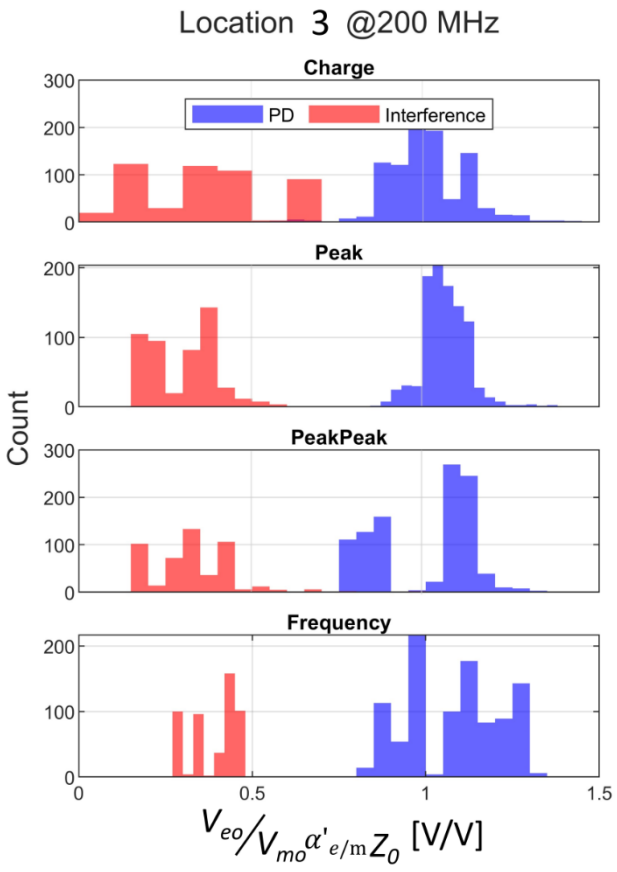

Figure 6.9. Ratios count for each approach for sensor position S3 using 200 MHz filters [94].

Table 6.5. Confusion matrix with a 0.8-1.2 threshold for the four approaches in position S3 using 200 MHz filters [94].

Loc.3 @200 MHz	Charge	Peak	Peak-peak	Frequency
True positive	94%	98%	87%	76%
False negative	6%	2%	13%	24%
True negative	100%	100%	100%	100%
False positive	0%	0%	0%	0%

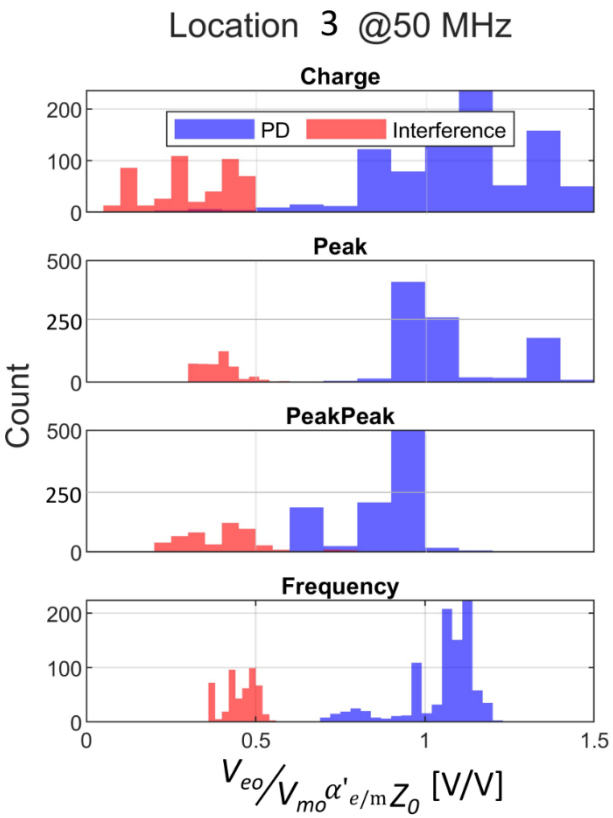

Figure 6.10. Ratios count for each approach for sensor position S3 and using 50 MHz filters [94].

Table 6.6. Confusion matrix with a 0.8-1.2 threshold for the 4 approaches in position 3 using 50 MHz filters [94].

Loc.3 @50 MHz	Charge	Peak	Peak-peak	Frequency
True positive	64%	74%	75%	93%
False negative	36%	26%	25%	7%
True negative	100%	100%	100%	100%
False positive	0%	0%	0%	0%

6.2.4. Practical Application

Regarding the practical application of the method, it is worth noticing that it works even when the sensors' parameters are unknown. In this case, the ratio of the measurements will not lead to the GIS characteristic impedance but will result in a constant ratio for all TEM propagation. This constant can be found with a calibrator injecting a signal in TEM mode. For instance, Figure 6.11 is a replica of Figure 6.6 but without scaling the sensors, assigning an arbitrary value of 1 to all parameters (M, C_1, C_2, L, Z_0, R). The slope is calculated with the calibrator's measurement and is used as the reference for the interference discrimination threshold. This is a practical application of the presented method based on the TEM propagation physics.

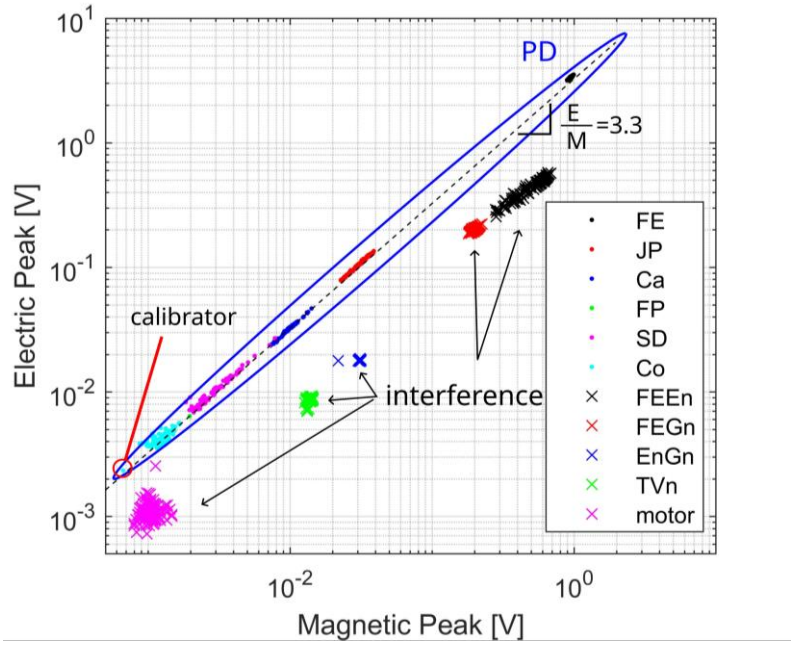

Figure 6.11 Same cluster as Figure 6.6 but without scaling the sensors, [34].

6.3. Chapter Conclusions

The presented research demonstrates that partial discharges can be discerned from external interference by measuring the GIS characteristic impedance with electric and magnetic couplers. The method is based on a physical property, invariable of any other parameters, and was validated with four different calculation approaches: charges, peaks, peak-peak, and frequency domain.

The different approaches for the proposed method can be used depending on the situation. For example, the charge method is a good option in a gas-insulated line application when the measuring system has a low bandwidth and resolution. In the case of a noisy measuring system, the frequency method offers a good solution. However, the peak method was the most versatile, having the best results in all kinds of situations.

The low-pass filter selection showed an essential influence on the results. On the one hand, a high cut-off frequency decreases the pulse overlapping and increases the SNR. On the other hand, the magnetic and electric sensors' frequency responses diverge at higher frequencies, which is more complex to predict, creating a spread of the results since each type of PD has a different response at this frequency range (>30 MHz), [95]. Overall, the interference discrimination method proved to work, but higher accuracy can be achieved by improving the sensors' design.

The following was concluded from the results:

- In a low noise and no reflection testbench, the method probes to work with an error below 5% for all approaches.

- Each approach gave different results in a full-scale GIS, depending on the pulse overlapping and the SNR.
- A calibrator can be used instead of the sensors' parameters as a practical application of the proposed method.

The method's primary error source is attributed to the inaccuracy of the sensors' models at higher frequencies. Therefore, the results can be improved with the electric and magnetic sensors' design. These findings are an essential contribution to the rapidly increasing demand for HVDC GIS, enabling the correct assessment of maintenance needs.

7

"No retreat, no surrender".

- Leonidas, *300*

7. Conclusions and Future Work

The energy transition towards decarbonization and modernization of the electric network requires the development of new technologies. Offshore windfarms, essential to this transition, rely on gas-insulated systems due to their compactness and extended lifespan. Despite the reliability of GIS, the high maintenance costs and severe consequences of power outages leave no room for failure risks. The primary source of failures in GIS is attributed to defects in electric insulation, producing partial discharges that serve as a tool for defect detection.

The current approach for standardized PD measurements proves impractical for implementation in GIS under operation. Consequently, unconventional methods have been employed, with ultra-high frequency sensors standing out. Despite the notable signal-to-noise ratio of the UHF system, it is still susceptible to interference and does not yield calibrated measurements suitable for comparison with other methods and for assessing insulation degradation. In response to these challenges, this thesis introduced a very-high frequency system capable of providing calibrated and more reliable measurements.

7.1. Research Questions

This thesis aimed to provide a calibrated, trustworthy PD measuring system based on very-high frequency sensors for gas-insulated systems. The sensors were characterized and designed for high-voltage applications with sufficient sensitivity (signal-to-noise ratio) and resolution (bandwidth) to estimate the PD charge magnitude with a minimum value of 5 pC. Additionally, a calibration process was developed for the proposed sensors. Finally, the reliability of the measuring system was improved with a method that discriminates

interference from PDs. Based on this goal, five research questions were formulated and answered.

Q1. How to model the magnetic and electric sensors, and how to improve their sensitivity, resolution, and accuracy?

The unbalanced magnetic sensor proposed in [23] successfully measured partial discharge and established a relation with the PD charge. However, this sensor was affected by common-mode currents, distorting the accuracy of the sensor. Additionally, its lumped element model constrained the sensor's characterization lower frequencies.

Chapter 3 introduces solutions to increase the sensor's measurement and model accuracy by reducing unwanted common-mode signals. The solutions involve including ferrite beads and using an "8-shaped" balanced magnetic loop. This construction rejects common-mode currents induced by external electric fields while maintaining sensitivity. Additionally, using a transmission line model, the sensor's characterization frequency range was extended from 30 MHz to 300 MHz, improving the time resolution and sensitivity. The magnetic and electric sensors and models were tested using a transverse electromagnetic testbench in the frequency and time domains.

Q2. How can the proposed magnetic sensor be adapted for HV GIS applications?

The magnetic sensors in [23] and the proposed one in Chapter 3 consist of a cable inside the GIS enclosure, enhancing the power-frequency electric field. Shielding these sensors is crucial for their application in HV GIS.

A conductive disk was proposed as a solution, resulting in an electric coupler capable of estimating the charge when measuring below the ultra-high-frequency range. Chapter 4 presented the combination of electric and magnetic couplers and investigated their interaction, leading to a high-voltage directional coupler. To reduce counter electromotive force in the magnetic loop induced by the electric coupler's Eddy currents, the electric sensor was cast with a carbon black and epoxy mixture in combination with an aluminium disk. The HV directional coupler's signal was improved using ferrite chokes in the sensor's feeder cable.

Q3. How can the charge estimation uncertainty be reduced?

One of the main sources of uncertainty in PD measurements in GIS is pulse reflections, which overlap with the incident pulse and distort the estimated charge and the PD pulse waveshape.

Chapter 4 presents a method that discerns reflected pulses, improving waveform and charge estimation. A software method involving signal processing of electric and magnetic simultaneous measurements was proposed. Alternatively, a hardware method was developed where electromagnetic signals were measured in a single sensor, similar to a directional coupler. The combination of electric and magnetic signals was tested in a testbench and a full-

scale GIS, discerning the incident PD pulse from the reflections and improving PD charge estimation.

Q4. How to calibrate the proposed measuring system?

The purpose of a calibration is to compare a measured quantity with another homogeneous one, considered the measurement unit. To date, there is no calibrated PD measurement for online GIS.

Chapter 5 introduces a theoretical and experimental procedure to calculate a scaling factor for calibrating the measuring system using the voltage-double-integration method. It was demonstrated that the calibration constants can be determined in a full-scale GIS by applying sinusoidal signals in the low-medium frequency range (50-500 kHz). This method was extended to magnetic and electric couplers. The calibration's magnitude linearity, frequency linearity and sensitivity were evaluated in two different laboratories, yielding similar results, with noise as the primary source of error. Furthermore, the calibration procedure was tested with different PD defects under HV GIS in three European laboratories, giving estimation errors below 30%.

Q5. How can partial discharges be distinguished from interferences?

Onsite substations are susceptible to multiple interferences, leading to the false identification of partial discharges. Therefore, discriminating interference in online PD measurements is of interest and is critical for maintenance programs in remote places, such as offshore gas-insulated systems.

Chapter 6 presented a method to discern PDs from interferences based on the GIS characteristic impedance by measuring the signals of the electric and magnetic sensors. The procedure was tested with a PD calibrator in a matched and open-circuited testbench, proving its ability to determine characteristic impedance with less than 5% error. In a full-scale GIS, considering pulse overlapping and noise, the peaks approach identified 98% of the PDs. A practical application procedure was proposed using a calibrator, eliminating the necessity for complex mathematical models.

7.2. Recommendations

Based on this thesis, recommendations for future work are given in this section.

This research introduced the acquisition part of a measuring system, identifying several areas for potential research and improvement. While the proposed system operates within a theoretical framework, it is not yet ready for practical applications. The ultimate objective is for the presented measuring system to evolve into a standardized method for online PD measurements in GIS, comparable to the IEC 60270. Recommendations for improvement and future work are outlined below:

Chapter 2 illustrated the rise and fall times for air PD pulses at different pressures. According to our results, these durations were too long compared to a discharge in SF_6, concluding that VHF measuring systems are more suitable for SF_6-alternative gases. However, this outcome was not in accordance with the publication [52], so further investigation is required to understand and confirm the duration of PD pulses in air and other SF_6-alternative gases. This research is of great interest for PD measurements in gases that will replace sulphur hexafluoride.

Chapter 3 presented the design and the mathematical models of electric and magnetic sensors. The analysis was focused on the sensors, where commercial voltage amplifiers were used. Enhancing the signal conditioning of the measuring system could be possible by designing amplifiers tailored to the sensors, thereby achieving a superior signal-to-noise ratio. Additionally, while the sensors' output was fixed to a 50 Ω load, aligning with the amplifiers, coaxial cables, and measuring instruments' standard values, better results may be obtained by adjusting this value.

The magnetic loop in this research measured the magnetic field induced by the current in the GIS enclosure. Towards the end of the PhD, a new magnetic field plane generated by the current in the GIS inner conductor was identified. Despite the lack of time for further development, this idea holds the potential for superior external interference rejection compared to the magnetic probes presented in this and previous research.

The handcrafted sensors in this thesis introduced additional parasitic elements at high frequencies, resulting in more complex transfer functions than those modelled in Chapter 3. Improving the sensor's design can simplify its characterization with straightforward models that can enhance the efficacy of charge estimation and interference identification.

The voltage double integration serves as a charge estimation method for derivative sensors, applicable independently of the number of poles. However, for practical reasons, the technique is approximated by integrating up to the pulse second zero crossing. This approximation deviates from the charge estimation when using filters with different bandwidths and orders. Further research is needed to understand the impact of the filter under this approach.

The main uncertainty for the charge estimation using the V2I method was the noise. Because of the double integration, the method is highly affected by offset and random noise. Therefore, it is of interest to investigate noise mitigation techniques that do not affect the charge estimation. During the PhD, a wavelet denoising technique was used, reducing the noise but also affecting the charge estimation. Hence, different methods must be tested.

Chapter 6 outlined four approaches for calculating GIS characteristic impedance, with the peak approach demonstrating the best results. The characteristic impedance, representing the ratio of electric and magnetic measurements, offers numerous ways for its

calculation. For instance, applying the wavelet transformation to the electric and magnetic outputs could yield new parameters for estimating the characteristic impedance.

Appendix

A) TUDelft Full-Scale GIS Sketch

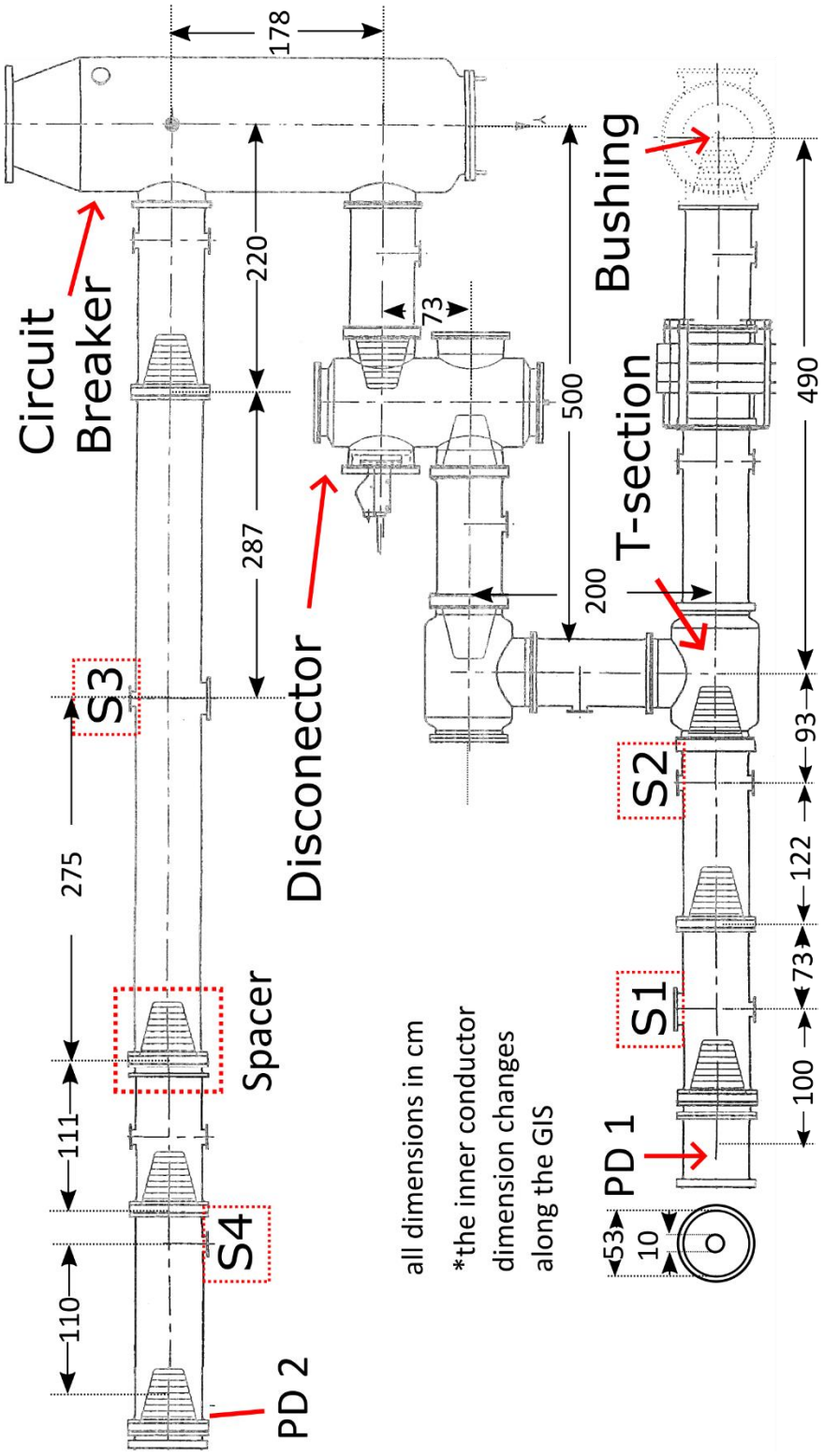

B) TUDelft Full-Scale GIS Picture

Bibliography

[1] Market and Markets, "Gas Insulated Switchgear Market." https://www.marketsandmarkets.com/Market-Reports/gas-insulated-switchgear-market-234770702.html

[2] ABB, "ABB installs latest HVDC gas-insulated switchgear innovation," *26 of September*, 2018. https://new.abb.com/news/detail/7703/abb-installs-latest-hvdc-gas-insulated-switchgear-innovation (accessed Dec. 15, 2023).

[3] A. Darwish, S. S. Refaat, H. A. Toliyat, and H. Abu-Rub, "On the Electromagnetic Wave Behavior Due to Partial Discharge in Gas Insulated Switchgears: State-of-Art Review," *IEEE Access*, vol. 7, pp. 75822–75836, 2019, doi: 10.1109/ACCESS.2019.2921089.

[4] V. Aaradhi and K. Gaidhani, "Partial discharge in Gas Insulated substations (GIS): A development and engineering perspective," *12th International Conference on Environment and Electrical Engineering, EEEIC 2013*, pp. 112–117, 2013, doi: 10.1109/EEEIC.2013.6549600.

[5] INTERNATIONAL, ELECTROTECHNICAL, and COMMISSION, *IEC 62271: High-voltage switchgear and controlgear – Part 203: AC gas-insulated metal-enclosed switchgear for rated voltages above 52 kV*, vol. 3. 2022.

[6] IEC 60270, "Partial Discharge Measurements," 2015.

[7] U. Schichler *et al.*, "UHF partial discharge detection system for GIS: Application guide for sensitivity verification: CIGRE WG D1.25," *IEEE Transactions on Dielectrics and Electrical Insulation*, vol. 23, no. 3, pp. 1313–1321, 2016, doi: 10.1109/TDEI.2015.005543.

[8] IEC, "IEC 60885-3: Test methods for partial discharge measurements on lengths of extruded power cables," 2015.

[9] A. Cavallini, G. C. Montanari, and M. Tozzi, "PD apparent charge estimation and calibration: A critical review," *IEEE Transactions on Dielectrics and Electrical Insulation*, vol. 17, no. 1, pp. 198–205, 2010, doi: 10.1109/TDEI.2010.5412018.

[10] A. P. Purnomoadi, A. Rodrigo Mor, and J. J. Smit, "Spacer flashover in Gas Insulated Switchgear (GIS) with humid SF6 under different electrical stresses," *International Journal of Electrical Power and Energy Systems*, vol. 116, no. June 2019, 2020, doi: 10.1016/j.ijepes.2019.105559.

[11] INTERNATIONAL, ELECTROTECHNICAL, and COMMISSION, *IEC 62478: High voltage test techniques – Measurement of partial discharges by electromagnetic and acoustic methods*, 1.0. International Standard, 2016.

[12] WG D1.33, "Guidelines for Unconventional Partial Discharge Measurements," *CIGRE*, pp. 1–58, 2010.

[13] G. Behrmann, S. Franz, J. Smajic, Z. Tanasic, and R. Christen, "UHF PD signal transmission in GIS: Effects of 90° bends and an L-shaped CIGRE step 1 test section," *IEEE Transactions on Dielectrics and Electrical Insulation*, vol. 26, no. 4, pp. 1293–1300, 2019, doi: 10.1109/TDEI.2019.008005.

[14] S. Ohtsuka, T. Teshima, S. Matsumoto, and M. Hikita, "Relationship between PD induced electromagnetic wave measured with UHF method and charge quantity obtained by PD current

waveform in model GIS," in *Electrical Insulation and Dielectric Phenomena*, 2006, pp. 615–618. doi: 10.1109/CEIDP.2006.312007.

[15] W. G. D1.25, "UHF partial discharge detection system for GIS: Application guide for sensitivity verification," 2016.

[16] F. Garnacho *et al.*, "Metrological Qualification of PD Analysers for Insulation Diagnosis of HVDC and HVAC Grids," *Sensors (Basel, Switzerland)*, vol. 23, no. 14, 2023, doi: 10.3390/s23146317.

[17] A. Khamlichi, F. Garnacho, C. Ffii-lcoe, F. Álvarez, J. Ortego, and E. Arcones, "Error in the measurement of partial discharge pulses according to the frequency response of HFCT sensors," pp. 242–246, 2021.

[18] A. Rodrigo Mor, L. Castro Heredia, and F. Muñoz, "A Novel Approach for Partial Discharge Measurements on GIS Using HFCT Sensors," *Sensors*, vol. 18, no. 12, p. 4482, Dec. 2018, doi: 10.3390/s18124482.

[19] A. Rodrigo Mor, "Report D15 . 3 Report on DC GIS diagnostic and monitoring tools and methods," Netherlands, 2018. doi: 10.3030/691714.

[20] A. Rodrigo Mor, L. C. Castro Heredia, and F. A. Muñoz, "A magnetic loop antenna for partial discharge measurements on GIS," *International Journal of Electrical Power and Energy Systems*, vol. 115, no. June 2019, p. 105514, 2020, doi: 10.1016/j.ijepes.2019.105514.

[21] F. Muñoz-Muñoz and A. Rodrigo-Mor, "Partial discharges and noise discrimination using magnetic antennas, the cross wavelet transform and support vector machines," *Sensors (Switzerland)*, vol. 20, no. 11, pp. 1–14, 2020, doi: 10.3390/s20113180.

[22] A.-P. Elg and E. Al, "Research Project EMPIR 19ENG02 Future Energy," in *VDE High Voltage Technology*, 2020, pp. 1–6.

[23] A. Rodrigo-Morz, F. A. Muñoz, and L. C. Castro-Heredia, "A novel antenna for partial discharge measurements in GIS based on magnetic field detection," *Sensors (Switzerland)*, vol. 19, no. 4, 2019, doi: 10.3390/s19040858.

[24] A. Ferrero and S. Salicone, "Measurement uncertainty," *IEEE Instrumentation and Measurement Magazine*, vol. 9, no. 3, pp. 44–51, 2006, doi: 10.1109/MIM.2006.1637979.

[25] G. Robles, J. M. Fresno, and J. M. Martínez-Tarifa, "Separation of radio-frequency sources and localization of partial discharges in noisy environments," *Sensors (Switzerland)*, vol. 15, no. 5, pp. 9882–9898, 2015, doi: 10.3390/s150509882.

[26] C. M. Escurra and A. R. Mor, "Test Bench and Frequency Response of a Magnetic Antenna used in GIS PD Measurements," in *2021 Electrical Insulation Conference, EIC 2021*, 2021, no. 2, pp. 269–272. doi: 10.1109/EIC49891.2021.9612372.

[27] C. Mier, A. R. Mor, and P. Vaessen, "Design and Characterization of a Magnetic Loop Antenna for Partial Discharge Measurements in Gas Insulated Substations," *IEEE Sensors Journal*, vol. 21, no. 17, pp. 18618–18625, 2021, doi: 10.1109/JSEN.2021.3089084.

[28] C. M. Escurra and A. R. Mor, "Balanced Magnetic Antenna for Partial Discharge Measurements in Gas-Insulated Substations," in *2022 9th International Conference on Condition Monitoring and Diagnosis, CMD 2022*, 2022, pp. 509–512. doi: 10.23919/CMD54214.2022.9991698.

[29] C. Mier, A. Rodrigo Mor, L. Castro, and P. Vaessen, "Magnetic and electric antennas calibration

for partial discharge charge estimation in gas-insulated substations," *International Journal of Electrical Power & Energy Systems*, vol. 141, no. January, p. 108226, 2022, doi: 10.1016/j.ijepes.2022.108226.

[30] C. Mier, A. Rodrigo Mor, P. Vaessen, and A. Lathouwers, "Magnetic and electric antennas synergy for partial discharge measurements in gas-insulated substations: Power flow and reflection suppression," *International Journal of Electrical Power and Energy Systems*, vol. 144, no. January 2023, pp. 1–9, 2023, doi: 10.1016/j.ijepes.2022.108530.

[31] C. Mier, A. Rodrigo Mor, and P. Vaessen, "A directional coupler for partial discharge measurements in gas-insulated substations," *Measurement: Journal of the International Measurement Confederation*, vol. 225, 2024, doi: 10.1016/j.measurement.2023.113996.

[32] C. Mier *et al.*, "Methods for Partial Discharge Calibration in Gas-Insulated Substations for HVDC Power Grids and Charge Evaluation Uncertainty," *IEEE Sensors Journal*, vol. 23, no. 19, pp. 23486–23493, 2023, doi: 10.1109/JSEN.2023.3302871.

[33] [Accepted] C. Mier Escurra, A. Rodrigo Mor, and P. Vaessen, "PARTIAL DISCHARGE POWER FLOW IN GAS-INSULATED SUBSTATIONS USING MAGNETIC AND ELECTRIC ANTENNAS," in International Symposium on High Voltage Engineering 2023.

[34] C. Mier, A. Rodrigo Mor, T. Luo, and P. Vaessen, "Partial discharge and interference discrimination in gas-insulated systems using electric and magnetic sensors," *International Journal of Electrical Power and Energy Systems*, vol. 158, 2024, doi: 10.1016/j.ijepes.2024.109911.

[35] S. S. Refaat and M. A. Shams, "A review of partial discharge detection, diagnosis techniques in high voltage power cables," *Proceedings - 2018 IEEE 12th International Conference on Compatibility, Power Electronics and Power Engineering, CPE-POWERENG 2018*, pp. 1–5, 2018, doi: 10.1109/CPE.2018.8372608.

[36] F. Kreuger, *Industrial High Voltage I*, Delft Univ. Delft: Delft University Press, 1992.

[37] R. Piccin, A. Mor, P. Morshuis, A. Girodet, and J. Smit, "Partial discharge analysis of gas insulated systems at high voltage AC and DC," *IEEE Transactions on Dielectrics and Electrical Insulation*, vol. 22, no. 1, pp. 218–228, 2015, doi: 10.1109/TDEI.2014.004711.

[38] C. Mier Escurra, "Characterization of a new method for partial discharges measurements in HVDC GIS," M.S. thesis, DCE&S, Delft University of Technology, Delft, 2018. [Online]. Available: http://repository.tudelft.nl/

[39] F. Alvarez, F. Garnacho, A. Ramirez, E. Arcones, P. Garcia, and C. A. Vera, "Generation of Reproducible Reference Insulation Defects in Experimental Tests Cells for Controlled PD monitoring," *ICHVE 2018 - 2018 IEEE International Conference on High Voltage Engineering and Application*, no. l, 2019, doi: 10.1109/ICHVE.2018.8641856.

[40] F. Alvarez, J. Ortego, F. Garnacho, and M. A. Sanchez-Uran, "A clustering technique for partial discharge and noise sources identification in power cables by means of waveform parameters," *IEEE Transactions on Dielectrics and Electrical Insulation*, vol. 23, no. 1, pp. 469–481, 2016, doi: 10.1109/TDEI.2015.005037.

[41] E. Arcones *et al.*, "Development, testing and aging of reference insulation defects for the improvement in partial discharges diagnosis," in *2021 Electrical Insulation Conference, EIC 2021*, 2021, pp. 273–276. doi: 10.1109/EIC49891.2021.9612350.

[42] C. Vera *et al.*, “Validation of a Qualification Procedure Applied to the Verification of Partial Discharge Analysers Used for HVDC or HVAC Networks,” *Applied Sciences (Switzerland)*, vol. 13, no. 14, 2023, doi: 10.3390/app13148214.

[43] W. G. 21.03, “Recognition of Discharges,” *CIGRE Electra*, vol. 11, pp. 61–98, 1969.

[44] S. Abdul Madhar, A. Rodrigo Mor, P. Mraz, and R. Ross, “Study of DC partial discharge on dielectric surfaces: Mechanism, patterns and similarities to AC,” *International Journal of Electrical Power and Energy Systems*, vol. 126, Mar. 2021, doi: 10.1016/j.ijepes.2020.106600.

[45] A. Cavallini, G. C. Montanari, A. Contin, and F. Puletti, “A new approach to the diagnosis of solid insulation systems based on PD signal inference,” *IEEE Electrical Insulation Magazine*, vol. 19, no. 2, pp. 23–30, 2003, doi: 10.1109/MEI.2003.1192033.

[46] J. A. Ardila-Rey, M. V. Rojas-Moreno, J. M. Martínez-Tarifa, and G. Robles, “Inductive sensor performance in partial discharges and noise separation by means of spectral power ratios,” *Sensors (Switzerland)*, vol. 14, no. 2, pp. 3408–3427, 2014, doi: 10.3390/s140203408.

[47] A. J. Reid, M. D. Judd, B. G. Stewart, and R. A. Fouracre, “Partial discharge current pulses in SF6 and the effect of superposition of their radiometric measurement,” *Journal of Physics D: Applied Physics*, vol. 39, no. 19, pp. 4167–4177, 2006, doi: 10.1088/0022-3727/39/19/008.

[48] H. Okubo, N. Hayakawa, and A. Matsushita, “The relationship between partial discharge current pulse waveforms and physical mechanisms,” *IEEE Electrical Insulation Magazine*, vol. 18, no. 3, pp. 38–45, 2002, doi: 10.1109/MEI.2002.1014966.

[49] C. Plet, D. N. V Gl, and U. Riechert, “D15 . 7 Report on PD characteristics of SF 6 alternative gases : comparison with SF 6,” no. 691714, 2020.

[50] C. M. Franck *et al.*, “Electric performance of new non-SF6 gases and gas mixtures for gas-insulated systems,” *CIGRE*, pp. 1–207, 2021.

[51] E. van Veldhuizen, C. Mier, A. Lathouwers, A. Rodrigo Mor, and M. Ghaffarian, “The effect of humidity on the AC breakdown strength of C4-FN/CO2 (5%/95%) and the partial discharge behaviour of corona under different operating conditions,” *IEEE Transactions on Dielectrics and Electrical Insulation*, pp. 1–8, 2024, doi: 10.1109/TDEI.2024.3390649.

[52] [Accepted] M. Boltze, M. Kuschel, and T. Hücker, “COMPARISON OF GIS UHF PARTIAL DISCHARGE MEASUREMENTS IN CLEAN AIR AND SF6,” in International Symposium on High Voltage Engineering 2023.

[53] M. Walter and S. Sutton, “Understanding the Implications of Partial Discharge Performance of Non-SF6 Gases,” *Cigre Electra*, no. 332, pp. 26–29, Feb. 2024.

[54] H. Wolfgang and L. Eberhard, *High-Voltage test and measuring techniques*, 2nd ed. Cham: Springer, 219AD.

[55] A. R. Mor, P. H. F. Morshuis, and J. J. Smit, “Comparison of charge estimation methods in partial discharge cable measurements,” *IEEE Transactions on Dielectrics and Electrical Insulation*, vol. 22, no. 2, pp. 657–664, 2015, doi: 10.1109/TDEI.2015.7076760.

[56] A. Rodrigo-Mor, F. A. Muñoz, and L. C. Castro-Heredia, “Principles of charge estimation methods using high-frequency current transformer sensors in partial discharge measurements,” *Sensors (Switzerland)*, vol. 20, no. 9, 2020, doi: 10.3390/s20092520.

[57] C. M. Escurra, A. R. Mor, and P. Vaessen, “IEC 60270 Calibration Uncertainty in Gas-Insulated Substations,” *2023 IEEE Electrical Insulation Conference, EIC 2023*, pp. 1–4, 2023, doi: 10.1109/EIC55835.2023.10177354.

[58] U. Iru, H. Lq, and U. Dqg, *IEEE C57.113*. IEEE, 2010.

[59] C. R. Paul, “Transmission Lines: Physical Dimensions vs. Electric Dimensions,” *Transmission Lines in Digital Systems for EMC Practitioners*, pp. 1–29, 2011, doi: 10.1002/9781118145579.ch1.

[60] N. Ida, *Engineering Electromagnetics*, 3rd ed. Akron: Springer, 2015.

[61] A. Darwish, S. S. Refaat, H. Abu-Rub, and H. A. Toliyat, “PD Signal Propagation in GIS: Ultra-High Frequency Detection-Based Modeling,” *IEEE Sensors Journal*, vol. 20, no. 16, pp. 9417–9426, 2020, doi: 10.1109/JSEN.2020.2988840.

[62] S. Meijer, "*Partial Discharge Diagnosis of High-Voltage Gas-Insulated Systems*," Ph.D. dissertation, Delft University of Technology, Delft, 2001. [Online]. Available: http://repository.tudelft.nl/

[63] M. Hikita, S. Ohtsuka, J. Wada, S. Okabe, T. Hoshino, and S. Maruyama, “Propagation properties of PD-induced electromagnetic wave in 66 kV GIS model tank with L branch structure,” *IEEE Transactions on Dielectrics and Electrical Insulation*, vol. 18, no. 5, pp. 1678–1685, 2011, doi: 10.1109/TDEI.2011.6032839.

[64] M. Hikita, S. Ohtsuka, S. Okabe, J. Wada, T. Hoshino, and S. Maruyama, “Influence of Insulating Spacer Type on Propagation Properties of PD-induced Electromagnetic Wave in GIS,” *IEEE Transactions on Dielectrics and Electrical Insulation*, vol. 17, no. 6, pp. 1731–1737, 2010, doi: 10.1109/TDEI.2010.5658223.

[65] H. Imagawa *et al.*, “PD signal propagation characteristics in GIS and its location system by frequency components comparison,” *IEEE Transactions on Power Delivery*, vol. 16, no. 4, pp. 564–570, 2001, doi: 10.1109/61.956738.

[66] R. Kurrer, "*Teilentladungsmessung im Gigaherts-Frequencbereich an SF6-isolierten Schaltanlagen,*" Ph.D. dissertation, Universität Stuttgart, Stuttgart, 1997.

[67] M. Hikita, “Fundamental principles and application of diagnosis for GIS using partial discharge measurements,” *Proceedings of the 2011 International Conference on Electrical Engineering and Informatics, ICEEI 2011*, no. July, pp. 11–16, 2011, doi: 10.1109/ICEEI.2011.6021849.

[68] W. Gao, D. Ding, D. Zhao, and W. Liu, “Propagation properties of high-frequency electromagnetic wave through typical in-field GIS structures,” *IEEE Transactions on Power Delivery*, vol. 29, no. 6, pp. 2476–2484, 2014, doi: 10.1109/TPWRD.2014.2356500.

[69] M. Hikita, S. Ohtsuka, J. Wada, S. Okabe, T. Hoshino, and S. Maruyama, “Propagation Properties of PD-induced Electromagnetic Wave in GIS Model Tank with T Branch Structure,” *IEEE Transactions on Dielectrics and Electrical Insulation*, vol. 18, no. 5, pp. 1678–1685, 2011, doi: 10.1109/TDEI.2011.6032839.

[70] M. Hikita, S. Ohtsuka, S. Okabe, J. Wada, T. Hoshino, and S. Maruyama, “Influence of disconnecting part on propagation properties of PD-induced electromagnetic wave in model GIS,” *IEEE Transactions on Dielectrics and Electrical Insulation*, vol. 17, no. 6, pp. 1731–1737, 2010, doi: 10.1109/TDEI.2010.5658223.

[71] C. Mier and A. Rodrigo-Mor, “Dataset for publication: Test Bench and Frequency Response of a

Magnetic Antenna used in GIS PD Measurements." Zenodo.

[72] M. Ishii and K. Komiyama, "Impedance method for a shielded standard loop antenna," *IEEE Transactions on Instrumentation and Measurement*, vol. 56, no. 2, pp. 422–425, 2007, doi: 10.1109/TIM.2007.890794.

[73] L. L. Libby, "Special Aspects of Balanced Shielded Loops," *Proceedings of the IEEE*, vol. 34, no. 9, pp. 641–646, 1946.

[74] L. V. Vasenkov and V. A. Tishchenko, "Design of a shielded loop antenna," *Measurement Techniques*, vol. 31, no. 8, pp. 796–798, 1988, doi: 10.1007/BF00863499.

[75] C. Mier, A. Rodrigo-Mor, and P. Vaessen, "Dataset for publication: Design and Characterization of a Magnetic Loop Antenna for Partial Discharge Measurements in Gas Insulated Substations." Zenodo. doi: 10.5281/zenodo.5913233.

[76] C. F. M. Carobbi and L. M. Millanta, "Analysis of the Common-Mode Rejection in the Measurement and Generation of Magnetic Fields Using Loop Probes," *IEEE Transactions on Instrumentation and Measurement*, vol. 53, no. 2, pp. 514–523, 2004, doi: 10.1109/TIM.2004.823297.

[77] C. Mier, "Data Set: Balanced Magnetic Antenna for Partial Discharge Measurements in Gas-Insulated Substations." Zenodo. doi: 10.5281/zenodo.7503775.

[78] C. Mier, "Mag&ElecSynergy." Mendeley Data, V1. doi: 10.17632/4rtnmg28y2.1.

[79] S. M. Mousavi, S. A. Mirtaheri, M. A. Khosravani-Moghaddam, B. Habibi, and J. S. Meiguni, "Design, fabrication and test of a broadband high directivity directional coupler," *ICEE 2015 - Proceedings of the 23rd Iranian Conference on Electrical Engineering*, vol. 10, pp. 168–170, 2015, doi: 10.1109/IranianCEE.2015.7146203.

[80] C. Mier, "GISDicCoup." Mendeley Data, V1, 2022. doi: 10.17632/dfr5h8rhns.1.

[81] JCGM 2008:100, "Evaluation of measurement data — Guide to the expression of uncertainty in measurement," *International Organization for Standardization Geneva ISBN*, no. September. p. 134, 2008.

[82] C. Mier, "Mag&ElecCalibration." Mendeley Data, V1, 2022. doi: 10.17632/837wftgxzv.1.

[83] C. Mier Escurra, "Software for calculating partial discharge charge." Delft, 2023. doi: 10.5281/zenodo.7803040.

[84] M. Hikita, S. Ohtsuka, T. Teshima, S. Okabe, and S. Kaneko, "Electromagnetic (EM) wave characteristics in GIS and measuring the em wave leakage at the spacer aperture for partial discharge diagnosis," *IEEE Transactions on Dielectrics and Electrical Insulation*, vol. 14, no. 2, pp. 453–460, 2007, doi: 10.1109/TDEI.2007.344624.

[85] W. Boeck, W. Buesch, and E. Colombo, "Insulation Co-ordination of GIS: return of experience, on site tests and diagnostic techniques," 1998.

[86] S. Abdul Madhar, P. Mraz, A. Rodrigo Mor, and R. Ross, "Physical interpretation of the floating electrode defect patterns under AC and DC stress conditions," *International Journal of Electrical Power and Energy Systems*, vol. 118, no. July 2019, p. 105733, 2020, doi: 10.1016/j.ijepes.2019.105733.

[87] C. Mier, J. R. Vidal, and M. Dalstein, "Data Set: Methods for Partial Discharge Calibration in Gas-

Insulated Substations for HVDC Power Grids and Charge Evaluation Uncertainty." Zenodo, 2023. doi: 10.5281/zenodo.7937107.

[88] A. Pirker and U. Schichler, "Partial discharge measurement at DC voltage -Evaluation and characterization by NoDi∗ pattern," *IEEE Transactions on Dielectrics and Electrical Insulation*, vol. 25, no. 3, pp. 883–891, 2018, doi: 10.1109/TDEI.2018.006742.

[89] F. Alvarez, J. Ortego, F. Garnacho, and M. A. Sanchez-Uran, "A clustering technique for partial discharge and noise sources identification in power cables by means of waveform parameters," *IEEE Transactions on Dielectrics and Electrical Insulation*, vol. 23, no. 1, pp. 469–481, Feb. 2016, doi: 10.1109/TDEI.2015.005037.

[90] H. Zhang, T. Zhao, H. Liu, W. Wang, and W. Gong, "An Anti Interference Technology of UHF PD Detection in UHV GIS Based on Automatic Time Difference Analysis," *International Conference on Advanced Electrical Equipment and Reliable Operation, AEERO 2021*, pp. 1–5, 2021, doi: 10.1109/AEERO52475.2021.9708358.

[91] N. Kularatna, A. S. Ross, J. Fernando, and S. James, "Background to Surge Protection," *Design of Transient Protection Systems*, pp. 1–15, 2019, doi: 10.1016/b978-0-12-811664-7.00001-x.

[92] K. Sack and C. Q. Su, "A non-contact directional sensor for partial discharge measurements," *Conference Record of IEEE International Symposium on Electrical Insulation*, pp. 1–4, 2010, doi: 10.1109/ELINSL.2010.5549556.

[93] Jianqing Wang, O. Fujiwara, and K. Sasabe, "A simple method for predicting common-mode radiation from a cable attached to a conducting enclosure," in *APMC 2001. 2001 Asia-Pacific Microwave Conference (Cat. No.01TH8577)*, vol. 3, pp. 1119–1122. doi: 10.1109/APMC.2001.985316.

[94] C. Mier Escurra, "Dataset: Interference." Mendeley Data, V1, 2023. doi: 10.17632/mmbgn94f4j.1.

[95] M. Rostaghi-Chalaki, K. Yousefpour, J. Klüss, M. Kurum, J. P. Donohoe, and C. Park, "Classification and comparison of AC and DC partial discharges by pulse waveform analysis," *International Journal of Electrical Power and Energy Systems*, vol. 125, no. September 2020, p. 106518, 2021, doi: 10.1016/j.ijepes.2020.106518.

List of Publications

Publications Related to the Thesis

Journals

- C. Mier Escurra, A. Rodrigo Mor, T. Luo, and P. Vaessen, “Partial Discharge and Interference Discrimination in Gas-Insulated Systems using Electric and Magnetic Sensors,” International Journal of Electrical Power & Energy Systems, vol. 158, no. January, p. 109911, 2024, doi: 10.1016/j.ijepes.2024.109911.
- C. Mier, A. Rodrigo Mor, and P. Vaessen, “A directional coupler for partial discharge measurements in gas-insulated substations,” Measurement: Journal of the International Measurement Confederation, vol. 225, 2024, doi: 10.1016/j.measurement.2023.113996.
- C. Mier, A. Khamlichi, M. Dalstein, J. R. Vidal, F. Garnacho, A. Rodrigo Mor, T. Vu-Cong, “Methods for Partial Discharge Calibration in Gas-Insulated Substations for HVDC Power Grids and Charge Evaluation Uncertainty,” IEEE Sensors Journal, vol. 23, no. 19, pp. 23486–23493, 2023, doi: 10.1109/JSEN.2023.3302871.
- C. Mier, A. Rodrigo Mor, P. Vaessen, and A. Lathouwers, “Magnetic and electric antennas synergy for partial discharge measurements in gas-insulated substations: Power flow and reflection suppression,” International Journal of Electric Power Energy Systems, vol. 144, no. January 2023, pp. 1–9, 2023, doi: 10.1016/j.ijepes.2022.108530.
- C. Mier, A. Rodrigo Mor, L. Castro, and P. Vaessen, “Magnetic and electric antennas calibration for partial discharge charge estimation in gas-insulated substations,” International Journal of Electric Power Energy Systems, vol. 141, no. January, p. 108226, 2022, doi: 10.1016/j.ijepes.2022.108226.
- C. Mier, A. R. Mor, and P. Vaessen, “Design and Characterization of a Magnetic Loop Antenna for Partial Discharge Measurements in Gas Insulated Substations,” IEEE Sensors Journal, vol. 21, no. 17, pp. 18618–18625, 2021, doi: 10.1109/JSEN.2021.3089084.

Conferences

- [Accepted], C. Mier Escurra, A. Rodrigo Mor, and P. Vaessen, “PARTIAL DISCHARGE POWER FLOW IN GAS-INSULATED SUBSTATIONS USING MAGNETIC AND ELECTRIC ANTENNAS,” in International Symposium on High Voltage Engineering 2023.
- C. M. Escurra and A. R. Mor, “Balanced Magnetic Antenna for Partial Discharge Measurements in Gas-Insulated Substations,” in 2022 9th International Conference on Condition Monitoring and Diagnosis, CMD 2022, pp. 509–512. doi: 10.23919/CMD54214.2022.9991698.
- C. Mier and A. R. Mor, “Partial Discharge Charge Estimation In Gas Insulated Substations Using Electric and Magnetic Antennas,” in IEEE 2022 International Conference on Dielectrics, 2022, pp. 1–4.
- C. M. Escurra and A. R. Mor, “Test Bench and Frequency Response of a Magnetic Antenna used in GIS PD Measurements,” in 2021 Electrical Insulation Conference, EIC 2021, 2021, no. 2, pp. 269–272. doi: 10.1109/EIC49891.2021.9612372.

Other Publications

Journals

- E. van Veldhuizen, C. Mier, A. Lathouwers, A. Rodrigo Mor, and M. Ghaffarian, “The effect of humidity on the AC breakdown strength of C4-FN/CO2 (5%/95%) and the partial discharge behaviour of corona under different operating conditions,” IEEE Transactions on Dielectrics and Electrical Insulation, pp. 1–8, 2024, doi: 10.1109/TDEI.2024.3390649.
- F. Garnacho, F. Álvarez, A. Elg, C. Mier et al., “Metrological Qualification of PD Analysers for Insulation Diagnosis of HVDC and HVAC Grids,” Sensors (Basel)., vol. 23, no. 14, 2023, doi: 10.3390/s23146317.
- C. Vera, F. Garnacho, J. Klüss, C. Mier et al., “Validation of a Qualification Procedure Applied to the Verification of Partial Discharge Analysers Used for HVDC or HVAC Networks,” Appl. Sci., vol. 13, no. 14, 2023, doi: 10.3390/app13148214.

Conferences

- [Accepted], M. Dalstein, T. Vu-Cong, C. Mier Escurra, et al., “NEW MAGNETIC SENSOR FOR PARTIAL DISCHARGES MEASUREMENT APPLIED TO HVDC CONSTRAINTS INSIDE GIS,” in International Symposium on High Voltage Engineering 2023.
- C. M. Escurra, A. R. Mor, and P. Vaessen, “IEC 60270 Calibration Uncertainty in Gas-Insulated Substations,” 2023 IEEE Electrical Insulation Conference EIC 2023, pp. 1–4, 2023, doi: 10.1109/EIC55835.2023.10177354.
- A-P. Elg, F. Garnacho, M. Agazar, J. Meisner, A. Merev, E. Houtzager, J. Haellstroem, K. Lahti, C. Mier Escurra, C. A. Platero, T. Micand, T. Steiner, A. Voss, "Research Project EMPIR 19ENG02 Future Energy," VDE High Voltage Technology 2020; ETG-Symposium, Online, 2020, pp. 1-6.

Acknowledgements

In this section, I would like to mention all the people who induced me to the Ph.D., helped me get through it, and supported me in finalizing it.

First, I give my thanks to my promotors Dr. Armando Rodrigo Mor and Prof. Peter Vaessen. Thank you Armando for your guidance through the whole four years of the PhD. Your passion for new ideas was transmitted to me, generating good results. It was not easy to have online meetings, but you managed your time to discuss what we needed every week. But most importantly, I thank you for inviting me to be part of your research team since the master's and then the PhD. Thank you Peter, for all your advice and guidance during the PhD, not only in the technical stuff but also in my professional career. Thank you for trusting me with my decisions related to my budget, allowing me to attend very fruitful conferences and workshops.

Thanks to the committee members Prof. Dr. Guillermo Robles Muñoz, Prof. Dr. Rob Ross, Prof. Dr. Stefan Tenbohlen, Prof. Dr. Ronald Plath and Prof. Dr. Ir. Marjan Popov for your valuable time invested in sharing your comments for my thesis. I am very glad for your interest in taking part in my defence.

Special thanks to Sharmila Rattansingh for all her patience and help in all the administrative purposes. You made life much easier through every process. Apart from your help, I appreciate you for receiving me into your office to have a small conversation and grab some candy. I also thank Marieke Bijl for her help and kindness in the HV group.

I would also like to thank the HV academic staff. Dr. Mohamad Ghaffarian Niasar, thanks for sharing your knowledge and practical expertise in the lab. I enjoyed having conversations with you. Dr. André Lathouwers, thank you for your valuable experience in gas-insulated substations and the opportunity you gave me to supervise a master's student. I enjoyed your exciting conversations about your trips with your mobile home; I will do that someday. Thanks to Dr. Christiann Engelbrecht for sharing your professional experience with me, which gave me a perspective on my career path. Thanks to Dr. Dennis van der Born, although you joined the group by the end of my PhD, I had a good time in Glasgow and learned practical things in the lab and onsite.

Also, very important for the finalization of my PhD, I would like to thank the HV laboratory staff. Thank you Wim Termorshuizen, for your immeasurable help in the workshop. You made even the craziest designs that came to my mind real. Thank you, Luis Carlos Castro, for your help and valuable perspective on the experiments. Thank you Imke Splinter and Paul

van Nes, for helping me assemble the test setups and advising me on improving the measurements.

Thanks to my office mates for making an enjoyable place of work. Thanks to Tianming for his endless help in COMSOL and the complicated mathematical stuff. I also appreciate the pleasant conversations we had. I had a really good and memorable time with you in Glasgow. I also want to thank you for your patience with my jokes. Thanks to Weichuan for our terrific conversations and the delicious restaurants you showed me in Rotterdam. Finally, thanks to my other office and Asian friend Dhanashree for your friendship since the master's; it was a pleasure finding you back in the PhD. I thank all of you for sharing our cultures.

Thanks to all my colleagues for sharing a good time inside and outside the office. Thanks to the kings Marco, Lyu, and Calvin for letting me be the only champion of the king's tournament and for the fun we had. Thanks to Alvaro, Darío, David and Djurre for never rejecting a beer after the office. Thanks to my one-month office mate Leila for the nice conversations and her help with the AI course. Thanks to Sohrab for all the good laughs. Thank you Reza and Zhengzhao, for the fish market lunches we had. Thanks, Miad, for organizing gatherings with the group. Thank you Lu and Francesca, for your friendship during the master's and the PhD. Thank you for your company during lunch and coffee break Manfredo, István, Mladen, Joel, Ibrahim, Wenli, Carina, Faezeh, Guangyao, Sachin, Farshid, Felipe, Koen, Margo Lucia and people I might have forgotten.

Thanks to the "BOLO" group (or whatever name it has now) for the good moments during these four years. An essential part of a satisfactory PhD is balancing the work with fun, and you made that happen. Thank you for coming to my wedding and visiting Europe with your company. Thank you, Raphael, Sena, Franco, Jérémie, and Panos.

Thanks a lot to all my friends back in Mexico, whose names I will not mention because I know they will not read this thesis. But I would like to express my appreciation for all their good thoughts during my PhD.

Thanks to my Dutch family for receiving me in your beautiful country and sharing with me important family moments. Thank you tío Hugo, tía Cecilia, Tomás, Camila y Susana.

Thanks to "Clan Krnl" for the good and bad moments that we have shared, which have resulted in what I have become now. Thanks, Erik, for all the fun we had when you visited Europe or I went back to Mexico. Thanks, Memo, for all the interesting conversations about electrical engineering and life. Also, thanks for inspiring me in my career path.

Gracias a mis papás, por su apoyo incondicional. Gracias a mi papá por todas sus desveladas para sacarme adelante y darme lo mejor. También gracias por enseñarme disciplina y las conversaciones interesantes sobre física conceptual. Gracias a mi mamá por sacrificarlo todo por tus hijos, por estar siempre al pendiente y perdonarme todos mis errores.

Finally, thanks to the most important person in my life. Thanks to Julissa for supporting my decision to do a PhD, even though it meant having a long-distance relationship. Thanks for your motivation, energy and positivism that inspired me throughout my PhD. And thanks for loving me.

Curriculum Vitae

Christian Mier Escurra was born in Aguascalientes, Mexico, in 1991. He obtained a Bachelor's degree in Mechanical with a minor in Electrical Engineering from ITESM, Monterrey, in 2014. In 2018, he received a Master's degree in Electrical Engineering from Delft University of Technology, in Delft, Netherlands. From 2014-2016, he worked as a junior engineer, and from 2018-2019 as a senior engineer in an electric power consultancy firm (Diram) in Mexico. He also worked in a power cable company as a researcher in 2019-2020 before perusing the PhD. Currently, he is a Ph.D. candidate at Delft University of Technology, in Delft, Netherlands. His research interests include monitoring and diagnostic, high voltage engineering, transients, and power systems.